

# **Remote Spacecraft Attitude Control by Coulomb Charging**

by

**Daan Stevenson**

B.S., University of California Berkeley, 2008

M.S., University of Colorado Boulder, 2011

A thesis submitted to the  
Faculty of the Graduate School of the  
University of Colorado in partial fulfillment  
of the requirements for the degree of  
Doctor of Philosophy  
Department of Aerospace Engineering

2015

This thesis entitled:  
Remote Spacecraft Attitude Control by Coulomb Charging  
written by Daan Stevenson  
has been approved for the Department of Aerospace Engineering

---

Hanspeter Schaub

---

Webster Cash

---

Brandon Jones

---

Daniel Moorer

---

Zoltan Sternovsky

Date \_\_\_\_\_

The final copy of this thesis has been examined by the signatories, and we find that both the content and the form meet acceptable presentation standards of scholarly work in the above mentioned discipline.

Stevenson, Daan (Ph.D., Aerospace Engineering Sciences)

Remote Spacecraft Attitude Control by Coulomb Charging

Thesis directed by Professor Hanspeter Schaub

The possibility of inter-spacecraft collisions is a serious concern at geosynchronous altitudes, where many high-value assets operate in proximity to countless debris objects whose orbits experience no natural means of decay. The ability to rendezvous with these derelict satellites would enable active debris removal by servicing or repositioning missions, but docking procedures are generally inhibited by the large rotational momenta of uncontrolled satellites. Therefore, a contactless means of reducing the rotation rate of objects in the space environment is desired. This dissertation investigates the viability of Coulomb charging to achieve such remote spacecraft attitude control. If a servicing craft imposes absolute electric potentials on a nearby nonspherical debris object, it will impart electrostatic torques that can be used to gradually arrest the object's rotation.

In order to simulate the relative motion of charged spacecraft with complex geometries, accurate but rapid knowledge of the Coulomb interactions is required. To this end, a new electrostatic force model called the Multi-Sphere Method (MSM) is developed. This approach uses conducting spheres positioned throughout a fixed geometry to determine what electrostatic forces and torques are acting on it. Computation times are orders of magnitude quicker than similar Finite Element Analysis (FEA) software, while accuracy to within 1% of the higher order truth models is maintained for the system parameters considered.

All aspects of the Coulomb de-spin concept are extensively analyzed and simulated using a simplified but representative system in which a spherical servicing craft attempts to remove the one dimensional (1-D) rotation from a cylindrical debris object. First, appropriate control algorithms are developed to ensure that the nonlinear Coulomb torques arrest the rotation with guaranteed stability. Baseline simulations suggest that 12 deg/s of rotation can be removed from a 3 m length by 1 m diameter cylinder in just 3 days, using voltage levels up to  $\pm 30$  kV. The sensitivity of this

performance to various system parameters and control strategies is analyzed in order to optimize an eventual Coulomb de-spin mission. Moreover, the complex interaction of the spacecraft with the plasma environment and charge control beams is modeled to determine what hardware requirements are necessary to achieve the desired electric potential levels. It is found that charge up and polarity switching procedures occur well within the time scales necessary to match the rotation of the debris object.

Lastly, the 1-D remote de-spin concept is validated experimentally using a scaled down terrestrial testbed. High voltage power supplies control the potential on two nearby conductors, a stationary sphere and a freely rotating cylinder. The nonlinear feedback control algorithms developed above are implemented to achieve rotation rate and absolute attitude control. This testbed is able to remove a 100 deg/s rotation rate from the cylinder in just 10 seconds by application of Coulomb torques alone, and control the absolute attitude to within 1.5 degrees of a reference angle. Collectively, these studies decisively validate the feasibility of Coulomb charging for remote spacecraft attitude control.



## Acknowledgements

The years spent pursuing this doctoral work at the University of Colorado Boulder constitute an incredibly rich and influential period of my life. Many thanks are in order to those who have helped me grow and mature during this time, both academically and personally. First and foremost, I wish to express the utmost gratitude to my academic advisor Dr. Hanspeter Schaub. The passion and rigor with which you teach in the classroom is unrivaled, as is the dedication with which you advise your students. Your guidance has inspired in me a deep devotion to this research topic, and I am truly proud of the work we have accomplished. Thanks also to the members of my prospectus and thesis committees, whose professional support and insights have greatly strengthened this dissertation.

It has been a pleasure to work alongside all the bright and talented students of the AVS lab, whose support and collaboration have been invaluable. Thanks to Carl Seubert for passing along his Coulomb charging knowledge and testbed, to Trevor Bennett for delving further into aspects of this research, and to everyone for constantly maintaining a light and jovial atmosphere in the lab. Moreover, I am glad to have had the chance to mentor and been assisted by several incredibly promising high school and undergraduate students over the years.

Mostly, I would be nowhere today without the nurturing support I have always received from my parents. Growing up in an environment of board games and puzzles, where I was introduced to counting in binary at age 5, it is hardly a surprise I fell in love with engineering. Thank you for reading to me every night before bed, and for instilling a distaste for idle time and an affinity to trying new things. Moreover, I attribute my zeal for the outdoors primarily to our countless

weekend hikes, however little I may have appreciated them at the time. To my older brothers, I prefer our current comradery to the pestering of our childhood, but I am a stronger person for it.

Lastly, I wish to thank all the amazing people I have met and befriended since I took the leap of faith in moving to Colorado. Our exploration of this state and beyond have kept me sane amidst my studies. I cherish every powder turn that has hit our face, every stretch of single track we have bombed down, every river we have navigated, every rock wall we have scaled, and every intramural championship shirt we have taken home. Here's to many more adventures with the ones I love!

**This research was funded by the NASA Science and Technology Research Fellowship (NSTRF) #NNX11AN47H and the National Science Foundation Graduate Research Fellowship Program (GRFP) under grant number 1000100047**

## Contents

### Chapter

<b>1</b>	Introduction	1
1.1	Motivation . . . . .	1
1.2	Satellite Charging Background . . . . .	5
1.3	Electrostatic De-spin Concept . . . . .	8
1.4	Overview of Research . . . . .	12
<b>2</b>	Electrostatic Models	15
2.1	Classical Electrostatic Models . . . . .	15
2.2	Multi-Sphere Method . . . . .	18
2.3	MSM Volume Population . . . . .	20
2.4	MSM Surface Population . . . . .	23
2.5	MSM Numerical Verification . . . . .	25
2.5.1	Two-Sphere System . . . . .	25
2.5.2	Cylinder Sphere System . . . . .	30
2.6	Boundary Element Method . . . . .	33
2.7	Satellite Model . . . . .	35
2.8	Constant Charge Modifications . . . . .	36
2.8.1	Insulators . . . . .	38
2.8.2	Floating Charge . . . . .	38
2.9	ISS Charged Droplet Experiment . . . . .	39

<b>3</b>	<b>Electrostatic De-spin</b>	<b>42</b>
3.1	System Dynamics . . . . .	42
3.2	Non-linear Control Theory . . . . .	46
3.2.1	Equilibrium Configurations . . . . .	46
3.2.2	Rate Control With Zero Nominal Potential . . . . .	48
3.2.3	Rate Control with Nominal Electrostatic Tugging or Pushing . . . . .	50
3.3	Baseline Simulation . . . . .	54
3.4	System Parameter Optimization . . . . .	57
3.4.1	Single Rotation Simulation . . . . .	57
3.4.2	Separation Distance . . . . .	59
3.4.3	System Scale . . . . .	60
3.4.4	Servicing Craft Size . . . . .	61
3.4.5	Debris Aspect Ratio . . . . .	61
3.5	Relative Position and Orientation Control Schemes . . . . .	63
3.5.1	Variable Separation Distance . . . . .	64
3.5.2	Circumnavigation Scheme . . . . .	65
3.5.3	Non-spherical Control Craft . . . . .	66
3.6	Asteroid De-spin . . . . .	69
<b>4</b>	<b>Charge Transfer Analysis</b>	<b>72</b>
4.1	Current Balance . . . . .	73
4.2	Power Requirements and Momentum Transfer . . . . .	76
4.3	Positive Potential Debris Craft . . . . .	77
4.4	Negative Potential Debris Craft . . . . .	80
<b>5</b>	<b>Experimental Testbed</b>	<b>83</b>
5.1	Background . . . . .	83
5.2	Experimental Setup . . . . .	85

5.3	Disturbance Characterization . . . . .	88
5.4	Rotation Rate Control . . . . .	91
5.4.1	Control Development . . . . .	91
5.4.2	Experimental Results . . . . .	92
5.5	Attitude Control . . . . .	93
5.5.1	Control Development . . . . .	93
5.5.2	Experimental Results . . . . .	95
<b>6</b>	<b>Conclusion</b>	<b>98</b>
6.1	Dissertation Summary . . . . .	98
6.2	Suggestions for Future Work . . . . .	99
	<b>Bibliography</b>	<b>102</b>
	<b>Appendix</b>	
<b>A</b>	<b>Coulomb Force Determination by Sensing</b>	<b>109</b>
<b>B</b>	<b>MSM Code</b>	<b>112</b>
<b>C</b>	<b>VMSM Parameter Variation</b>	<b>117</b>
<b>D</b>	<b>SMSM Packing Parameter</b>	<b>120</b>

## Tables

### Table

2.1	Parameters of three-sphere MSM for cylinder geometry . . . . .	23
2.2	Setup and computation time for calculation of force and torques between sphere and cylinder at 82 relative locations . . . . .	33
3.1	Parameters for baseline cylinder de-spin simulation . . . . .	55
3.2	Baseline de-spin results . . . . .	59
3.3	De-spin control schemes results . . . . .	63
4.1	Plasma environment parameters for current balance . . . . .	76
4.2	Charge beam characteristics for positive debris craft . . . . .	78
4.3	Charge beam characteristics for negative debris craft . . . . .	81
5.1	Testbed component details . . . . .	88
C.1	Scalar residual comparison between three-sphere MSM and single sphere model . . .	118
C.2	Scalar residual comparison of scaled parameter variation from numerical simulation .	118

## Figures

### Figure

1.1	Number of cataloged objects in Earth orbit <sup>1</sup> . . . . .	2
1.2	Depiction of the GEO debris belt <sup>2</sup> . . . . .	3
1.3	Illustration of various current sources that affect spacecraft charging <sup>32</sup> . . . . .	6
1.4	Illustration of the electrostatic tugging concept <sup>32</sup> . . . . .	8
1.5	Depiction of the remote Coulomb de-spin concept . . . . .	9
2.1	Comparison of various electrostatic models . . . . .	17
2.2	Conceptual depiction of the Multi-Sphere Method . . . . .	18
2.3	Maxwell 3D model and parameter sweep for data export . . . . .	22
2.4	Three-sphere MSM parameters for cylinder geometry . . . . .	23
2.5	Methodology for parameter selection of surface populated MSM . . . . .	25
2.6	Two analytic models for the two sphere system that capture induced effects . . . . .	27
2.7	Various uniform point distributions on the surface of a sphere . . . . .	27
2.8	Charge density distribution on two spheres ( $\phi_1 = \phi_2 = +30$ kV) . . . . .	28
2.9	Error in force between two spheres for various electrostatic models . . . . .	29
2.10	Charge density distribution on SMSM of cylinder and sphere ( $\phi_1 = \phi_2 = +30$ kV) . . . . .	30
2.11	Force and torque comparison between MSM models and Maxwell3D . . . . .	32
2.12	MSM model of a simple satellite . . . . .	36
2.13	Orbital motion of water droplets on the ISS by Coulomb interaction . . . . .	40

2.14	Simulation of Coulomb orbits modeled by the MSM . . . . .	41
3.1	Free body diagram for cylinder-sphere system . . . . .	43
3.2	Coulomb torques for various orientations and potentials . . . . .	45
3.3	Illustration of departure angle with respect to equilibrium orientations . . . . .	47
3.4	Illustration of pulling and pushing configurations. . . . .	52
3.5	Illustration of Lyapunov function and level sets for unit inertia $I_2$ and gain $\beta$ . . . .	53
3.6	State Space Flow Illustration In Relation to Lyapunov Level Sets. . . . .	54
3.7	Three sphere MSM for cylinder-sphere system . . . . .	55
3.8	Cylinder tug and de-spin simulation using Coulomb charge control . . . . .	57
3.9	Surface populated MSM for cylinder-sphere system . . . . .	58
3.10	Performance dependency on servicing craft size . . . . .	62
3.11	Performance dependency on debris aspect ratio . . . . .	62
3.12	Object separation for constant surface to surface distance . . . . .	64
3.13	Position of craft in circumnavigation scheme . . . . .	65
3.14	Configuration for windmill control craft . . . . .	66
3.15	Coulomb torque dependency on debris and control craft angles . . . . .	67
3.16	Results from windmill control craft scenario . . . . .	68
3.17	Voltage and charge distribution on the servicer craft and asteroid in de-spin simulation. .	71
4.1	Depiction of charge transfer between craft . . . . .	73
4.2	Time history of charge control with positive debris craft . . . . .	79
4.3	Power optimization for negative debris craft . . . . .	80
4.4	Time history of charge control with negative debris craft . . . . .	81
5.1	One-Dimensional Spacecraft Formation Flight Testbed for Terrestrial Charged Relative Motion Experiments . . . . .	84
5.2	Depiction of the experimental setup for charged attitude control . . . . .	87



5.3	Screenshot of the LabVIEW graphical user interface . . . . .	88
5.4	Characterization of disturbance torques . . . . .	90
5.5	Cylinder rotation rate control, experimental and simulation . . . . .	93
5.6	Cylinder attitude control: experimental and simulation . . . . .	96
A.1	Gaussian surface on conductor. . . . .	109
A.2	Charged Conductor. . . . .	110
D.1	Optimal packing parameter for Surface MSM on sphere . . . . .	120
D.2	Optimal packing parameter for Surface MSM on cylinder . . . . .	121
D.3	Error in force for various packing parameters . . . . .	122

## Chapter 1

### Introduction

#### 1.1 Motivation

Since the 1957 launch of Sputnik 1, the first synthetic body to orbit Earth, the space surrounding our planet has become more and more densely populated with every subsequent satellite mission. Currently, the Joint Space Operations Center (JSpOC) tracks more than 16,000 objects orbiting Earth, via a variety of ground based radars as well as some space based sensors.<sup>83</sup> As these methods are generally capable of detecting only objects larger than 10 cm in diameter, the total number of man-made objects in space is estimated to be many orders of magnitude larger. Besides the 1,200 operational spacecraft currently in orbit, the majority of the catalog consists of inactive satellites and rocket bodies, many of them fragmented by break-up events.<sup>44</sup> While accidental spacecraft explosions are common enough in the challenging operational environment of space, several anti-satellite (ASAT) missile tests such as the 2007 destruction of the Chinese Fengyun-1C satellite have contributed significantly to the debris population.<sup>38</sup> The increase in fragmentation debris due to this event can be seen clearly in Figure 1.1, which shows the evolution of cataloged space objects.

In 1990, Donald Kessler investigated the possibility of the self-sustained growth of space debris caused by a cascading series of collision events.<sup>39</sup> Such a scenario, commonly known as the Kessler Syndrome, could render the use of satellites and further space exploration unfeasible for many generations. The unexpected 2009 collision between the satellites Iridium 33 and Cosmos 2251, which produced more than 2,000 new debris objects,<sup>93</sup> highlighted the reality of such

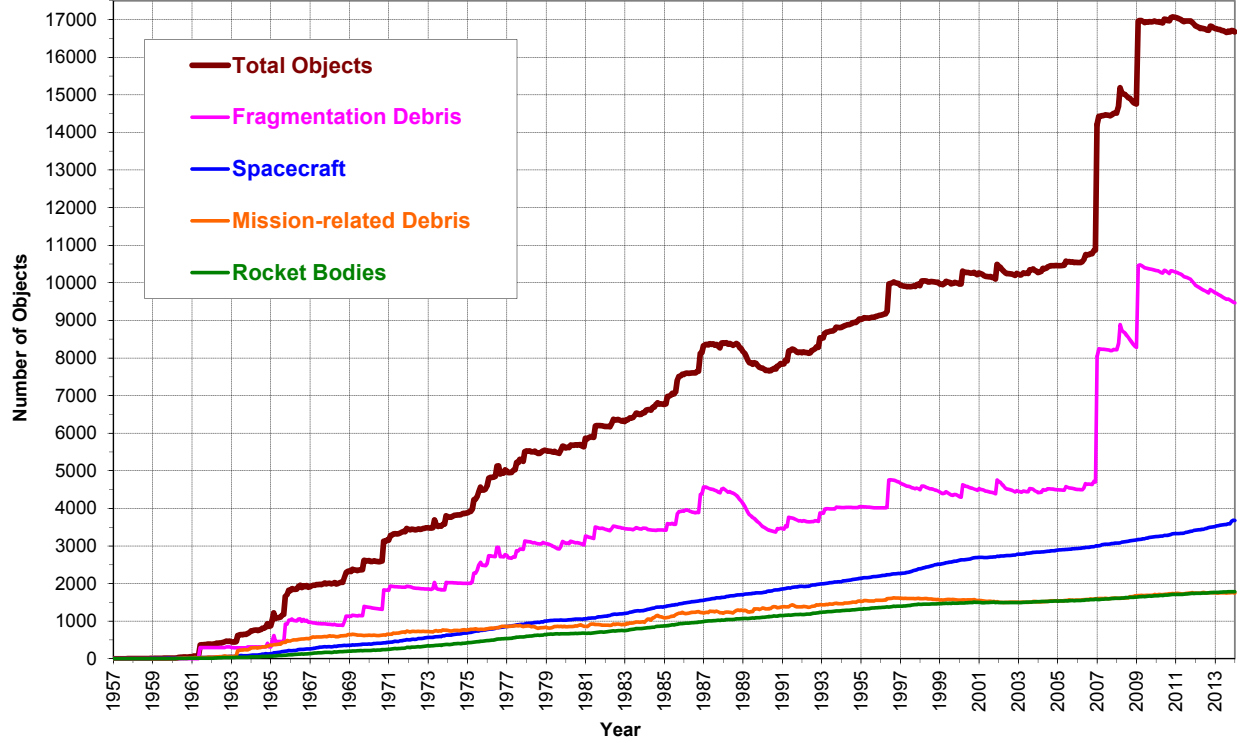


Figure 1.1: Number of cataloged objects in Earth orbit<sup>1</sup>

a self-propagating orbital debris calamity. Extensive procedures are in place to predict the close approaches of orbiting bodies (conjunction analysis) and maneuver satellites to decrease the probability of collisions (collision avoidance). With inherent relative velocities on the order of km/s, even impacts from very small objects can easily penetrate satellite structures and render them obsolete. Moreover, such collision risks presents an undeniable danger for human operations on the permanently manned International Space Station (ISS).

While there is little international oversight to enforce debris mitigation policies, the Inter-Agency Space Debris Coordination Committee (IADC) suggests that satellite operators incorporate an end of life strategy into their mission. At altitudes below 2,000 km, known as Low Earth Orbit (LEO), satellites experience considerable atmospheric drag. When the altitude is brought below 100 km, there is sufficient atmospheric density to de-orbit the satellite, generally resulting in its

<sup>1</sup> <http://orbitaldebris.jsc.nasa.gov/newsletter/pdfs/ODQNv18i1.pdf>

disintegration and destruction. At the much higher 35,786 km altitude Geosynchronous (GEO) orbits, a lack of atmospheric drag inhibits the natural decay of inoperative satellites. As a result, this highly desirable orbit regime is quickly becoming overpopulated, as evident from Figure 1.2. This presents a serious concern for the 18 billion USD worth of insured GEO assets as of 2011 (compared with 1 billion in LEO).<sup>17</sup> Since the fuel requirements for re-entry from such high orbits are cost prohibitive, the preferred end of life strategy is relocation to a graveyard orbit with a sustained perigee at least 200 km above the GEO belt.<sup>3</sup>

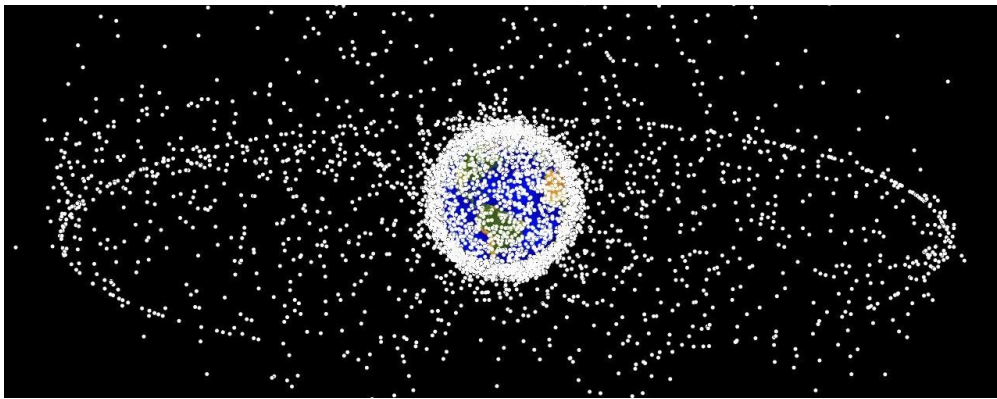


Figure 1.2: Depiction of the GEO debris belt<sup>2</sup>

In Reference 47, Liou postulates that active debris removal (ADR) operations with a minimum removal rate of 5 objects per year is necessary to curb the naturally increasing debris situation in LEO. **Analysis of satellite congestion in the GEO environment also suggests that mitigation measures must be combined with active remediation to preclude an escalating scenario similar to that in lower orbits.**<sup>1,2</sup> Various studies have investigated the feasibility of ADR missions, including analysis of optimal trajectories and transfer orbits to de-orbit or relocate multiple debris objects.<sup>4,12</sup> Many of these missions assume the servicer can capture a debris object by some soft mechanical interface, such as a net, hook or claw.<sup>60,64</sup> Other studies propose to attach a thrusting module or electrodynamic tether to the tumbling spacecraft in order to move them into desired orbits.<sup>20,56</sup> Many of these studies neglect simple conservation of energy laws -

<sup>2</sup> <http://orbitaldebris.jsc.nasa.gov/photogallery/beehives/GEO1280.jpg>

a body rotating in space will transfer its rotational momentum to the contacting servicing craft, thus risking the addition of another uncontrolled object to the debris population.

Several other approaches avoid interfacing with the debris body, rather affecting its orbit by remote processes. The ion-sheppard method would direct the focused exhaust cone of an ion engine at a satellite to gradually raise or lower its altitude.<sup>10,43</sup> Considering the unstable nature of a pushing configuration, this approach will require very precise knowledge of the exhaust characteristics and monitoring of the debris location and orientation. Another promising method, as discussed further in the following section, is the electrostatic tractor concept. By generating electrostatic potentials on both craft using charge control devices, a servicing craft would gradually tug the debris object by means of their electrostatic attraction.<sup>72,74</sup> While only feasible at the High Earth Orbit (HEO) regime, the control requirements of this approach are more forgiving in relative position and charge level errors.

While the above method could increase the semi-major axis of a GEO debris object by 300 km in several months,<sup>29</sup> a docked Hohmann transfer could achieve the desired orbit correction in just over 12 hours. An alternative to repositioning derelict satellites into a graveyard orbit is to service them by replenishing fuel reserves or repairing failed components. Such missions, as investigated by NASA's Satellite Servicing Capability Office and DARPA's Phoenix program, preclude the unnecessary insertion of countless replacement satellites. Either approach requires the servicing vehicle to mechanically interface with the debris object, which is explored in References 51 and 96. These docking procedures are often hazardous or impractical considering the excessive rotational kinetic energy of a heavy debris object in an uncontrolled tumble. While pose algorithms and attitude matching maneuvers for rendezvous are generally restricted to rotation rates below 1 deg/s,<sup>18,63</sup> some GEO debris objects exhibit rotation rates greater than 10 deg/s.<sup>37,54</sup> In order to expand the set of viable targets for a physical docking strategy, a touchless method of detumbling is highly desirable. **By remotely reducing the rotation rate prior to rendezvous, collision risks and guidance and control challenges are greatly reduced during docking operations.**

## 1.2 Satellite Charging Background

As a result of their interaction with the space environment, all spacecraft naturally experience accumulation of electrostatic charge. Due to the low density and high energy of molecules at orbital altitudes, the space environment constitutes a plasma, where negatively charged electrons and positively charged ions exist as independent charge carriers. Collisions occur constantly between the mobile charged particles and the surface of the spacecraft, resulting in positive and negative plasma currents. Because the mass of an electron is several orders of magnitude smaller than that of protons and ions, while their thermal energies tend to be comparable, electron velocities are generally much higher than that of positive charge carriers. Therefore, a satellite without solar irradiation absorbs more electrons and acquires a net negative charge.<sup>19,46</sup> In space, Langmuir probes or electrostatic analyzers can be used to provide measurements of spacecraft potential.<sup>45</sup> The ATS-5 and ATS-6 satellite missions, launched to GEO in 1969 and 1974, measured ambient potential levels up to -10 kV in solar eclipse.<sup>52</sup> When illuminated by the sun, meanwhile, the photoelectric effect serves to eject electrons from the spacecraft, and a net positive charge may result. Secondary electron emission (SEE) in the form of ejected and backscattered electrons create further electric currents. Most of the currents described above and depicted in Figure 1.3 are dependent on the satellite potential. As a result, the spacecraft settles to whatever equilibrium potential balances the incoming and outgoing currents.<sup>74</sup>

By emitting beams of charged particles to the space environment, spacecraft are capable of actively controlling their electrostatic potential. The charge carriers must be accelerated by electron or ion guns with sufficient energy levels to escape the electrostatic influence of the charged craft, and achievable potentials are limited by the device energy. In 1979, the SCATHA satellite was launched carrying a 3 kV electron beam and verified the ability to control spacecraft potential up to +3 kV with respect to the ambient plasma potential.<sup>49</sup> A later study shows that with a charge control device using only Watt levels of power a vehicle in an average GEO plasma environment can be charged to a potential of 10s of kV within milliseconds.<sup>41</sup> Normally, charge control devices

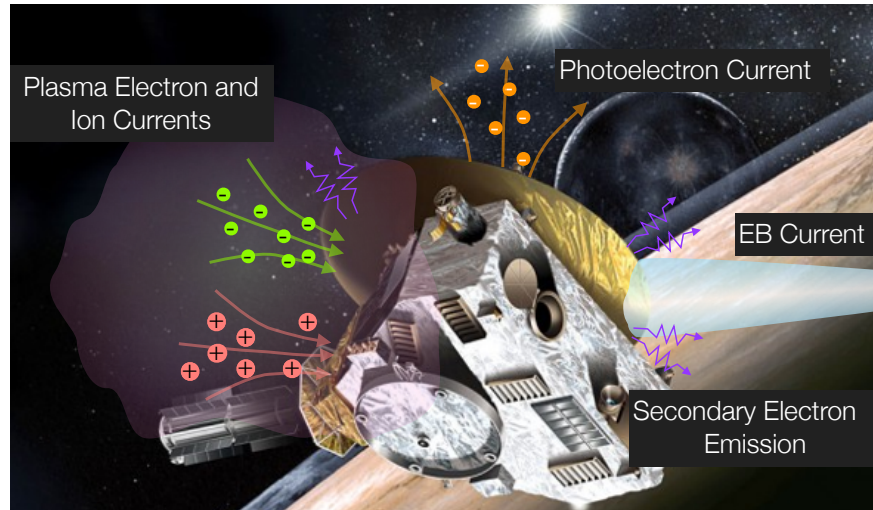


Figure 1.3: Illustration of various current sources that affect spacecraft charging<sup>32</sup>

are used to mitigate net spacecraft charging, as electrostatic discharge (ESD) events are one of the leading causes of on-orbit failures and anomalies.<sup>65</sup> These discharges occur as a result of differential charging, when unequal voltage levels reside at different locations of the spacecraft. If the vehicle is designed to be fully conducting, with all outer surfaces connected to a common ground, successful operation is possible at high absolute electrostatic potentials.<sup>59</sup>

A substantial research effort was initiated more than a decade ago to determine the feasibility of using Coulomb forces from charged spacecraft for relative position control in close proximity formations.<sup>41,42,73</sup> The use of electrostatic actuation for formation flying is attractive compared to conventional thrusters because non-renewable fuel reserves are not depleted and plume impingement issues are avoided. The required mass emission for this Coulomb actuation is so low that this mode of actuation can essentially be considered propellantless. Applications include Separated Spacecraft Interferometry (SSI), to achieve large field-of-view planetary imagery with unprecedented resolution, and small-body relative orbits with cameras or other robotic devices to inspect external spacecraft integrity. Several studies analyze the relative motion dynamics of a 2 to multi-craft Coulomb formation.<sup>9,30,92</sup> Control is limited to one parameter per spacecraft (the prescribed voltage level), and the direction of the resulting forces is predetermined by the relative positions

in the formation. Complex charge control strategies have been developed that compensate for the nonlinear nature of the electrostatic forces and coupling with differential gravity.<sup>50,55,67,68</sup>

One limitation of the Coulomb charging technology is the natural electric shielding that results from the space environment. Any charged object in a plasma attracts particles of opposite polarity, which form an electric sheath around the object and diminish the electric fields. This dropoff is characterized by the Debye length, a coefficient dependent on the densities and energies of the particles present in the plasma.<sup>58</sup> These quantities are highly dependent on the local space weather, but nominal values are around 1 cm for the colder, denser plasmas in LEO and around 200 m in the hotter, sparser GEO environment.<sup>21,90</sup> This restricts the use of Coulomb charge control at reasonable separation distances to higher Earth orbits, where Debye shielding can be neglected during nominal conditions. Even within a given altitude, plasma parameters can vary drastically due to concurrent solar activity,<sup>94</sup> so operation may have to be adjusted or suspended during solar storm events. Inter-satellite arcing presents another concern for charged spacecraft flying in close formation, but the proposed separation distances are many times larger than the centimeter levels required in GEO to arc between objects at kiloVolts of potential.<sup>16</sup>

While only cooperative Coulomb charging scenarios have been discussed so far, the realm of potential missions can be expanded with the ability to remotely charge noncooperative space objects. If the charged particle beams considered above can be focused and directed from a servicing craft towards an uncontrolled satellite, the electric potential on both craft can be controlled to establish an attractive electrodynamic tether between the vehicles as shown in Figure 1.4.<sup>72</sup> Reference 29 discusses the thrust profiles required to re-orbit a GEO debris object to a graveyard orbit via such an electrostatic tractor, while Reference 74 assesses the charge transfer requirements. Various other applications of spacecraft charging have been considered. Flexible conducting membranes can acquire significant rigidity when they are charged to high voltage levels. These Electrostatically Inflated Membrane Structures (EIMS) may be used to build large spacecraft assemblies such as solar sails in orbit.<sup>88</sup> Moreover, unique charged modules may be tethered together to create large rigid networks of sensor systems.<sup>79</sup>



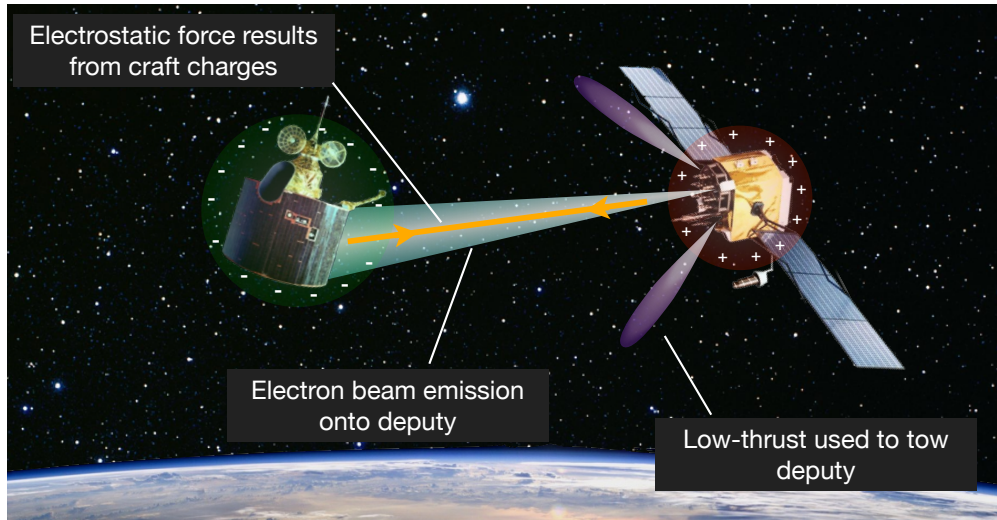


Figure 1.4: Illustration of the electrostatic tugging concept<sup>32</sup>

### 1.3 Electrostatic De-spin Concept

Most previous studies regarding Coulomb charge control have modeled the electrostatics of satellites with point charges or spherical conductors. In this case, all forces are assumed to be on-axis with the center of the spacecraft and result only in translational motion. In reality, most spacecraft contain decidedly nonspherical features, such as solar panels and communication dishes. When two such charged vehicles fly in close proximity to each other, the asymmetric charge distributions that reside on these geometries will induce electrostatic torques on the bodies. **If these moments are generated intentionally, they can be harnessed to arrest the rotation of uncontrolled space objects and address the need for remote de-spin operations prior to rendezvous.**

Figure 1.5 shows an uncontrolled spinning satellite flying in close proximity to a servicing spacecraft equipped with charge control devices. By directing a focused electron beam toward the spinning satellite, opposing electrostatic polarities are generated. The two bodies are mutually attracted by the Coulomb force between them, so the servicing spacecraft must thrust away to maintain a constant separation distance. Because the large solar panel on the spinning satellite is closer and experiences a slightly larger force than the rest of the body, a net torque that opposes the rotation is generated. As the uncontrolled satellite continues rotating, the servicing spacecraft

emits positive ions into deep space to obtain a negative net charge. The bodies then repel each other, while the proximity of the large antenna results in further arresting torques.

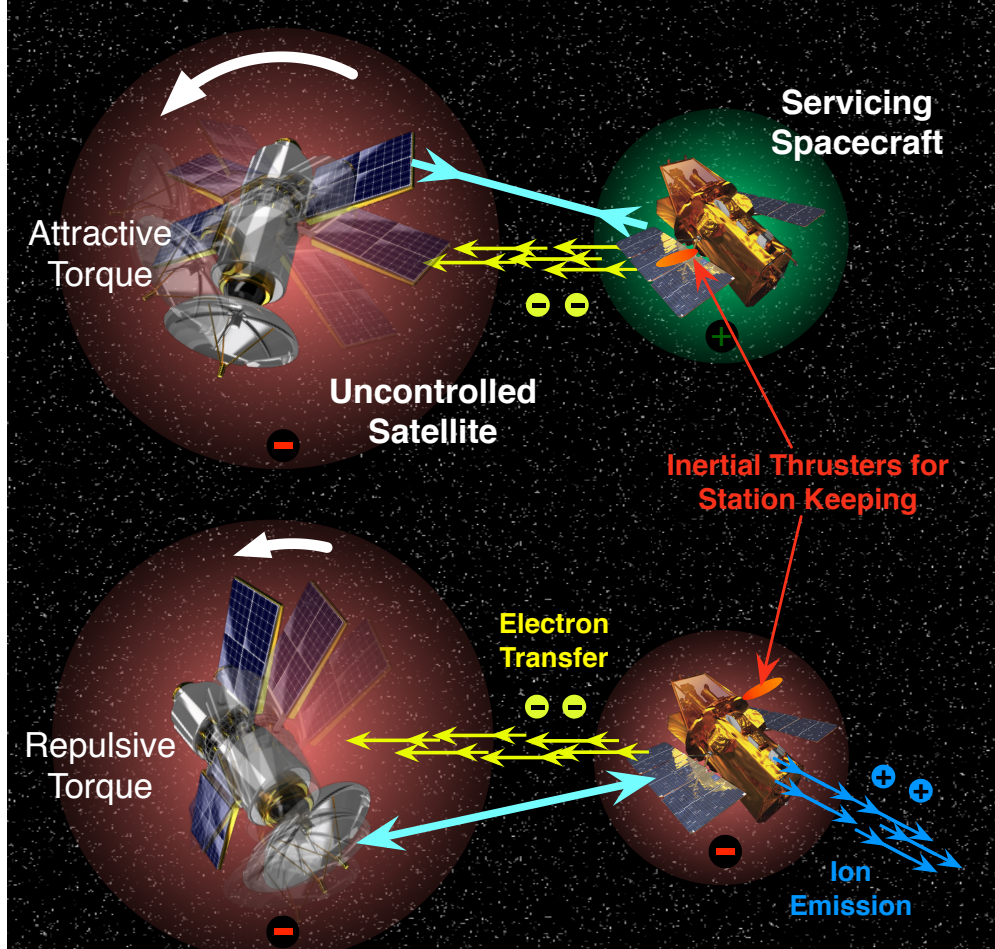


Figure 1.5: Depiction of the remote Coulomb de-spin concept

Successful implementation of this concept requires extensive research to address challenges that span across various disciplines including astrodynamics, electrodynamics, numerical techniques and control theory. First, a computationally efficient model of the electrostatic interaction between generic geometries is necessary. This can be used to create 6 Degree of Freedom (6DOF) simulations of the spacecrafts' relative motion and attitudes. Algorithms must be developed for the remote attitude control problem once the extent of controllability is established. This includes analysis of the active charge transfer process, in order to predict the hardware and power requirements.

To increase the Technology Readiness Level (TRL)<sup>48</sup> of this technology in anticipation of mission implementation, laboratory experiments are necessary to verify theoretical predictions. Creating a free motion terrestrial testbed with high voltage capabilities presents considerable challenges. **In addressing the tasks posed above, this body of research advances a technology that stands to address the serious active debris removal challenge existent in the astrodynamics field.**

Development of the Coulomb charge control concept has progressed rapidly over the past decade, but financial support for flight testing of these concepts remains elusive. For now, it is imperative to mature this technology further in theory and by terrestrial experimentation, thus demonstrating its feasibility to the rest of the astrodynamics community. The research conducted within this dissertation evolves the remote electrostatic spacecraft attitude control concept from its inception to such a point, but further studies are required. Within this investigation, the system dynamics are generally constrained to one dimension in order to focus on the fundamental aspects of Coulomb attitude control. This is a reasonable approximation considering that space objects tend to converge to a minimum energy spin state about the axes of maximum inertia. If 3D spacecraft rotation is considered, the complexity of control algorithms increases drastically. Repositioning of the servicing craft allows for increased controllability, but it might be impossible to arrest rotation about symmetric axes.<sup>6</sup>

Further, development of an adequate sensor suit is required for the servicing craft to acquire the necessary information about the spinning debris object. Unless launch data is known a priori about the target satellite, its exact geometry and inertia must be determined by estimation. During de-spin operations, knowledge of the debris attitude is crucial in order to apply the correct polarity charge control. This may be acquired using structured light, visual flow methods, or flash LIDAR sensors. In order to maintain knowledge of the relative motion for collision avoidance and accurate prediction of the electrostatic force magnitudes, optical and laser ranging techniques can be used. The servicer's inertial thrust levels need to be in the milli-Newton range to balance the equivalent electrostatic forces. It is important that the inertial thrusting solution does not interfere with the

electrostatic tractor performance. This could be achieved by using neutral gas thrusters, or select types of electric propulsion systems such as field-emission electric propulsion (FEEP) thrusters. In both cases care must be taken to analyze the coupled thruster emission flow subject to the charging on the debris and servicer.<sup>7</sup>

While fundamental analysis of the charge transfer requirements is being conducted, this aspect of the technology stands to benefit from further investigation. Complete efficiency is generally assumed from the charge transfer, but little is known about the exact interaction of a charged beam with various materials that may be encountered on the surface of the debris object. Lastly, real time knowledge of the debris' potential level must be obtained for accurate prediction of the electrostatic interaction. Because of the absence of conventional sensors that can achieve this type of measurement, the information may have to be gathered by estimation approaches. Further knowledge of the charge transfer process can be gleaned from terrestrial experimentation conducted in vacuum chambers.

Electrostatic detumble presents a very promising solution to the issue of rendezvous with uncontrolled space objects, but several alternatives do exist. First, active debris removal or servicing operations might focus only on vehicles that rotate at rates within the deg/s limitations of current pose algorithms. While certain ground based optical methods for estimating spacecraft attitudes are emerging,<sup>66</sup> it is difficult to determine the rotation rate of a specific derelict GEO satellite. The momentum transfer of the ion-sheppard method may be used to reduce rotation rates by focusing the ion beam on the appropriate half of the spinning object.<sup>11</sup> Lower actuation levels are achievable by this approach than the electrostatic method. Another method for touchless detumble is to use magnetic fields emitted from a chaser vehicle to impose braking eddy current torques on a foreign object. This approach would require very close proximity operations and is reliant on a fully conducting foreign object.<sup>53,89</sup> Due to the commonality in challenges, many of these alternate technologies benefit from the theories developed in this research effort and vice versa.

## 1.4 Overview of Research

The development of Coulomb charge control technology has progressed rapidly over the past decade. The electrostatic attitude control idea was conceived more recently, but stands out as a promising means to remotely de-spin derelict satellites. **The scope of this dissertation is to mature Coulomb attitude control in theory and by terrestrial experimentation, thus advancing its Technology Readiness Level (TRL) and demonstrating its feasibility to the astrodynamics community.** To this end, three research tasks are identified and carried out in this thesis.

**Research Task 1 (Chapter 2):** Develop computationally efficient electrostatic models to predict the Coulomb interaction between multiple bodies with generic geometries.

- Survey existing electrostatic models, analyzing their accuracy and computational efficiency.
- Develop the mathematical framework for a new Multi-Sphere Method (MSM) and program necessary algorithms.
- Use a nonlinear fitting scheme to optimize the necessary parameters when populating the volume of simple shapes.
- Expand the MSM population with increasing numbers of spheres for increased accuracy, using a robust approach to place spheres uniformly on the geometry surface.
- Validate models by rigorously comparing the accuracy and computation times of the new methods to a higher order electrostatic solution.
- Modify the MSM framework to include insulating materials and conductors with a known total charge but unknown distribution.
- Apply the above methodology to more complex geometries and highlight the capabilities beyond the Coulomb attitude control concept.

**Research Goal 2 (Chapter 3-4):** Analyze all theoretical aspects of the 1-D remote electrostatic de-spin concept, validating expected outcomes with high fidelity simulations.

- Derive the dynamics of a simplified de-spin system, where a servicing craft approaches a cylindrical debris object to remove rotation in one dimension.
- Develop the nonlinear control algorithms required to remotely de-spin the cylinder, and analyze their Lyapunov stability.
- Simulate the 6DOF motion of the system to determine the baseline performance and requirements, and compare to results extrapolated from simplified models.
- Determine the effect of scaling various system parameters on system performance to determine optimal design criteria for future missions.
- Explore various relative position and orientation control schemes to determine whether they may improve the de-spin performance.
- Consider the possibility of removing rotation rates from small asteroid bodies in support of the Asteroid Retrieval Mission (ARM).
- Analyze the requirements of the charge transfer devices necessary to achieve the desired potential levels on both vehicles, and simulate the time dependent buildup of charge on the craft.

**Research Goal 3 (Chapter 5):** Verify the remote spacecraft attitude control concept by simplified terrestrial laboratory experiments.

- Survey previous terrestrial spacecraft motion testbeds and determine the requirements for an experiment to validate the de-spin theories developed above.
- Design and build the hardware necessary to permit low friction 1-D rotational motion of objects and verify the presence of torques between non-spherical charged objects.

- Create a software suite to control the high voltage potential levels on the objects and track the motion of the cylinder.
- Characterize the disturbances on the rotating cylinder and compare to Coulomb actuation capabilities.
- Test the performance of various rotation and attitude control algorithms and compare experimental results to computer simulations of the expected system motion.

In achieving these research tasks, the Coulomb attitude control technology has progressed from infancy to a TRL Level of 3-4. Directions for future research, in anticipation of eventual on-orbit validation are outlined in Chapter 6.

## Chapter 2

### Electrostatic Models

#### 2.1 Classical Electrostatic Models

In order to predict the dynamics of multiple charged bodies in space, knowledge of the forces and torques due to their electrostatic interaction is necessary. For the moment, consider all bodies to be composed of rigid conducting material, which is a reasonable assumption for the structural components of most spacecraft. In a conductor, electrons move around freely, resulting in a configuration where all charge resides on the body surface such that the electric field within the conductor is zero. The charge distribution is governed by Poisson's equation for electrostatics:

$$\nabla^2 \phi(\mathbf{x}) = -\frac{\rho(\mathbf{x})}{\epsilon_0} \quad (2.1)$$

where  $\phi$  represents the electrostatic potential,  $\rho$  is the volume charge density, and  $\epsilon_0 = 8.85 \times 10^{-12}$  F/m is the permittivity of free space. In the volume between the conducting bodies where the charge density is null, Poisson's equation reduces to Laplace's equation. Solving this for the electrostatic potential, where the physical geometries and applied voltages form the boundary conditions, allows one to determine the charge distribution from Poisson's equation. Since the electric field  $\mathbf{E}(\mathbf{x})$  is the gradient of the electrostatic potential, it is possible to determine the force contribution of every differential charge element by

$$d\mathbf{F} = dq\mathbf{E} \quad (2.2)$$



via which the mechanics of the system can be fully resolved. With the use of Legendre polynomials and Bessel functions, the second order partial differential Laplace equation can be solved for certain simple non-spherical geometries.<sup>85</sup> Multi-body systems or those with more complex geometries, however, cannot be solved analytically. Appendix A discusses how electric field or charge distribution sensing could be used to determine the electrostatic forces acting on a spacecraft.

Early analysis of in-orbit satellite formations modeled the charged bodies as point charges experiencing forces according to Coulomb's law.<sup>9,50,55</sup> Later, spacecraft were represented by conducting spheres,<sup>79</sup> and the mutual capacitance relationship was used to determine the charge on each sphere given its voltage as prescribed by the charge control devices discussed earlier.<sup>85</sup> Realistically, spacecraft components such as solar panels and communication antennae result in geometries that are far from spherical. An Effective Sphere Method (ESM) was developed to determine what size sphere optimally approximates the capacitance of a given 3D shape,<sup>35</sup> but even in spheres, induced charging effects result in non-symmetric charge distributions that yield large errors at small separation distances. Most importantly, these approaches fail to capture the electrostatic torques and off-axis forces that result from non-symmetric spacecraft bodies flying at small separation distances. Resolving these higher order interactions is crucial in order to develop the remote electrostatic de-spin technology.

As with other disciplines governed by partial differential equations, numerical methods are available in electrostatics to provide a computationally expensive but highly accurate solution of the system. Finite Element Analysis (FEA) software can be used to compute a linearized approximation of Eq. (2.1) on numerous finite elements distributed throughout the entire 3D space. Global boundary conditions are formed from the spacecraft geometries and electrostatic potentials, while the local boundary conditions of each element are prescribed to match those of its neighboring elements. Once the linearized fields are solved, charge distributions and the resulting forces are derived using a discretized form of Eq. (2.2). Even at low accuracies, it takes a desktop computer on the order of minutes to determine the electrostatic forces and torques present in a single configuration of a two-body system. Clearly, 6DOF charged relative motion simulations are not feasible at

this computation speed, nor is it possible to gain analytical insight into the dynamics and control of such scenarios.

Therefore, a niche exists for a novel electrostatic model that is computationally efficient but retains enough spacial fidelity to resolve off-axis forces and torques. The Multi-Sphere Method (MSM) attempts to bridge the gap in accuracy and computation time between the simplified models and FEA approaches discussed above, as depicted qualitatively in Figure 2.1. In this new method, a generic spacecraft shape is modeled by a collection of conducting spheres. Computation is limited to inverting an  $[n \times n]$  matrix (where  $n$  is the number of spheres in the system) to determine the charge on each sphere, and forces and torques are subsequently predicted by summation of the contribution of each sphere by Coulomb's law. The electrostatic charge essentially distributes itself among the spheres as determined by their geometry, much like it does with infinite freedom in a generic conducting geometry. As such, the model is robust for various orientations and separation distances between objects. Multiple population densities are possible, and increasing the number of spheres results in greater accuracy at the cost of increased computation time.

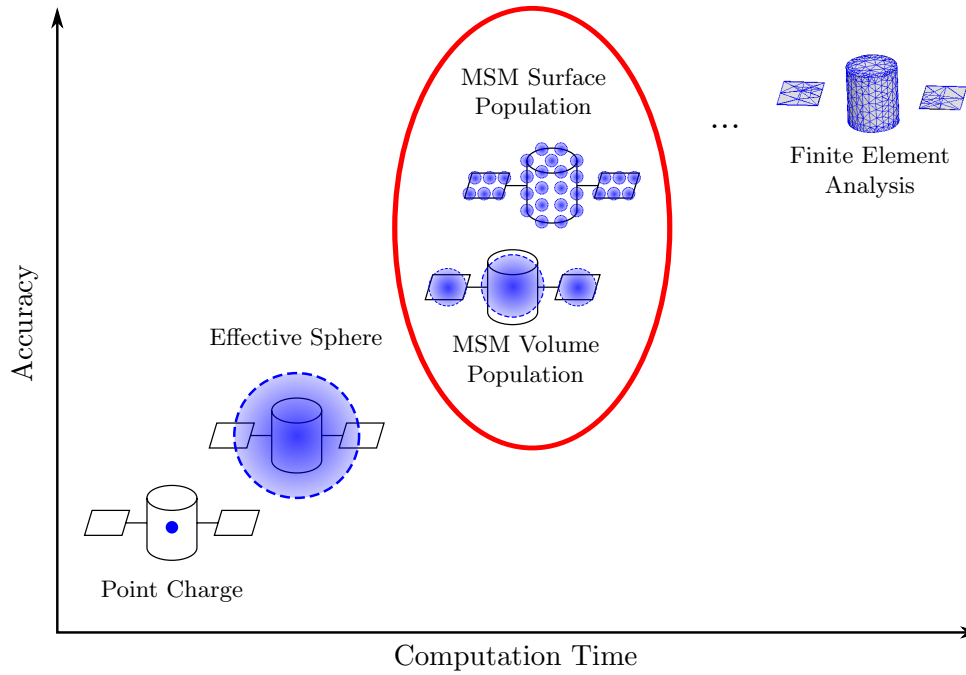


Figure 2.1: Comparison of various electrostatic models

## 2.2 Multi-Sphere Method

The Multi-Sphere Method, a novel electrostatic model developed during this research effort, uses a collection of conducting spheres to model a rigid 3D shape. Figure 2.2 depicts a representative satellite  $A$ , modeled by  $n$  spheres. Optimal selection of the sizes and locations of the sphere is discussed in the following section. The goal here is to determine the electrostatic interaction of the satellite with another charged object  $B$ , which is modeled for simplicity by a single sphere. The finite spheres in satellite  $A$  remain fixed with respect to some selected origin  $O$ , constrained to match the translation and rotation dynamics of the actual body.

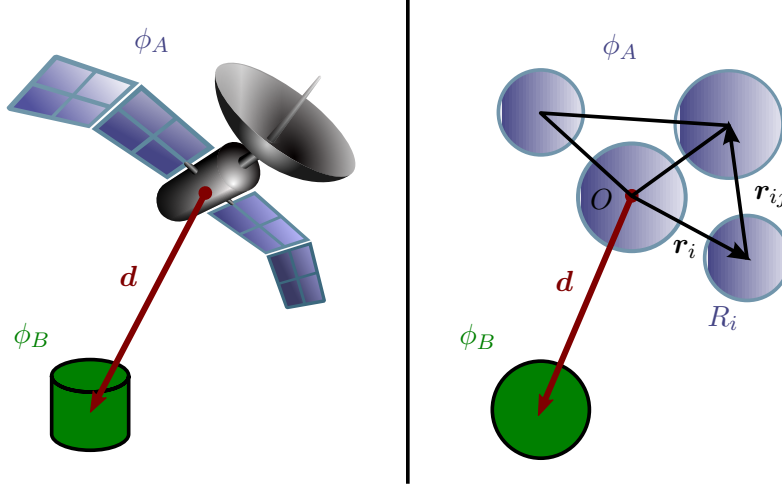


Figure 2.2: Conceptual depiction of the Multi-Sphere Method

As discussed in the Introduction, charge control devices may be used to prescribe a specific electrostatic potential on a given satellite. Here it is assumed that both objects have been brought to some voltage levels  $\phi_A$  and  $\phi_B$ . Meanwhile, the Coulomb forces between the spheres depend on the charge that each holds, which can be deduced from their relative sizes and positions. The voltage  $\phi_i$  on a given sphere is related to the charge  $q_i$  on that sphere and the charges on its neighboring spheres. This relation is governed by Eq. (2.3),<sup>85</sup> where  $R_i$  represents the radius of the sphere in question and  $\mathbf{r}_{i,j} = \mathbf{r}_j - \mathbf{r}_i$  is the center-to-center distance to each neighbor. The

constant  $k_c = 8.99 \times 10^9 \text{ Nm}^2/\text{C}^2$  is Coulomb's constant.

$$\phi_i = k_c \frac{q_i}{R_i} + \sum_{j=1, j \neq i}^m k_c \frac{q_j}{r_{i,j}} \quad (2.3)$$

This relationship is most valid when  $r_{i,j} \gg R_i$ . When the spheres are large and closely spaced, the charge on both spheres is attracted or repelled by that of the neighboring sphere, resulting in a nonuniform distribution on the surface. This induced charge effect causes the effective separation distance to be altered, which is not captured by Eq. 2.3. As more spheres are introduced and their size decreases relative to the system size, results become more accurate.

The linear relations in Eq. (2.3) can be combined for each of the  $m = n + 1$  spheres in the system in Figure 2.2, resulting in the matrix equation in Eq. (2.4). Here  $\boldsymbol{\phi} = [\phi_A, \phi_A, \dots, \phi_A, \phi_B]^T$  and  $\mathbf{q} = [q_1, q_2, \dots, q_n, q_B]^T$  represent matrix collections of the voltages and charges in the entire system.

$$\boldsymbol{\phi} = k_c [C_M]^{-1} \mathbf{q} \quad (2.4)$$

The inverse of the Position Dependent Capacitance (PDC) matrix  $[C_M]^{-1}$  is expanded as follows, where  $\mathbf{r}_{i,B} = \mathbf{d} - \mathbf{r}_i$ :

$$[C_M]^{-1} = \begin{bmatrix} 1/R_1 & 1/r_{1,2} & \cdots & 1/r_{1,n} & 1/r_{1,B} \\ 1/r_{2,1} & 1/R_2 & \ddots & \vdots & \vdots \\ \vdots & \ddots & \ddots & \vdots & \vdots \\ 1/r_{n,1} & \cdots & \cdots & 1/R_n & 1/r_{n,B} \\ 1/r_{B,1} & \cdots & \cdots & 1/r_{B,n} & 1/R_B \end{bmatrix} \quad (2.5)$$

Note that the model for body  $B$  could contain multiple spheres or extra bodies could be present in the system, in which case the extra spheres are appended to the above matrix relation. Moreover, if there is a voltage differential present on any of the modeled spacecraft, the corresponding spheres can be held at different voltages.

The next step is to solve for the array of charges  $\mathbf{q}$  from Eq. (2.4) by inverting this  $n + 1$  size symmetric matrix, a computation that is straightforward but becomes increasingly expensive when more spheres are used in the model. Coulomb's law can then be implemented to calculate

the linear force between each charged sphere. Since the location of the spheres within the modeled body are held fixed with respect to each other, their equal and opposite contributions cancel. The total force  $\mathbf{F}$  and torque  $\mathbf{L}$  about the origin  $O$  on body  $A$  due to the object  $B$  is given by the following summations:

$$\mathbf{F}_A = -k_c q_B \sum_{i=1}^n \frac{q_i}{r_{i,B}^3} \mathbf{r}_{i,B} \quad (2.6)$$

$$\mathbf{L}_A = -k_c q_B \sum_{i=1}^n \frac{q_i}{r_{i,B}^3} \mathbf{r}_i \times \mathbf{r}_{i,B} \quad (2.7)$$

While any origin  $O$  can be chosen for body  $A$ , the force and torque in Eqs. (2.6) and (2.7) are now defined from this reference origin.

If the MSM of object  $B$  contains multiple spheres or there are other bodies present, there is an extra summation over all spheres that are external to body  $A$ , as follows:

$$\mathbf{F}_A = -k_c \sum_{j=1, j \notin A}^m \sum_{i=1}^n \frac{q_i q_j}{r_{i,j}^3} \mathbf{r}_{i,j} \quad (2.8)$$

$$\mathbf{L}_A = -k_c \sum_{j=1, j \notin A}^m \sum_{i=1}^n \frac{q_i q_j}{r_{i,j}^3} \mathbf{r}_{i,j} \times \mathbf{r}_{i,B} \quad (2.9)$$

The MSM algorithm described above can be executed in most any computing language. The MATLAB software suite from Mathworks, Inc.<sup>©</sup> is used predominantly for this research effort due to its proficiency in matrix manipulation. To manage the translation and rotation of the bodies, a rigid kinematics toolbox with attitude transformation subroutines was utilized.<sup>71</sup> The code is given in Appendix B, with the constant charge modification capabilities explained in Section 2.8 included.

### 2.3 MSM Volume Population

Given the mathematical framework of the Multi-Sphere Method, the challenge of choosing an appropriate set of spheres for a given spacecraft geometry remains. When considering simple shapes, the logical approach is to populate the volume of the geometry with a relatively small number of spheres. For every sphere used in the model, 4 parameters must to be determined: 3

spatial coordinates along with the sphere radius. When the symmetry properties of the modeled geometry are matched by the MSM spheres, the parameter space can be greatly reduced. The goal then is to find an optimal solution for these parameters such that the MSM output matches the results of some truth model such as the high accuracy FEA solvers discussed previously. Out of the wide range of commercially available electrostatic modeling software, Ansoft Maxwell 3D<sup>®</sup> is chosen for verification of the MSM due to its ability to resolve various field parameters (such as surface charge distribution, force and torque), parameter sweep capabilities, computationally efficient mesh refinement, and relative ease of use.

Throughout this body of work, a 3 m length by 1 m diameter cylinder is extensively used as the space object of interest. This simple yet distinctly non-spherical geometry is very effective in highlighting the dynamics and control challenges of 1D Coulomb attitude control. Moreover, numerous space debris objects with cylindrical shapes have been identified, such as the once-popular GEO dual-spinner satellites and various upper stage rocket engines like the Centaur. The cylinder is modeled as a perfect conductor in Maxwell 3D as shown in Figure 2.3(a). Since the goal is to accurately predict the Coulomb forces and torques on a body with the MSM, a charged external sphere is introduced in the system. The forces and torques that result when this sphere is positioned at various locations around the cylinder, as in Figure 2.3(b), constitutes the truth data for the regression analysis to optimize the sphere parameters. A voltage excitation of  $\phi = +30$  kV is prescribed on both objects in the simulation, while a sufficiently far removed external surface is held at zero voltage to complete the boundary conditions.

Since execution of the MSM algorithm involves inversion of the capacitance matrix followed by a complex summation operation, it is not possible to perform a linear regression to determine the optimal solution of the sphere parameters. Instead, a Gaussian least squares differential correction method is used,<sup>36</sup> also implementing a finite difference method to determine the partial derivatives of the model output function with respect to the parameters. The input to the regression is the external sphere position, the outputs are the force and torque values on the modeled body for that external sphere position, and the parameters are the sphere positions and sizes. Bisquare weights

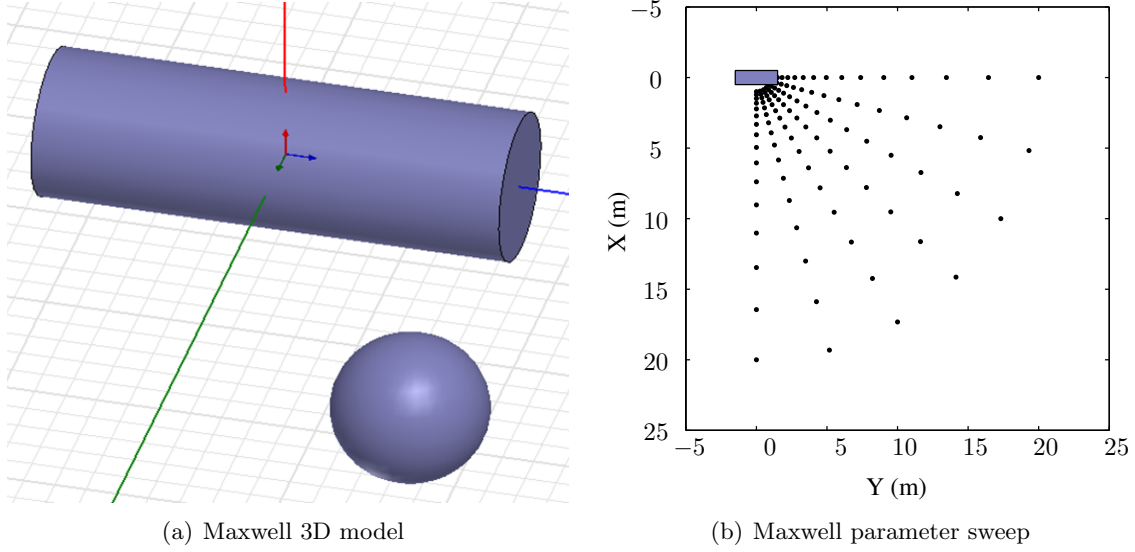


Figure 2.3: Maxwell 3D model and parameter sweep for data export

are used, which seek to find a curve that fits the bulk of the data using the usual least-squares approach, while minimizing the effect of outliers.<sup>23,34</sup> Moreover, the relative weight of each data point can be prescribed which is useful if fitting to the correct forces is more important than obtaining accurate torques, for example.

The nonlinear regression described above is executed to determine the optimal parameters of a three-sphere model for the aforementioned 3 m x 1 m cylinder. Due to symmetry arguments, the parameter space is reduced from 12 to just 3 values. A manual search is used to determine an appropriate set of initial parameters. The parameters of the resulting MSM spheres are listed in Table 2.1, while the model is shown superimposed on the actual cylinder geometry in Figure 2.4. Although the spheres intersect each other in physical space, this does not present a problem in the framework of the MSM. Numerical verification of the solution is presented together with that of another model in Section 2.5.2. In Appendix C, the MSM results are compared to the FEA solution as certain parameters such as shape sizes and applied voltages are varied. This ensures that the model is robust to such variations and can be implemented in a range of simulation scenarios.

Table 2.1: Parameters of three-sphere MSM for cylinder geometry

	Sphere 1	Sphere 2	Sphere 3
X Coordinate (m)	0	0	0
Y Coordinate (m)	-1.1454	0	1.1454
Z Coordinate (m)	0	0	0
Radius (m)	0.5959	0.6534	0.5959

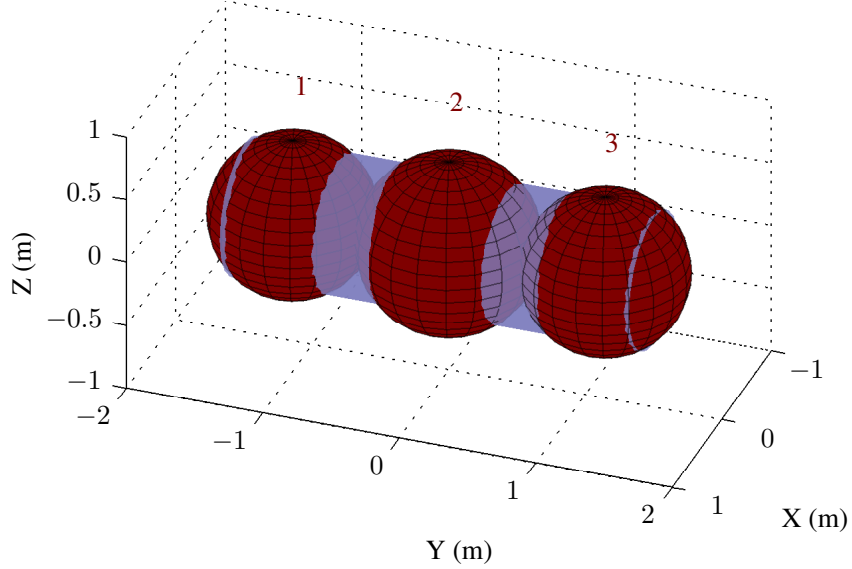


Figure 2.4: Three-sphere MSM parameters for cylinder geometry

## 2.4 MSM Surface Population

While the Volume population method for the MSM (VMSM) works well to predict the electrostatic interactions of the cylinder shape, capturing the 3D and induced charge effects of more intricate geometries at small separation distances requires a model with more than three spheres. Increasing the number of spheres leads to a higher fidelity prediction of the electrostatic interactions because there is more freedom for redistribution of the charge between the various spheres in the model, much like there is on the surface of an actual conducting object. In this way, induced charge effects can be captured in any dimension where multiple spheres are present.

The MSM algorithm for calculating forces and torques can handle models with large numbers



of spheres, but the nonlinear fitting scheme used to optimize the sphere positions and sizes is not robust in this domain. As with any nonlinear fitting algorithm, when the parameter set increases, successful convergence is dependent on the chosen initial conditions and global optimization is not guaranteed. Since the underlying assumption that the modeled body is fully conducting remains, it is known that all the contained charge will reside on its surface. Therefore, the approach is taken to populate only the surface of a given shape with spheres.

In order to minimize the parameters that need to be selected when creating the MSM, it is desirable to pick a set of spheres that are uniformly distributed along the surface of the geometry. For complex shapes this is not a trivial task, but several CAD programs contain algorithms to generate uniform point clouds from solid models. For simple shapes like spheres and cylinders, specific algorithms are created to uniformly populate the surface. By this approach, the Surface populated MSM (SMSM) method is significantly faster and more robust to set up than the VMSM. Since execution of the MSM requires inversion of an  $[n \times n]$  matrix and an  $n^2$  summation operation, increasing the number of spheres increases the computation time. However, the resulting solutions are much more accurate, and run-time costs are still significantly lower than for FEA calculations.

With the spheres in the MSM positioned in a uniform manner on the surface of the modeled geometry, the one remaining parameter to choose is the spheres' radius  $R$ , which is assumed constant throughout the SMSM model. Only one scalar invariant quantity is necessary to determine an optimal radius, which varies with the spacing of the spheres on the surface. The self-capacitance of an isolated conductor is dependent only on its geometry, and is therefore a good candidate quantity for determining the optimal sphere radius  $R$ . For complex shapes the capacitance can be found numerically by a higher order electrostatic modeling program such as Maxwell 3D. Meanwhile, the capacitance of the MSM body can be computed by summation of the charge  $q_i$  on each sphere in the model for a given voltage  $\phi$ :

$$C_{\text{MSM}} = \frac{Q}{\phi} = \frac{\sum_{i=1}^n q_i}{\phi} \quad (2.10)$$

An optimizing function based on a golden section search and parabolic interpolation<sup>14,25</sup> is used to

choose a radius  $R$  that minimizes

$$f(R) = C_{\text{MSM}} - C_{\text{num}} \quad (2.11)$$

The methodology for determining the sphere parameters for a generic spacecraft shape is summarized in Figure 2.5. The red boxes are processes that must be executed when analytic solutions are not present for the uniform sphere distribution and capacitance, as is most often the case. The two components of a full MSM are the location  $\mathbf{r}_i$  and radius  $R_i$  of each sphere. For a generic body, a solid modeling program will be necessary to determine a uniform point cloud model on the surface. For most shapes, the capacitance is to be found by an electrostatic modeling program such as Maxwell 3D. The PDC matrix is then used to calculate the capacitance for the system of spheres to determine an optimal uniform radius  $R$  that matches the capacitance from the numerical solution. At this point, the full model can be used in conjunction with other MSM objects to calculate electrostatic interactions.

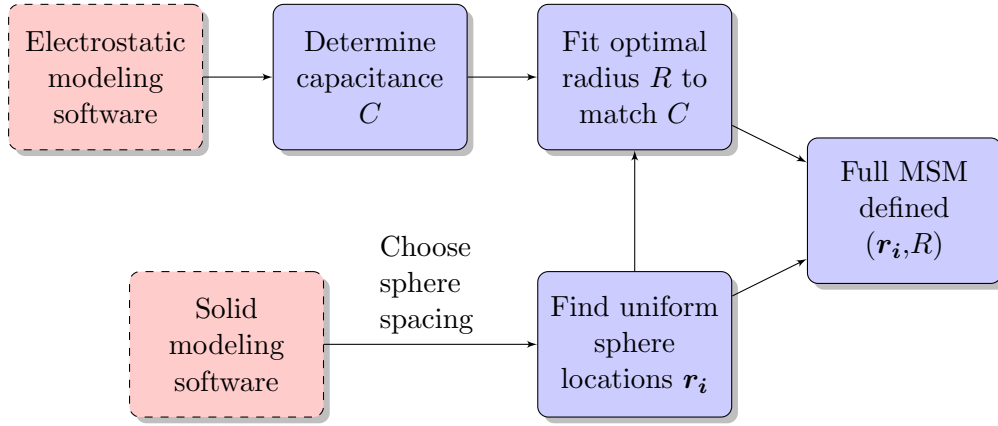


Figure 2.5: Methodology for parameter selection of surface populated MSM

## 2.5 MSM Numerical Verification

### 2.5.1 Two-Sphere System

To verify the accuracy of the Multi-Sphere Method, its output must be compared to higher fidelity solutions. First, a simple system with two charged conducting spheres is considered, because

several analytic solutions exist for comparison. The two spheres are chosen to have a radius  $R_S = 0.5$  m while the separation distance  $d$  is varied, and equal as well as opposite sphere voltages  $\phi = \pm 30$  kV are considered. The Position Dependent Capacitance (PDC) model, as in Eq. 2.3, captures the relationship between the prescribed voltage and the total charge on each sphere, but not the induced charge effects. The two approaches in Figure 2.6 attempt to offset this anomaly by ensuring that the spheres form equipotential surfaces. They are valid only for a system where both conducting spheres are of equal radius and are held at equal magnitude voltages, as is the case here.

The first order induced charge model, shown in Figure 2.6(a), attempts to capture induced effects by a one dimensional change in separation distances. The separation  $d$  between the charges  $q_A$  and  $q_B$  that are computed using the PDC matrix, is adjusted by an extra distance  $x$ . This distance is chosen such that  $\phi_L$  and  $\phi_R$  are equal, resulting in a cubic equation in  $x$ .<sup>81</sup> The figure shows an increased separation as for the repulsion case; attraction would result in a decreased separation distance.

In Soules' Method of Images (MOI), illustrated in Figure 2.6(b), successively smaller image charges  $q_i$  are placed at distances  $x_i$  along the line of centers to approximate the induced charged distribution:<sup>86</sup>

$$q_i = \pm \frac{r q_{n-1}}{d - x_{n-1}} \quad (2.12a)$$

$$x_i = \frac{R_S^2}{d - x_{n-1}} \quad (2.12b)$$

Here  $n > 1$ ,  $q_1$  is determined for a given voltage using the PDC model, and  $x_1 = 0$ . In Equation (2.12b), the successive charges switch polarity  $(-)$  for the repulsion case and maintain the same polarity  $(+)$  for attraction.<sup>84</sup> The algorithm is implemented using 19 spheres as in Reference 81.

While the two induced charge models discussed above provide a vast improvement over the PDC model in force prediction at small separation distances, Maxwell3D is found to produce the most accurate solution when the simulation is tuned properly. Therefore the Maxwell3D solution is

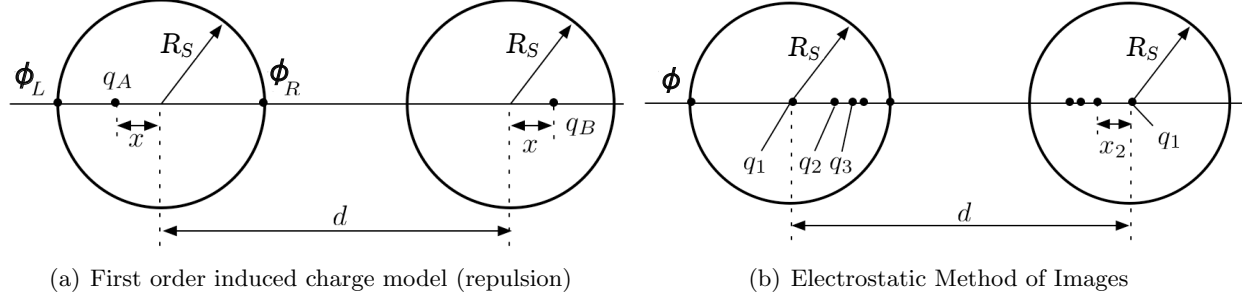


Figure 2.6: Two analytic models for the two sphere system that capture induced effects

used as the truth model for verification of the surface populated Multi-Sphere Method. The mesh and charge distribution is visible in Figure 2.8(a).

To develop a MSM for a spherical geometry by the process in Figure 2.5, it is necessary to uniformly populate the surface of a sphere with equidistant points, which is a well documented computer science problem.<sup>5</sup> A Golden Section Spiral is used to divide the sphere into parallel bands of equal width, and points are placed along the spiral at successive longitudes separated by the golden angle:

$$\psi = \pi(3 - \sqrt{5}) \quad (2.13)$$

The figure below shows the resulting sphere population for  $n = 4, 10$  and  $30$  spheres.

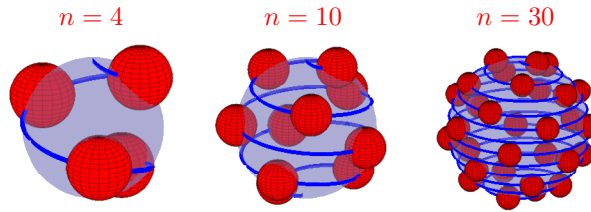


Figure 2.7: Various uniform point distributions on the surface of a sphere

Next, the optimal  $R$  is determined by minimizing the relation in Eq. 2.11. For a sphere with radius  $R_S$ , the self-capacitance is analytically known to be  $C_{\text{sphere}} = R_S/k_c$ . For the two sphere

densities used, the following radii are determined:

$$R \text{ (10 spheres)} = 0.1460 \text{ m} \quad (2.14)$$

$$R \text{ (30 spheres)} = 0.0835 \text{ m} \quad (2.15)$$

As the number of spheres in the model increases, the total surface area on the optimized MSM spheres is shown in Appendix D to converge to a single value, giving further credence to the capacitance fit.

Figure 2.8 shows the charge density distribution in both Maxwell3D and on a 30 sphere surface populated MSM. The charge densities are normalized to the total surface area. This result qualitatively highlights the ability of the SMSM to capture induced charge effects when enough spheres are present on the object surface.

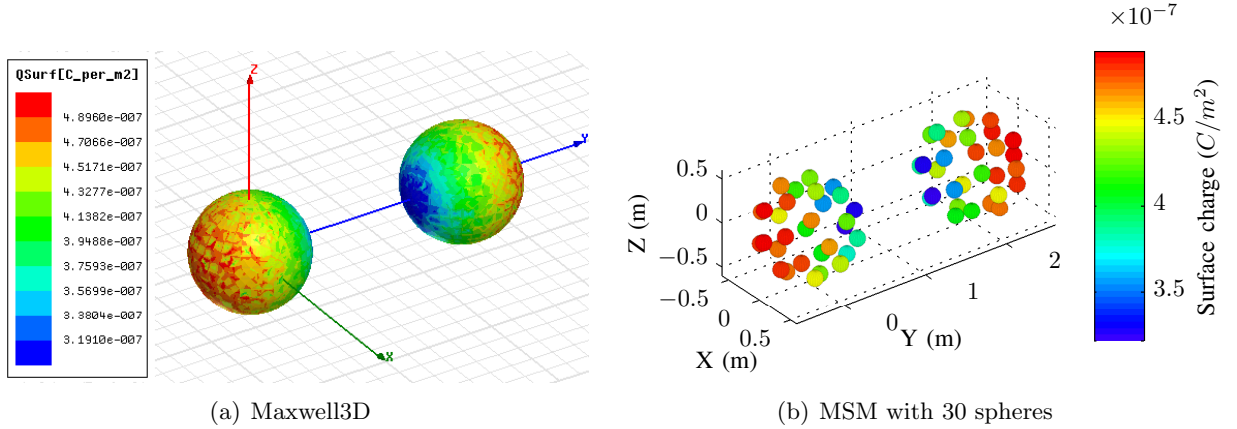


Figure 2.8: Charge density distribution on two spheres ( $\phi_1 = \phi_2 = +30 \text{ kV}$ )

Figure 2.9 gives the percent error for various models at a range of separation distances, for the repulsive and attractive cases (2.9(a) & 2.9(b), respectively). Percent error is defined as

$$Err = \frac{F_{\text{model}} - F_{\text{Maxwell}}}{F_{\text{Maxwell}}} \quad (2.16)$$

The PDC model produces almost 50% error at very small separation distances, but matches the full solution well at further distances. While the Maxwell 3D solution is used as the truth model, the slight disagreement with the Method of Images solution is surprising, since this approach should

closely represent the full series solution according to Reference 84. As more spheres are added to the MSM however, the errors at close distances converge to zero, thus giving further credence to the solution given by Maxwell 3D. The first order induced charge method matches Maxwell 3D for the repulsion case but is equivalent to the Method of Images for the attractive case, which is likely a coincidence.

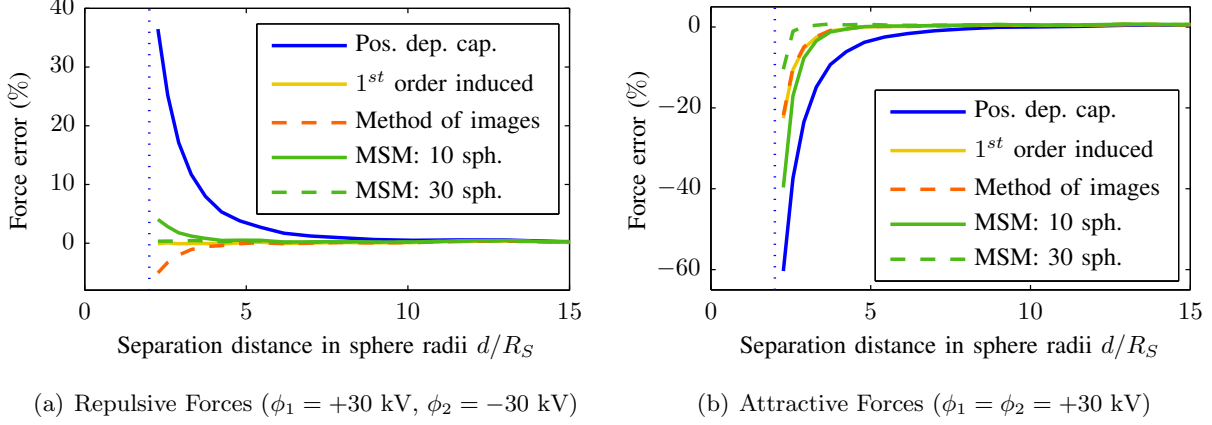


Figure 2.9: Error in force between two spheres for various electrostatic models

The SMSM with 30 spheres results in less than a percent error for repulsion right up to where the spheres touch at  $d = 2R_S$ . For attraction, induced effects are known to be even more dominant, and more spheres are necessary to completely capture these effects. The PDC model shows nearly twice as much error with attraction as for the repulsion case. The 10 sphere SMSM results in up to 40% error as the spheres nearly touch, but this drops off quickly to less than 2% when  $d = 3.5R_S$ . All in all, the surface populated MSM is clearly shown to model the electrostatic interactions of the spheres to a very high degree of accuracy. It provides a more accurate solution than other induced charge effect models, while increasing in accuracy as more spheres are added. Moreover, this method is expandable to generic spacecraft shapes where the others are not. The effect of the radii of the spheres in the SMSM model on the resulting forces is investigated in Appendix D.

### 2.5.2 Cylinder Sphere System

We return now to the system with a 3 m length by 1 m diameter cylinder and a 1 m diameter sphere that was used to determine optimal sphere parameters for the VMSM. The Maxwell 3D force and torque data over the range of sphere locations in Figure 2.3(b) is extensively compared to the output of both volume and surface populated MSM configurations. For the SMSM, the methodology in Figure 2.5 is again implemented to create a SMSM model for the cylinder. Since this shape is still fairly simple, manual algorithms are used to populate the surface. For the end discs, a gold section spiral is utilized much like for populating the spheres in Figure 2.7, while on the circumference of the body, hexagonal packing is implemented. Maxwell 3D is used to determine that the self capacitance of the cylinder in space is

$$C_{\text{cylinder}} = 1.0616 \times 10^{-10} \frac{C}{V} \quad (2.17)$$

This is used to fit the optimal sphere radius, resulting in a cylinder model with  $n = 105$  spheres ( $R = 0.0731$  m) and a sphere model with  $n = 30$  spheres as above ( $R = 0.0835$  m). In Figure 2.10, where both objects are held at  $\phi = +30\text{ kV}$ , the induced charge effects are clearly visible from the charge distribution throughout the shapes.

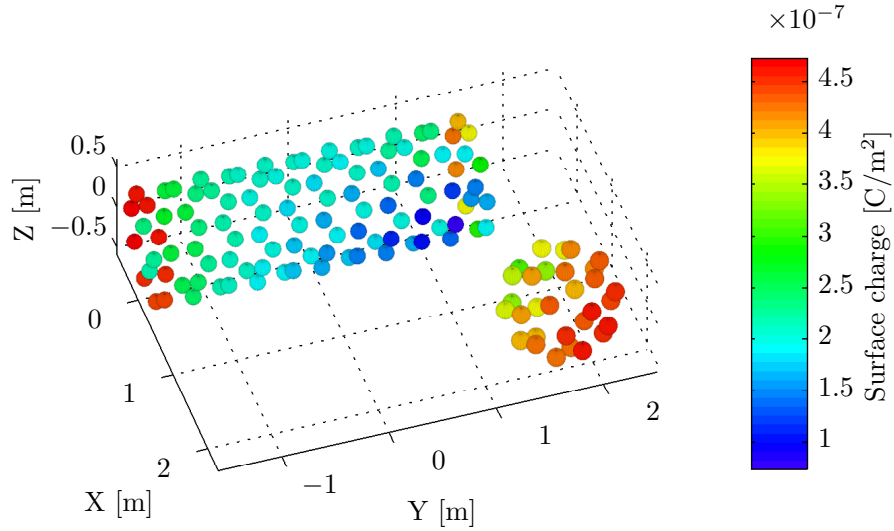


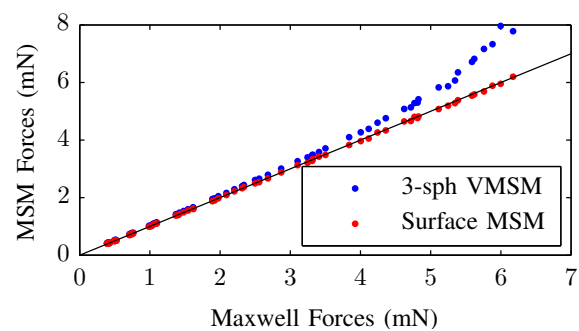
Figure 2.10: Charge density distribution on SMSM of cylinder and sphere ( $\phi_1 = \phi_2 = +30$  kV)

Figure 2.11 shows the accuracy of the force and torque (left and right), calculated by the VMSM model with three spheres and the surface populated model (105 spheres in the cylinder and 30 spheres in the sphere), compared to the truth data from Maxwell 3D. Figures 2.11(a) and 2.11(b) are 1 to 1 plots between the MSM models and the Maxwell 3D data, where the black line represents perfect matching between the two models. The three sphere VMSM over-predicts the larger forces that correspond to small separation distances. The drawback of this visualization is that it isn't possible to see where in relation to the cylinder the sphere is located for a given data point. Figures 2.11(c) - 2.11(f) rectify this shortcoming, as they show the absolute force and torque errors compared to Maxwell 3D, for the three sphere and surface populated MSM, respectively. A representative size cylinder and sphere are included for reference, while the color legend is in logarithmic scale.

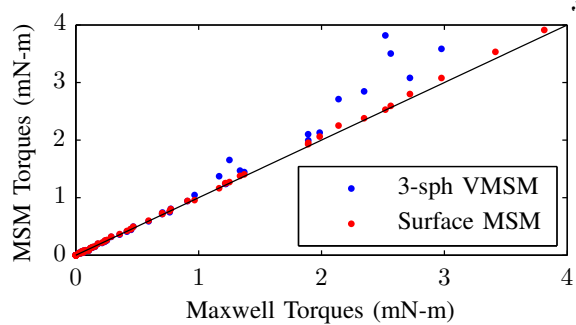
It is clear from the figures that the SMSM predicts the forces much better at small separation distances across the range of angles, but by about 6 m separation (12 craft radii), the difference between the two models is fairly negligible. For the case of torques, the three sphere model actually does a slightly better job at separation distances larger than 4 m (8 craft radii). This is encouraging for executing lengthy 6 Degree of Freedom (6DOF) simulations, where the SMSM model might still be time prohibitive. Most Coulomb charge control applications that don't involve docking occur at separation distances beyond this range.

It is important to weigh the accuracy with computation and setup times of the different models, as shown in Table 2.2. The first column gives the time for each model to compute a force and torque value at each of the 82 relative positions. While this computation takes Maxwell 3D about 1 hour and 14 minutes at fairly moderate accuracy settings, the MSM with three spheres completes the task in a fraction of a second. Meanwhile, it takes the surface populated model (with 135 spheres in the system) about 16 seconds. The next column shows the numerical calculation time necessary for the setup of the two MSM models. For the volume populated (3-sphere) MSM, this requires the complete set of data calculated earlier by Maxwell 3D, while the surface populated MSM only requires a single numerical computation of the capacitance of the body. The 'Fit'

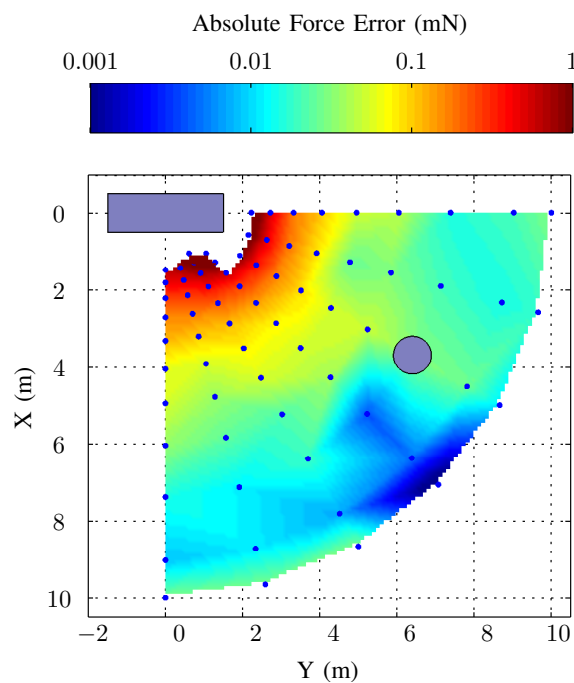




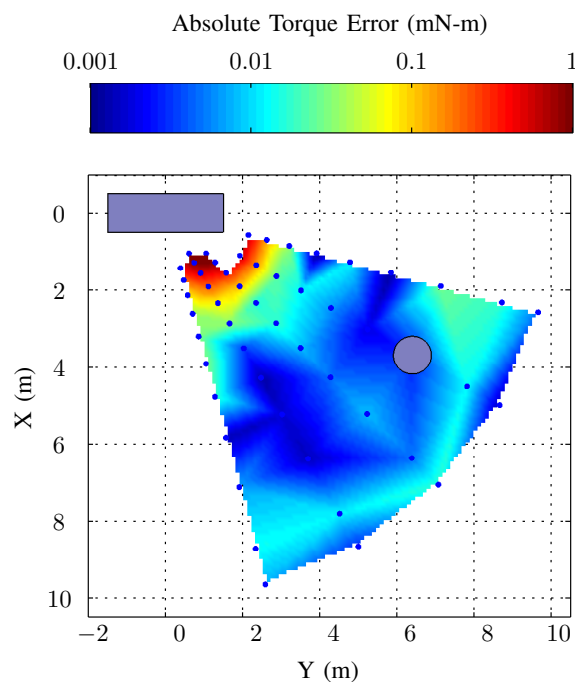
(a) Forces compared to Maxwell3D



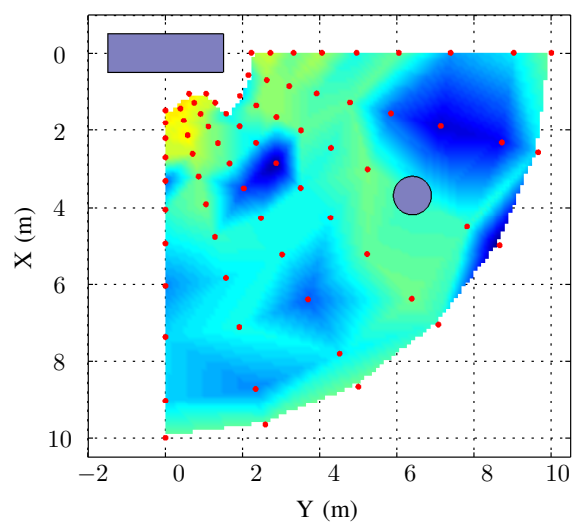
(b) Torques compared to Maxwell3D



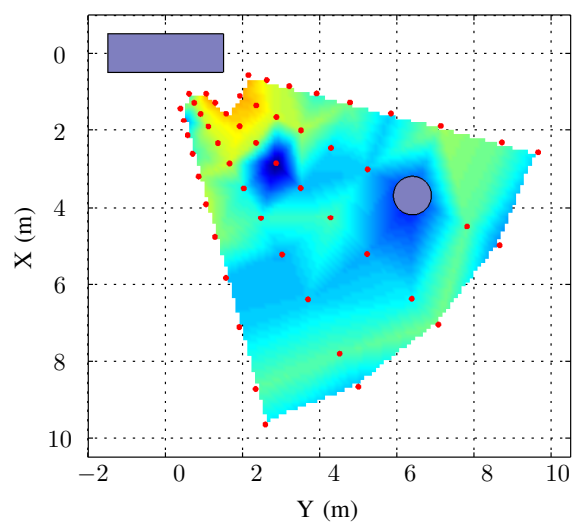
(c) 3-sphere VMSM force errors



(d) 3-sphere VMSM torque errors



(e) Surface MSM force errors



(f) Surface MSM torque errors

Figure 2.11: Force and torque comparison between MSM models and Maxwell3D

column represents the complex nonlinear fit for the 3-sphere VMSM, and determination of the sphere positions as well as a fit to match  $R$  to capacitance for the surface populated model. As is clear, computation happens about an order of magnitude quicker for the VMSM, but setup is two orders of magnitude quicker for the SMSM model. Depending on the requirements on accuracy and computation time, both approaches are viable for use in the calculation of spacecraft electrostatic interactions. Both exceed Maxwell 3D or other FEA software in the ability to predict forces and torques in real time.

Table 2.2: Setup and computation time for calculation of force and torques between sphere and cylinder at 82 relative locations

[Time in sec]	Comp.	Setup				
Maxwell3D	4434	Num.	Fit	Total		
3-sph VMSM	<b>0.11</b>	4434	+	9.1	=	<b>4443.1</b>
Surface MSM	<b>15.6</b>	54.1	+	4.1	=	<b>58.2</b>

## 2.6 Boundary Element Method

Comparison to higher order numerical solutions in this work has been focused predominantly on finite element methods that solves Laplace's equation  $\nabla^2 \phi(\mathbf{x}) = 0$  on the free space domain outside the conducting bodies. While this numerical approach is capable of providing very high accuracy solution, the Boundary Element Method (BEM)<sup>13,19,27,28</sup> is another method with considerable similarities in its mathematical formulation to the SMSM. The BEM differs from FEA in that unknowns are solved on the boundary of the domain, i.e. on the surface of conducting elements, not unlike the SMSM.

Applying Green's function to Laplace's equation on some surface  $S$  with normal  $n$  results in:<sup>13</sup>

$$\phi(\mathbf{x}) = \int_S \left[ G(\mathbf{x}, \mathbf{x}') \frac{\partial \phi}{\partial n}(\mathbf{x}') - \frac{\partial G}{\partial n}(\mathbf{x}, \mathbf{x}') \phi(\mathbf{x}') \right] dS(\mathbf{x}') \quad (2.18)$$

where the Green's function  $G$  for the Laplacian in 3D is

$$G(\mathbf{x}, \mathbf{x}') = \frac{1}{4\pi|\mathbf{x}' - \mathbf{x}|} \quad (2.19)$$

At this point the boundary of the domain is discretized using a set of basis functions to obtain a solution of the charge distribution  $\sigma$  (which is manifested in Eq. 2.18 in the  $\frac{\partial\phi}{\partial n}(\mathbf{x}')$  term). If Neumann boundary conditions are prescribed on the entire boundary, the second term in the integral in Eq. 2.18 disappears and this relation can be discretized to the following matrix form

$$A\boldsymbol{\lambda} = \mathbf{b} \quad (2.20)$$

where  $\boldsymbol{\lambda}$  contains charge distribution ( $\sigma$ ) values on the elements and  $\mathbf{b}$  is a column with the resulting surface voltage  $\phi$  on a central point at each element. The matrix  $A$  is populated with analytic solutions to the following integral that results from Eq. 2.18 for every combination of two surface elements:

$$\phi(\mathbf{x}) = \int_S \frac{\sigma(\mathbf{x}')}{4\pi\epsilon|\mathbf{x} - \mathbf{x}'|} dS(\mathbf{x}') \quad (2.21)$$

The formulation is similar to the capacitance matrix of the MSM, but if complex basis functions are used in the BEM, populating  $A$  becomes tedious and time consuming, in which case the SMSM provides a much simpler approach.

In its simplest form, the BEM can be implemented using the following simplifications:<sup>27</sup>

- (1) Within each element, assume that the charge density has a constant value so that  $\sigma$  is piecewise constant over the surface.
- (2) Use a centroidal approximation with the charge in the adjacent element concentrated at a center point in the patch to solve Eq. 2.21.

In this case, the off-axis terms in the matrix  $A$  simplify to  $k_c/r_{i,j}$  as in the MSM capacitance matrix, while equating Eq. 2.21 for the self-terms (diagonal elements of the matrix) results in a geometry-dependent constant. This constant is analogous to the sphere size chosen in the SMSM.

Considering this simplified form of the BEM, the two methods require the same  $O(N^2)$  inversion operation to solve for a set of charges on the boundary of the system, but some fundamental differences remain. First, setup in the SMSM is simpler because the self-integral for various element geometries (which can be computationally intensive for curved elements) is omitted; instead, a constant sphere size is determined from the single free space capacitance value used from a truth model. Further, if so desired, selection of sphere placement and size in the SMSM can be tuned to capture certain electrostatic characteristics, where the BEM is limited to a set of surface elements that span the entire boundary but do not overlap. This is an especially important distinction when considering sharp edge and corner features. In this case, spheres in the SMSM can be placed exactly along or on such features where the charge is expected to be highest, thus capturing the charge concentration at the right location. The BEM meanwhile is limited to elements that border the sharp feature rather than being located on it, even if the mesh is discretized to be denser at such locations. This benefit of the SMSM is especially evident when a relatively small number of sphere / elements is used to capture the charge distribution on a given body. The surface populated BEM, for example, could not capture off-axis forces and torques on a cylinder using only three elements, as is possible with the VMSM.

## 2.7 Satellite Model

To demonstrate the ability of the MSM to model spacecraft geometries more complex than the cylinder and sphere configurations used for verification, a simple satellite with a cylindrical chassis and two rectangular solar panels is created. The procedure outlined in Figure 2.5 is used to create separate models for the chassis and the solar panels. Capacitances are determined using Maxwell 3D, and the sphere spacing is chosen using constant separation algorithms. The resulting MSM model is shown in Figure 2.12. While a similar spacing is used between spheres, the solar panel spheres are much larger than that on the spacecraft body. This is because they effectively capture twice the surface area since the panels are 2D surfaces. Because of the sharp corners and edges on the satellite geometry, it contains numerous charge concentrations. If extremely sharp

corners are present at large negative voltages, natural field emission of electrons could occur.<sup>95</sup> For the voltages considered in this study, sub millimeter curvatures would be required for such emission. The electric fields resulting from this satellite model are considerably different than a simple cylinder of comparable size held at the same voltage. While the cylinder geometry is used throughout the rest of this dissertation to analyze various aspects of satellite attitude control, similar arguments can be made for more complex spacecraft geometries like the simple satellite considered here.

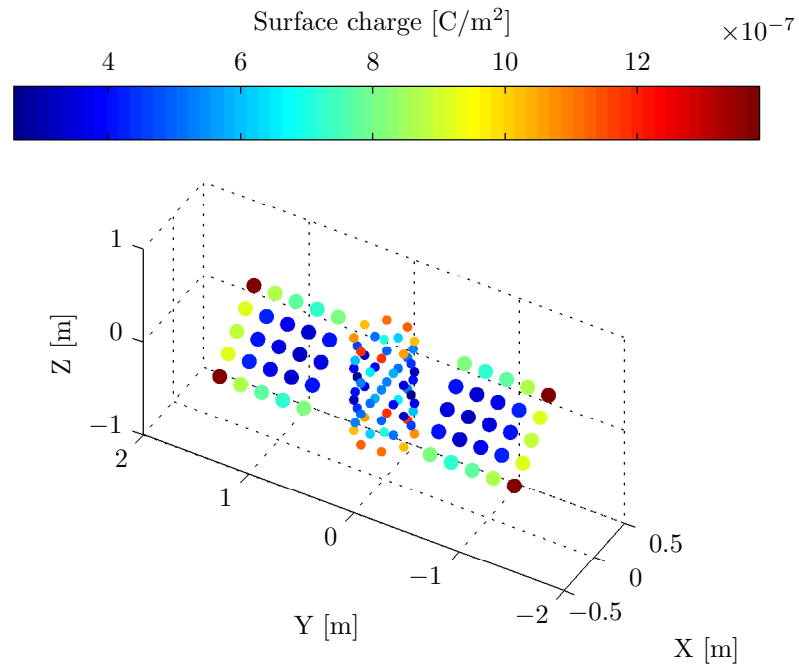


Figure 2.12: MSM model of a simple satellite

## 2.8 Constant Charge Modifications

So far, the capability of the Multi-Sphere Method (MSM) has been limited to modeling only objects of conducting material. While spacecraft considered for electrostatic de-spin operations should be dominantly conducting, a variety of insulating materials is commonly used for spacecraft construction. Moreover, augmenting the MSM to model materials of various conductivity extends its application to several other scenarios. Within conductors, charge carriers move around with

nearly no resistance so that the charge distribution is always considered to be in equilibrium. For insulators, the time scales for charges to redistribute are so large that the time dependency can also be ignored. A look at the first principals of electrodynamics allows for quantification of these time scales.

Since Coulomb charge is a conserved quantity, the following differential form of the general continuity equation holds according to the divergence theorem:

$$\frac{\partial \rho}{\partial t} + \nabla \cdot \mathbf{j} = 0 \quad (2.22)$$

where  $\rho$  is the volume charge density and  $\mathbf{j}$  represents the charge flux, also known as the electric current density. The current density is generally assumed to be proportional to the electric field  $\mathbf{E}$  by the factor  $\sigma$ , which is the electrical conductivity of the material.

$$\mathbf{j} = \sigma \mathbf{E} \quad (2.23)$$

Combining Eq. 2.22 and 2.23 yields

$$\frac{\partial \rho}{\partial t} = -\sigma \nabla \cdot \mathbf{E} \quad (2.24)$$

By Gauss' law, this becomes

$$\frac{\partial \rho}{\partial t} = -\frac{\sigma}{\epsilon_0} \rho \quad (2.25)$$

which suggests that a charge accumulation will disperse throughout a medium with an exponential time constant

$$\tau = \frac{\epsilon_0}{\sigma} \quad (2.26)$$

Most metals have conductivity values ranging from  $10^6$  to  $10^8$  S/m, which equates to time constants between  $10^{-17}$  and  $10^{-19}$  s. Electrically insulating materials such as plastics tend to have conductivity  $\sigma < 10^{-14}$  S/m resulting in charge mobility constants  $\tau > 10^3$  s.<sup>77</sup> For both these materials, the charge distribution can be assumed constant for a certain geometry configuration. For conductors, it is a function of the electric potential and geometry, while charge remains on insulators regardless of external influences. For materials with conductivity values within these

bounds, a time dependency exists for the charge density, which is outside the capability of the MSM and outside the scope of this research effort. Various semiconductors, glasses, and liquids fall in this category, which are not found in large quantities on most spacecraft.

### 2.8.1 Insulators

Assuming the system consists only of conductors and insulators, the Multi-Sphere Method (MSM) can be modified to include constant charge materials. For spheres within the insulator, a charge is specified rather than a voltage, which are compiled in the vector  $\mathbf{q}_I$ . Combining the mutual capacitance relationship in Eq. 2.3 for each of the conducting spheres yields

$$\phi_C = k_c[C_C]^{-1}\mathbf{q}_C + k_c[C_{C,I}]^{-1}\mathbf{q}_I \quad (2.27)$$

where  $[C_{C,I}]^{-1}$  is the mutual capacitance matrix populated with separation distances between the conducting spheres and insulated spheres, with no self capacitance terms. This relationship can be solved for  $\mathbf{q}_C$  so that the charge on all spheres in the system is known, at which point Eq. 2.8 and 2.9 can be equated to determine the force and torque on all bodies in the system. If knowledge of the resulting voltage on the insulating components is desired, it can be determined by:

$$\phi_I = k_c[C_I]^{-1}\mathbf{q}_I + k_c[C_{I,C}]^{-1}\mathbf{q}_C \quad (2.28)$$

where  $[C_I]^{-1}$  is populated with sphere sizes and relative distances between the insulator spheres, and  $[C_{I,C}]^{-1}$  is the transpose of  $[C_{C,I}]^{-1}$ .

### 2.8.2 Floating Charge

Another scenario that requires augmentation to the MSM is the case of an object modeled by multiple spheres that contains a total floating charge. The first iteration of the experimental testbed discussed in Chapter 5 presented such a situation. Since no active charging was possible on the rotating cylinder, its potential was brought to a certain level before the control experiment, at which point the connection with the power supply was removed. A certain amount of charge is

then left within the conducting body, but the charge distribution and potential level is determined by its orientation and the influence from other charged objects in the system.

Assuming the three sphere model discussed above is used to model the cylinder (spheres a-c in body 2), the charge on all the spheres sums to a total known charge  $q_2$  determined by the system configuration when the charge lead is removed:

$$q_2 = q_a + q_b + q_c \quad (2.29)$$

Now  $\phi_2$  is an extra unknown, dependent on  $\phi_1$  and the relative position and orientation of the two conductors. However, there is also an extra linear equation in Eq. (2.29). The matrix equation from Eq. 2.4 and 2.5 is elegantly modified as follows to isolate all the unknowns into a single column vector:

$$\begin{bmatrix} \phi_1/k_c \\ 0 \\ 0 \\ 0 \\ q_2 \end{bmatrix} = \begin{bmatrix} 1/R_1 & 1/r_{1,a} & 1/r_{1,b} & 1/r_{1,c} & 0 \\ 1/r_{1,a} & 1/R_a & 1/r_{a,b} & 1/r_{a,c} & -1 \\ 1/r_{1,b} & 1/r_{a,b} & 1/R_b & 1/r_{b,c} & -1 \\ 1/r_{1,c} & 1/r_{a,c} & 1/r_{b,c} & 1/R_c & -1 \\ 0 & 1 & 1 & 1 & 0 \end{bmatrix} \begin{bmatrix} q_1 \\ q_a \\ q_b \\ q_c \\ \phi_2/k_c \end{bmatrix} \quad (2.30)$$

It is necessary to incorporate the factor  $k_c$  with the electric potential terms prior to this modification to ensure that the matrix to be inverted remains well-conditioned. This approach can be extended for any system where a conductor contains a floating charge rather than being held at a specific voltage.

## 2.9 ISS Charged Droplet Experiment

Besides its intended use for modeling remote satellite de-spin dynamics, the MSM can be applied to a wide range of systems whose the kinematics are influenced by electrostatic interaction. With the modifications outlined in the previous section, charged insulators can be considered along with conductors. If the MSM is included within a structural dynamics framework, charged flexible membranes such as Gossamer structures can even be modeled.<sup>88</sup>



Recently, astronaut Don Pettit performed a collection of educational science experiments on the International Space Station (ISS), by the name Science Off the Sphere. In one interesting experiment, he creates Coulomb orbital motion with water droplets about a knitting needle, as can be seen in Figure 2.13. The triboelectric effect is used to charge the teflon knitting needle to negative voltages, while the water droplets are introduced with a syringe next to a positively charged nylon needle. The water droplets exhibit some very interesting chaotic motion about the knitting needle, which can not be readily predicted analytically.



Figure 2.13: Orbital motion of water droplets on the ISS by Coulomb interaction

The MSM, however, is the perfect tool to simulate the Coulomb orbital motion of these droplets. The knitting needle is modeled by a row of spheres. Since Teflon is an insulator, the constant charge formulation of the MSM from Section 2.8.1 is used. It is assumed that a constant charge is deposited along the length of the needle so that the average voltage along the surface is -10 kV. The water droplet is assumed to have a constant charge equivalent to +1 kV in an isolated environment. An initial position and velocity is chosen to match those in the Pettit's video, and the motion is integrated with an RK-45 integrator in MATLAB, where the electrostatic dynamics are calculated using the MSM. The resulting motion, shown in Figure 2.14 closely matches those experienced by the droplets in the video, although further comparison is difficult because only a single view is available of the physical experiment.

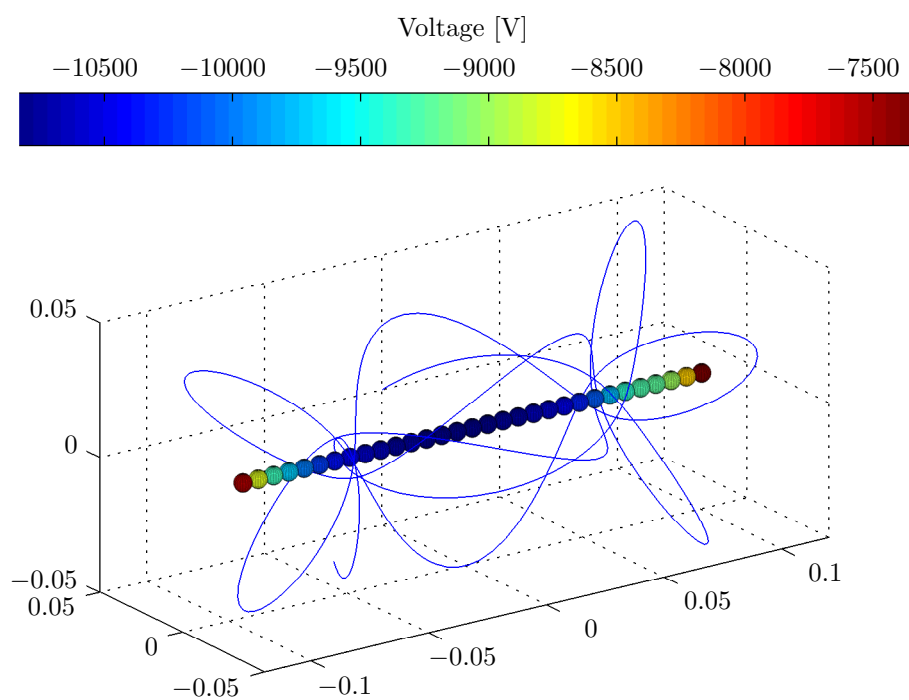


Figure 2.14: Simulation of Coulomb orbits modeled by the MSM

## Chapter 3

### Electrostatic De-spin

#### 3.1 System Dynamics

Before considering the full three dimensional Coulomb attitude control problem for a complex spacecraft body, it is necessary to develop the mathematical framework using a simplified scenario. Figure 3.1 shows the cylinder-sphere system that will be analyzed in detail throughout this chapter. Body 2 represents a rotating debris object with cylindrical geometry such as a Centaur upper stage rocket. Assuming the body of length  $h$  and radius  $r$  has a uniform density with mass  $m_2$ , its transverse moment of inertia is given by:

$$I_2 = \frac{1}{12}m_2(3r^2 + h^2) \quad (3.1)$$

The servicing spacecraft is modeled to be a spherical conductor of mass  $m_1$  with a center to center separation distance  $d$  from the debris, whose angular deviation from the parallel configuration is given by  $\theta$ . Angular motion of the cylinder is limited to 1-D rotation about its major axis of inertia, which represents the minimum kinetic energy case that an uncontrolled space object is likely to acquire.<sup>71</sup> Both bodies are free to translate as if the system is located in deep space. It is assumed that the control craft is capable of enforcing the desired electrostatic potential  $\phi_1$  and  $\phi_2$  on the two bodies. The specifications and power requirements of the charge transfer devices necessary to achieve those voltages are discussed in Chapter 4.

The free body diagram in Figure 3.1 shows the electrostatic forces and torques that result when potential levels of opposite polarity are applied to the two craft. Because the electrostatic

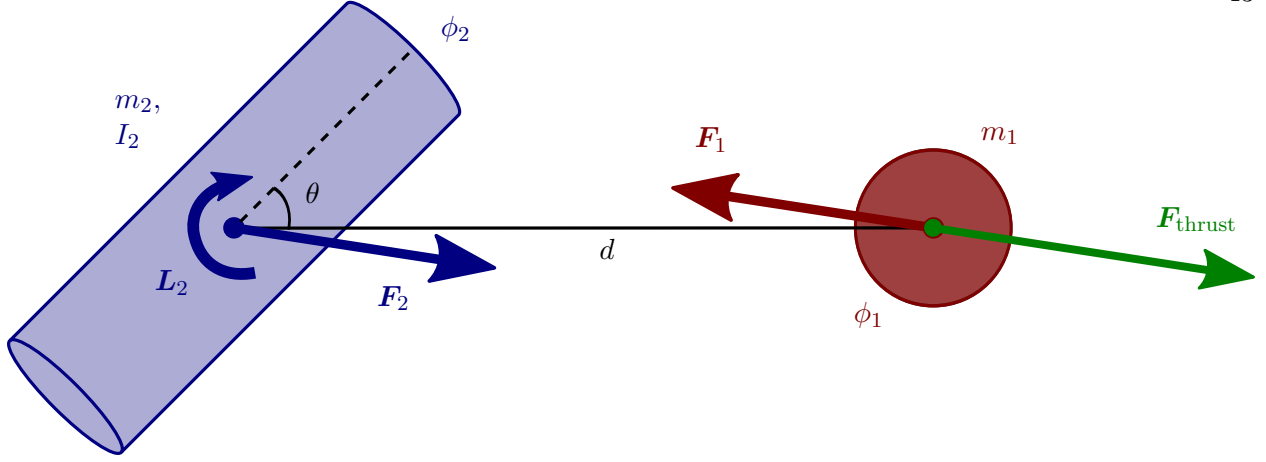


Figure 3.1: Free body diagram for cylinder-sphere system

force is conservative and internal to the system, the two craft experience equal and opposite net Coulomb forces  $F_1 = -F_2$ . Since the charge distribution on the nearby end of the cylinder causes a greater differential attractive force than that from the far end, the forces are offset and the cylinder experiences a control torque  $L_2$  which can be utilized to arrest its rotation. The total translational and rotational momentum in the system due to electrostatic interactions is conserved, but the vehicles approach each other in free space. A thrusting force on body 1 is necessary to maintain a constant relative position within the system:

$$\mathbf{F}_{\text{thrust}} = -\mathbf{F}_1 \left(1 + \frac{m_1}{m_2}\right) \quad (3.2)$$

In the end, it is this force that provides the energy necessary to adjust the attitude of the cylinder. If the appropriate control strategy is implemented, the system will continually move in space, but the craft are fixed relative to each other and can be assumed stationary for the following control development. When the system employs equal polarity potential levels, the forces and torques are reversed and the vehicles are electrostatically repelled.

For a body with inertia matrix  $[I]$  and angular velocity vector  $\boldsymbol{\omega}$  rotating freely in space, the rotational equations of motion are

$$[I]\dot{\boldsymbol{\omega}} = -\boldsymbol{\omega} \times [I]\boldsymbol{\omega} + \mathbf{L} \quad (3.3)$$

With the cylinder constrained to one dimensional motion in the plane of the control craft, the dynamics reduce to

$$I_2\ddot{\theta} = L_2 \quad (3.4)$$

In order to gain insight into the system dynamics and develop robust attitude control algorithms, further knowledge of the electrostatic torque  $L_2$  is desired. The Multi-Sphere Method requires inverting the Position Dependent Capacitance matrix, followed by a summation of the Coulomb force due to the charge on each sphere in the model. Even using the simplest three sphere MSM model developed in Section 2.3, analytic expressions of the torque are incredibly complex. However, if some simplifying assumptions are made regarding the potential levels, it becomes evident that dependency on the voltages and cylinder orientation are separable.

Without loss of generality, it is assumed that the voltage applied to the control sphere is  $\phi_1 = \phi$  and the voltage applied to the debris cylinder is  $\phi_2 = |\phi| \geq 0$ . As a result, negative  $\phi$  implies opposite polarity, attractive control while positive  $\phi$  implies equal polarity, repulsive control. When this condition is satisfied, the expression for the torque  $L_2$  can be separated into dependencies on the control voltage  $\phi$  and cylinder rotation angle  $\theta$ :

$$L_2 = \gamma f(\phi)g(\theta) \quad (3.5)$$

If the separation of potential  $\phi$  and orientation  $\theta$  can not be done, extracting the required control potential from the charged attitude feedback is significantly complicated. For the cylinder shape, this separation is justified by restricting the potentials to  $\phi_2 = |\phi_1|$  and assuming the cylinder is symmetric.

Fig. 3.2 shows the Coulomb torque  $L_2$  exerted on a 3 m by 1 m cylinder for various cylinder orientations  $\theta$  and applied potentials  $\phi$ . The separation distance from the 1 m diameter control craft is chosen to be  $d = 3$  m to highlight the asymmetry between opposite and equal polarity configurations due to induced charging effects. This data could be used as a lookup table to determine the necessary potentials for a desired torque, but for nonlinear stability analysis, a more analytic formulation is desired.

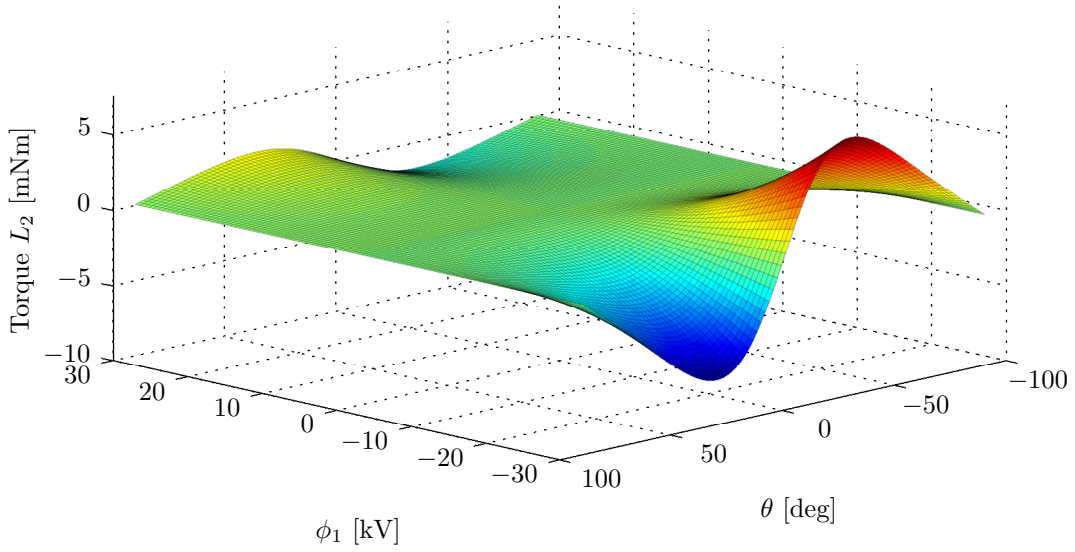


Figure 3.2: Coulomb torques for various orientations and potentials

For larger separation distances, where the torque is equal and opposite for positive and negative  $\phi$ , the Coulomb torque on the cylinder can be modeled with high accuracy using the analytic expression

$$f(\phi) = \phi|\phi| \quad (3.6)$$

and

$$g(\theta) = \sin 2\theta \quad (3.7)$$

From the asymmetry in Fig. 3.2, it is clear that the formulation above does not hold for smaller separation distances. Due to the proximity of the shapes and the resulting induced charging effect, the torques produced by the attractive configuration are considerably larger than those imparted by electrostatic repulsion. To capture this asymmetry, a polarity dependent coefficient  $\gamma(\text{sign}(\phi))$  is proposed, where  $\gamma$  remains always positive:

$$\gamma(\text{sign}(\phi)) = \begin{cases} \gamma_a & \text{for } \phi < 0 \\ \gamma_r & \text{for } \phi > 0 \end{cases} \quad (3.8)$$

Reference 6 explores alternative formulations of  $g(\theta)$  to capture the non-symmetric orientation dependency at small separation distances. A summation of higher order terms of the form  $\sin(2m\theta)$

is used, which are normalized with respect to the maximum torque angle. It turns out that this function is also polarity dependent, and the coefficients must change with attraction or repulsion much like  $\gamma$  does. Importantly, inclusion of the higher order terms does not affect the sign of  $g(\theta)$ , which remains positive in the first and third quadrants and negative in the second and fourth quadrants of  $\theta$ . Using the polarity dependent coefficient  $\gamma$  and function  $g$  as described above, we obtain

$$L_2 = \begin{cases} \gamma_a f(\phi) g_a(\theta) & \text{for } \phi < 0 \\ \gamma_r f(\phi) g_r(\theta) & \text{for } \phi > 0 \end{cases} \quad (3.9)$$

where the  $f$  function remains  $f(\phi) = \phi|\phi|$  and is readily invertible to obtain the required electrostatic potentials for a desired  $f$ .

## 3.2 Non-linear Control Theory

### 3.2.1 Equilibrium Configurations

For the following developments, it is assumed that the relations in Eq. 3.6 & 3.7 hold. The constant  $\gamma$  is positive for a prolate geometry such as the cylinder. The one-dimensional rotational equation of motion that results is

$$I\ddot{\theta} - \gamma f(\phi) g(\theta) = 0 \quad (3.10)$$

To evaluate the equilibrium orientations and study the associate local stability, let  $\theta_{e,i}$  be the set of orientation angles such that  $g(\theta_{e,i}) = 0$ . These orientations, as shown in Figure 3.3, occur every  $90^\circ$  at the parallel and perpendicular orientations. Let a small departure angle  $\Delta\theta$  be defined as

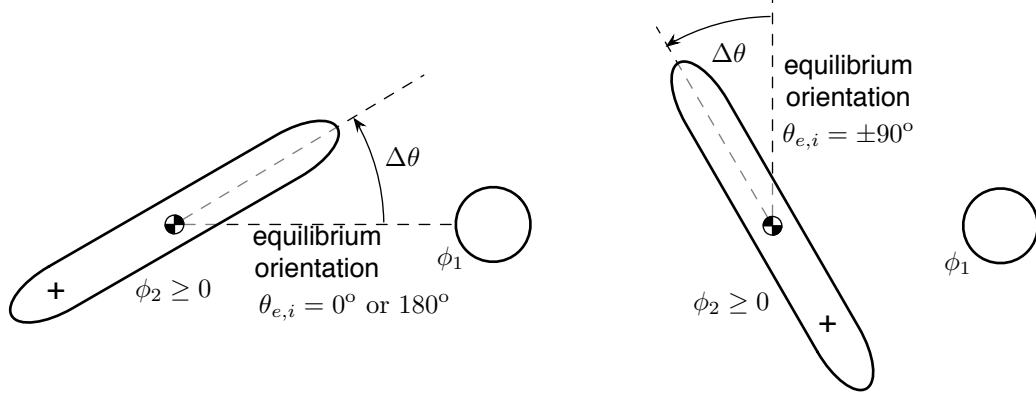
$$\Delta\theta = \theta - \theta_{e,i} \quad (3.11)$$

then the linearized rotational equation of motion about an equilibrium orientation  $\theta_{e,i}$  is given by

$$I\Delta\ddot{\theta} + k\Delta\theta = 0 \quad (3.12)$$

where the local stiffness  $k$  is defined as:

$$k = -\gamma f(\phi) \left. \frac{\partial g}{\partial \theta} \right|_{\theta=\theta_{e,i}} \quad (3.13)$$



(a) In-line equilibrium configuration

(b) Cross-track equilibrium configuration

Figure 3.3: Illustration of departure angle with respect to equilibrium orientations

The sensitivity of  $g$  with respect to  $\theta$  is

$$\frac{\partial g}{\partial \theta} = 2 \cos(2\theta) \quad (3.14)$$

To study the local stability of departure motions about equilibrium orientations, the sign of  $k$  is investigated for different scenarios. Consider first the in-line debris orientation shown in Figure 3.3(a) with  $\theta_{e,i} = 0^\circ$  or  $180^\circ$ . The local stiffness  $k$  in this case is

$$k = -2\gamma f(\phi) \quad (3.15)$$

For a repulsive force setup with  $\phi > 0$  and  $f(\phi) = \phi|\phi| > 0$ , a negative stiffness  $k < 0$  results, indicating an unstable equilibrium. This instability can be understood because the near-end of the cylinder experiences a stronger repulsion force than the far end, and thus the resulting electrostatic torque will cause a destabilizing effect. If the sphere potential is negative with  $\phi < 0$ , the attractive electrostatic force causes a locally stable equilibrium with  $k > 0$ .

Next, consider the equilibria shown in Figure 3.3(b) where the cylinder tall axis is orthogonal to the line-of-sight axis. Here the  $g$  sensitivity is

$$\left. \frac{\partial g}{\partial \theta} \right|_{\theta=\pm 90^\circ} = 2 \cos(\pm 180^\circ) = -2 \quad (3.16)$$



Assuming a repulsive force configuration with  $f(\phi) > 0$ , the local stiffness is

$$k = 2\gamma f(\phi) > 0 \quad (3.17)$$

Thus, if bodies 1 and 2 are electrostatically pushing on each other, then  $\theta_{e,i} = \pm 90^\circ$  are locally stable orientations. Finally, assuming the cross-track scenario in Figure 3.3(b) and a pulling configuration with  $f(\phi) < 0$ , the local stiffness is

$$k = 2\gamma f(\phi) < 0 \quad (3.18)$$

indicating that such an orientation is locally unstable.

### 3.2.2 Rate Control With Zero Nominal Potential

For the following developments, the function  $f$  in Eq. 3.5 must be invertible, which is satisfied by the relation in Eq. 3.6. First, the scenario is investigated where the nominal spacecraft potential is zero. Thus, when the tumbling motion has been arrested, no electrostatic pulling or tugging should be present. The inertial thrust to maintain a fixed separation distance will also go to zero as the tumbling ceases. The control development assumes that the tumbling angle  $\theta$  and rate  $\dot{\theta}$  are measured and that the potential  $\phi$  is the control variable.

Let  $\alpha > 0$  be a constant rate feedback gain. The function  $h$  is chosen such that

$$h(x)x > 0 \quad \text{if } x \neq 0 \quad (3.19)$$

forms a positive definite expression. Then, the following tumble rate feedback control  $f(\phi)$  is proposed:

$$f(\phi) = -\text{sgn}(g(\theta))h(\alpha\dot{\theta}) \quad (3.20)$$

Because the function  $f$  is invertible, it is possible to determine from Eq. (3.20) the required potential  $\phi_1 = \phi$  and  $\phi_2 = |\phi|$  on both bodies. Note that if the approximate electrostatic torque did not have the separation of potential and relative orientation, as formulated in Eq. (3.5), then the potential feedback control development becomes significantly more complex. In particular, due to the coupling between orientation and potential, it may not be possible to extract the control

potential  $\phi$  analytically, in which case numerical solvers are required to determine the control. As is, the potential control development only requires  $f$  and  $g$  to satisfy some simple conditions to guarantee stability. In particular, the  $g(\theta)$  function approximation could be further refined, without having to develop a new rate feedback control strategy.

The function  $h$  is introduced to yield a general feedback control whose performance can be modified. For example, the simple linear function  $h(\alpha\dot{\theta}) = \alpha\dot{\theta}$  can be used. However, the resulting control potentials will grow large if large initial tumble rates  $\dot{\theta}$  are considered. If the available potentials are bounded to be less than  $\phi_{\max}$ , then the following  $h$  function will smoothly limit or saturate the control without impacting the following stability discussion:

$$h(\alpha\dot{\theta}) = f(\phi_{\max}) \frac{\tan^{-1}(\alpha\dot{\theta})}{\pi/2} \quad (3.21)$$

As the tumble rate  $\dot{\theta} \rightarrow \infty$ ,  $\tan^{-1}(\alpha\dot{\theta}) \rightarrow \pi/2$ , and

$$\lim_{\dot{\theta} \rightarrow \infty} h(\alpha\dot{\theta}) = f(\phi_{\max}) \quad (3.22)$$

Thus, the control effort for large rates  $\dot{\theta}$  is smoothly limited with this  $h$  function in Eq. (3.21) by

$$\lim_{\dot{\theta} \rightarrow \infty} f(\phi) = \begin{cases} f(\phi_{\max}) & \text{if } g(\theta) \neq 0 \\ 0 & \text{if } g(\theta) = 0 \end{cases} \quad (3.23)$$

To investigate the stability of the feedback control law in Eq. (3.20), the rotational kinetic energy is used as a globally positive definite Lyapunov candidate function  $V(\dot{\theta})$ .<sup>71</sup>

$$V(\dot{\theta}) = \frac{I}{2} \dot{\theta}^2 \quad (3.24)$$

The presented control only aims to arrest the spin rate, and does not seek to achieve a particular relative orientation angle  $\theta$ . Taking the time derivative of  $V$ , and substituting the equations of motion in Eq. (3.10) leads to

$$\dot{V}(\dot{\theta}) = L_2 \dot{\theta} = \gamma f(\phi) g(\theta) \dot{\theta} \quad (3.25)$$

Substituting in the control expression in Eq. (3.20) and simplifying leads to

$$\dot{V}(\dot{\theta}) = -\gamma |g(\theta)| h(\alpha\dot{\theta}) \dot{\theta} \leq 0 \quad (3.26)$$

This  $\dot{V}$  expression is globally negative semi-definite as  $h(\alpha\dot{\theta})\dot{\theta}$  is a positive definite expression and  $\gamma > 0$ . Note that  $\dot{V}$  can become zero at the equilibrium orientations  $\theta_{e_i}$  where  $g(\theta_{e,i}) = 0$ . Thus, Eq. (3.26) guarantees globally stable closed loop dynamics with regard to tumbling rate.

To study convergence, LaSalle's invariance principle is employed.<sup>40</sup> The Lyapunov rate  $\dot{V}$  is zero if either the rate  $\dot{\theta}$  is zero and the control goal is achieved, or if  $g(\theta) = 0$ . The latter condition forces  $\dot{V}$  to zero regardless if  $\dot{\theta}$  is zero. Since all but four equilibrium orientations result in  $g(\theta) \neq 0$ , it is not possible for the condition  $g(\theta) = 0$  to remain true unless  $\dot{\theta} = 0$  as well. Thus, the largest invariant set where  $\dot{V}$  vanishes is  $(\theta, \dot{\theta}) = \{\dot{\theta} = 0\}$ . As a result, this potential feedback control achieves global convergence in driving the rates to zero. The final orientation, however, is arbitrary with this control.

### 3.2.3 Rate Control with Nominal Electrostatic Tugging or Pushing

Electrostatic forces have been proposed to reorbit large geosynchronous debris objects to disposal orbits.<sup>29,31,72</sup> Because the large, bus-sized GEO debris can be tumbling at 10s of degrees per second, not having to mechanically touch the debris is a significant advantage. While the pulling configuration with a nominal attractive electrostatic force is the preferred configuration,<sup>69</sup> pushing configurations are also feasible. The rate-control from the previous section is modified such that the nominal potential  $\phi$  is non-zero, allowing for continuous pulling ( $\phi < 0$ ) or pushing ( $\phi > 0$ ).

To investigate detumbling a rigid body while also electrostatically pulling or pushing the object, the following Lyapunov candidate function is considered:

$$V(\theta, \dot{\theta}) = \frac{I}{2}\dot{\theta}^2 + \gamma\beta \int_0^{\theta_r} g(x)dx \quad (3.27)$$

where  $\beta$  represents a feedforward constant. The integral term of this  $V$  expression is locally positive definite if a reference orientation  $\theta = 0$  is chosen such that

$$\left. \frac{\partial g(\theta)}{\partial \theta} \right|_{\theta=0} > 0 \quad (3.28)$$

This condition has an impact on the final convergence of the rate control. Note that this Lyapunov function depends on the orientation  $\theta$  as well as the rate  $\dot{\theta}$  because the pushing/pulling condition impacts the final orientation of the debris body.

Taking the time derivative of Eq. (3.27), and substituting Eqs. (3.5) and (3.10), yields the following Lyapunov rate expression:

$$\dot{V}(\theta, \dot{\theta}) = (\gamma f(\phi)g(\theta) + \gamma\beta g(\theta))\dot{\theta} \quad (3.29)$$

Let the new potential control expression be:

$$f(\phi) = -\beta - \text{sgn}(g(\theta))h(\alpha\dot{\theta}) \quad (3.30)$$

Given a nominal potential  $\phi_{\text{nom}}$ , the feedforward gain  $\beta$  is chosen to be

$$\beta = f(\phi_{\text{nom}}) \quad (3.31)$$

resulting in the appropriate nominal control effort.

Substituting Eq. (3.30) into Eq. (3.29) yields the following Lyapunov rate expression:

$$\dot{V} = \left( -\gamma\beta g(\theta) - \gamma\text{sgn}(g(\theta))h(\alpha\dot{\theta})g(\theta) + \gamma\beta g(\theta) \right) \dot{\theta} \quad (3.32)$$

$$= -\gamma|g(\theta)|h(\alpha\dot{\theta})\dot{\theta} \leq 0 \quad (3.33)$$

Note that the integral term in the Lyapunov expression causes a cancellation with the feedforward potential term, resulting in a negative semi-definite  $\dot{V}$  expression. The feedforward/feedback control in Eq. (3.30) is thus at least locally stable. Considering  $V$  depends on both  $\theta$  and  $\dot{\theta}$ , this implies that the system is stable when it comes to rest at the equilibrium orientations, as depicted in Figure 3.4.

Next, the convergence of this feedback/feedforward control is investigated. As before,  $\dot{V}$  vanishes if either  $\dot{\theta} = 0$  or  $g(\theta) = 0$ . The earlier control resulted in  $\dot{\theta} \rightarrow 0$  for all cases, but the final orientation was arbitrary depending on the initial conditions. With the feedforward component included, the attitude will converge to discrete orientations. The closed loop dynamics using the

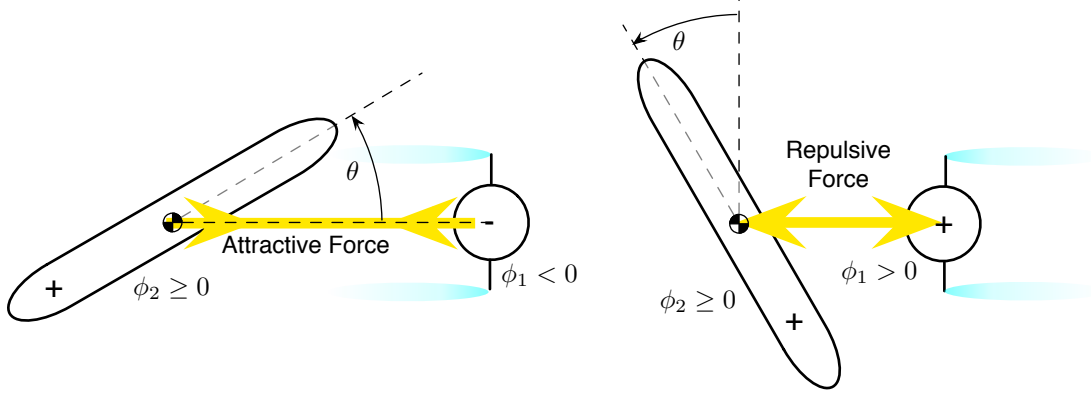
(a) Pulling configuration with  $\beta < 0$ (b) Pushing configuration with  $\beta > 0$ 

Figure 3.4: Illustration of pulling and pushing configurations.

control in Eq. (3.30) is

$$I\ddot{\theta} + \gamma\beta g(\theta) + \gamma|g(\theta)|h(\alpha\dot{\theta}) = 0 \quad (3.34)$$

Again, it is not possible for  $g(\theta) = 0$  to remain true if  $\dot{\theta} \neq 0$ . However, can  $g(\theta)$  remain non-zero if  $\dot{\theta}$  is zero, i.e. can the cylinder come to rest at one of the non-equilibrium orientations? Setting the rate to zero in Eq. (3.34) yields

$$I\ddot{\theta} = -\gamma\beta g(\theta) \quad (3.35)$$

This indicates that  $\ddot{\theta}$  cannot remain zero unless both  $\dot{\theta} = 0$  and  $g(\theta) = 0$ . Thus, the largest invariant set where  $\dot{V}$  vanishes is  $\theta = \theta_{e,i}$  and  $\dot{\theta} = 0$ . In contrast to the rate-only feedback, this feedforward/feedback control has the rate converge to zero, and the orientation converge to a torque equilibrium orientation. For the torque shape function  $g(\theta) = \sin(2\theta)$  two of these equilibria were unstable, and two were stable. If small perturbations are considered, the second body will not remain at an unstable equilibrium, but eventually converges to a stable equilibrium.

To study this stability behavior, consider the Lyapunov surface illustration in Figure 3.5 where unit inertia and unit feedforward gain are used with the tugging configuration where  $\beta < 0$  and  $g(\theta) = \sin(2\theta)$ . The largest Lyapunov level about the origin is highlighted for convenience. For initial conditions outside this level set, it is possible for the debris body to stabilize about the

stable equilibrium  $\theta_e = 180^\circ$ . This illustrates that the control in Eq. (3.30) is indeed only locally stable. However, if the control objective is to arrest the rate and align the body with either  $\theta = 0^\circ$  or  $180^\circ$ , then the control is globally asymptotically stabilizing, although it is arbitrary which of the two orientations the system will converge to.

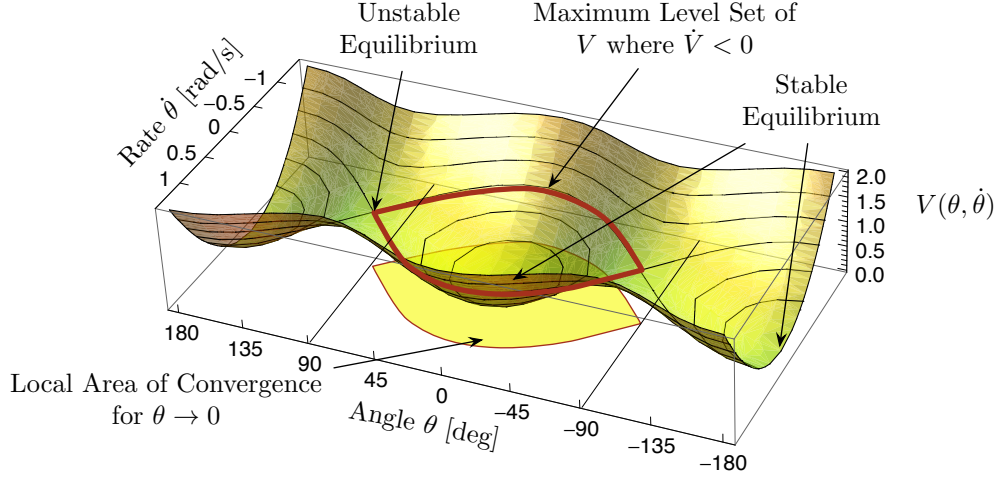


Figure 3.5: Illustration of Lyapunov function and level sets for unit inertia  $I_2$  and gain  $\beta$

The contour plot in Figure 3.6(a) illustrates the closed loop trajectories if the control in Eq. (3.30) is active. Depending on the initial conditions, the trajectories can either converge to the stable equilibria at 0 or 180 degrees, or approach the  $\pm 90$  degree unstable equilibria. If it is important that the tumbling body settle with a particular end (either  $\theta = 0^\circ$  or  $180^\circ$ ), then the following strategy can be employed. Figure 3.6(b) illustrates the state trajectories if no control is present, and the debris body continues to tumble at a constant rate. The horizontal flow lines can be exploited to move the states of the tumbling body into a preferred zone where convergence to a particular equilibrium orientation is guaranteed. This process is highlighted in red in Figure 3.6(a). The rate control is first employed until the rates are small enough to guarantee convergence to an equilibrium. If this is not the desired equilibrium, turning off the potential control will allow the body to tumble onward. As the state trajectory enters the local area of convergence of the desired equilibrium orientation, the feedback control is re-engaged to arrest the final rates, and drive  $\theta \rightarrow \theta_e$ .

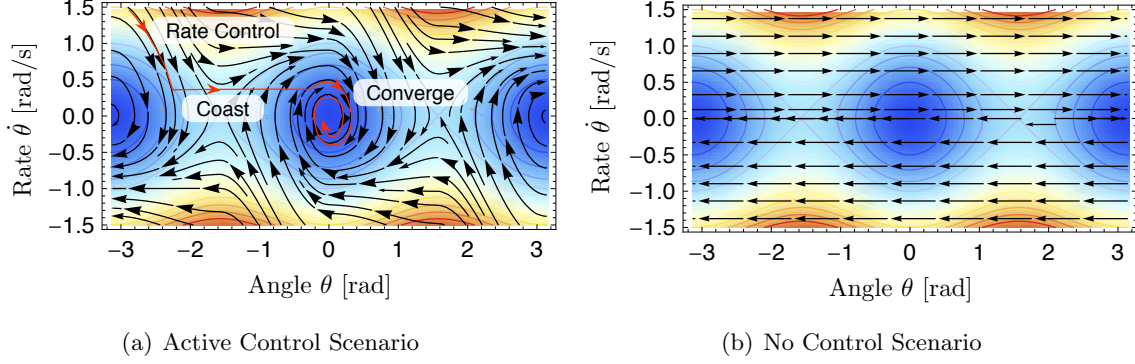


Figure 3.6: State Space Flow Illustration In Relation to Lyapunov Level Sets.

Further control developments to achieve a desired rate or attitude are discussed in the Chapter 5, in context of the experimental testbed.

### 3.3 Baseline Simulation

To verify the performance of the Coulomb attitude control laws developed above, they are executed within a simulation of the simplified cylinder-sphere system. The representative debris cylinder with a length of 3 m and diameter of 1 m is used, with a control craft of 1 m diameter. Assuming an average density of  $100 \text{ kg/m}^3$ , this results in a 235.6 kg debris object with a  $1,038.43 \text{ kg-m}^2$  transverse moment of inertia and a 52.4 kg control vehicle. A  $d = 7 \text{ m}$  separation is considered, which represents a surface to surface separation of 10 craft radii when the cylinder is oriented parallel and at closest approach. It is assumed that the debris object has an initial counter-clockwise rotation rate of  $\omega = \dot{\theta} = 2 \text{ rpm} = 12 \text{ deg/s}$ . These parameters are summarized in Table 3.1.

The de-spin operation is modeled from start to finish using a custom RK-45 integration scheme with a 0.1 second time step, executed in MATLAB. The three sphere MSM outlined in Section 2.3 is used to model the electrostatic interaction in the system. The charge distribution for a single configuration is shown in Figure 3.7. The debris' attitude is restricted to rotation about its minor geometrical axis, but both objects have full translational freedom. The thrust control in Eq. (3.2) is implemented along with a proportional derivative feedback on the desired relative

Table 3.1: Parameters for baseline cylinder de-spin simulation

Parameter	Value	Units	Description
$d$	7	m	Center-to-center separation
$\rho$	100	kg/m <sup>2</sup>	Object densities
$m_1$	52.4	kg	Sphere mass
$m_2$	235.6	kg	Cylinder mass
$I_2$	191.4	kg·m <sup>2</sup>	Cylinder transverse moment of inertia
$\omega_0$	12	deg/sec	Initial cylinder rotation rate
$\alpha$	$5 \times 10^5$	–	Gain in $h$ function
$\phi_{\max}$	30	kV	Max voltage in $h$ function
$P$	0.3	–	Position control proportional gain
$D$	0.6	–	Position control derivative gain

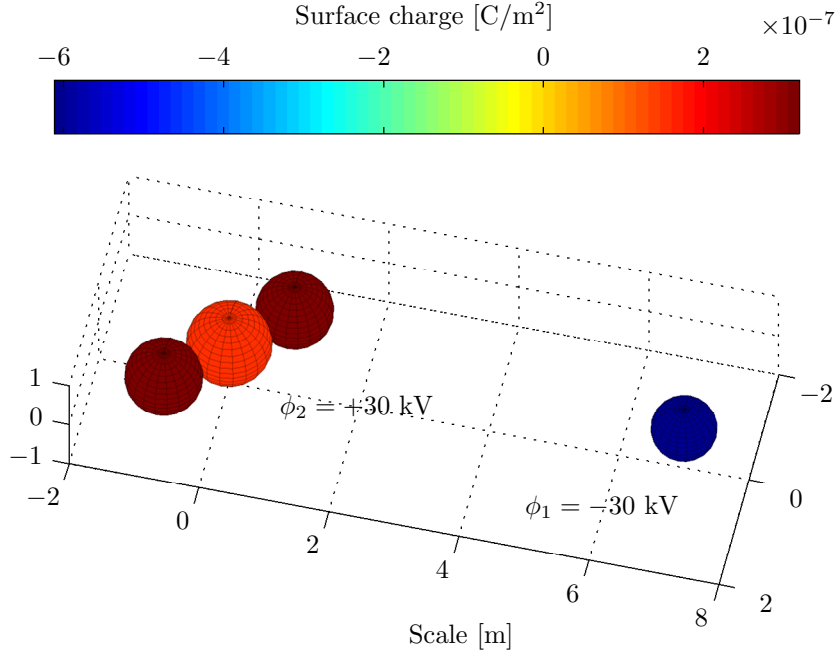


Figure 3.7: Three sphere MSM for cylinder-sphere system

position, as follows:

$$\mathbf{F}_{\text{thrust}} = m_1 \left( -\frac{\mathbf{F}_1}{m_1} + \frac{\mathbf{F}_2}{m_2} + P(\boldsymbol{\rho} - \boldsymbol{\rho}_{\text{des}}) + D(\dot{\boldsymbol{\rho}} - \dot{\boldsymbol{\rho}}_{\text{des}}) \right) \quad (3.36)$$

where  $\boldsymbol{\rho}$  represents the separation vector from the servicing craft to the debris object, with  $\rho_{\text{des}} = d$



and  $\dot{\rho}_{\text{des}} = 0$ . The attitude control algorithm in Eq. 3.20 from Section 3.2.2 is applied, with  $h$  defined by Eq. 3.21. The required voltages are determined as follows:

$$\phi_1 = \begin{cases} \sqrt{-f(\phi)} & \text{if } f(\phi) < 0 \\ -\sqrt{f(\phi)} & \text{if } f(\phi) > 0 \end{cases} \quad (3.37)$$

$$\phi_2 = |\phi_1| \quad (3.38)$$

Since a very large gain  $\alpha$  is chosen, this control essentially reduces to a maximum performance quadrant dependent polarity switching voltage control.

From Figure 3.8(a) and 3.8(b) it is clear that the cylinder stops spinning after roughly 75 hours or just over 3 days, during which time 4522 full rotations have been completed. A complete de-spin from 12 deg/s by electrostatic actuation in this time is impressive considering the momentum of the cylinder and separation distance between the craft. As to be expected with this form of rate control, the cylinder comes to rest at an arbitrary angle, at which point the voltage control drops to nil. Figure 3.8(d) shows that the entire system has been displaced roughly 35 km during the operation, even though no nominal voltage control was implemented. Because of the induced electrostatic effects and complex capacitance relationship between charge and voltage, there is a noticeable difference in performance between the pulling and pushing configurations in different quadrants. Namely, 62.4% of the arresting torque comes from the quadrants in which the debris object and control craft have opposite polarity (pulling configuration), while only 37.6% of the effort comes from the equal polarity (pushing) configuration. The resulting difference in forces accounts for the net system displacement. This displacement could be used to raise the orbit of a GEO debris satellite and benefit the eventual goal of placing the object into a disposal orbit. If the system displacement is not desired, the control craft could reposition itself to opposite sides of the rotating debris in order to achieve a net zero system displacement.

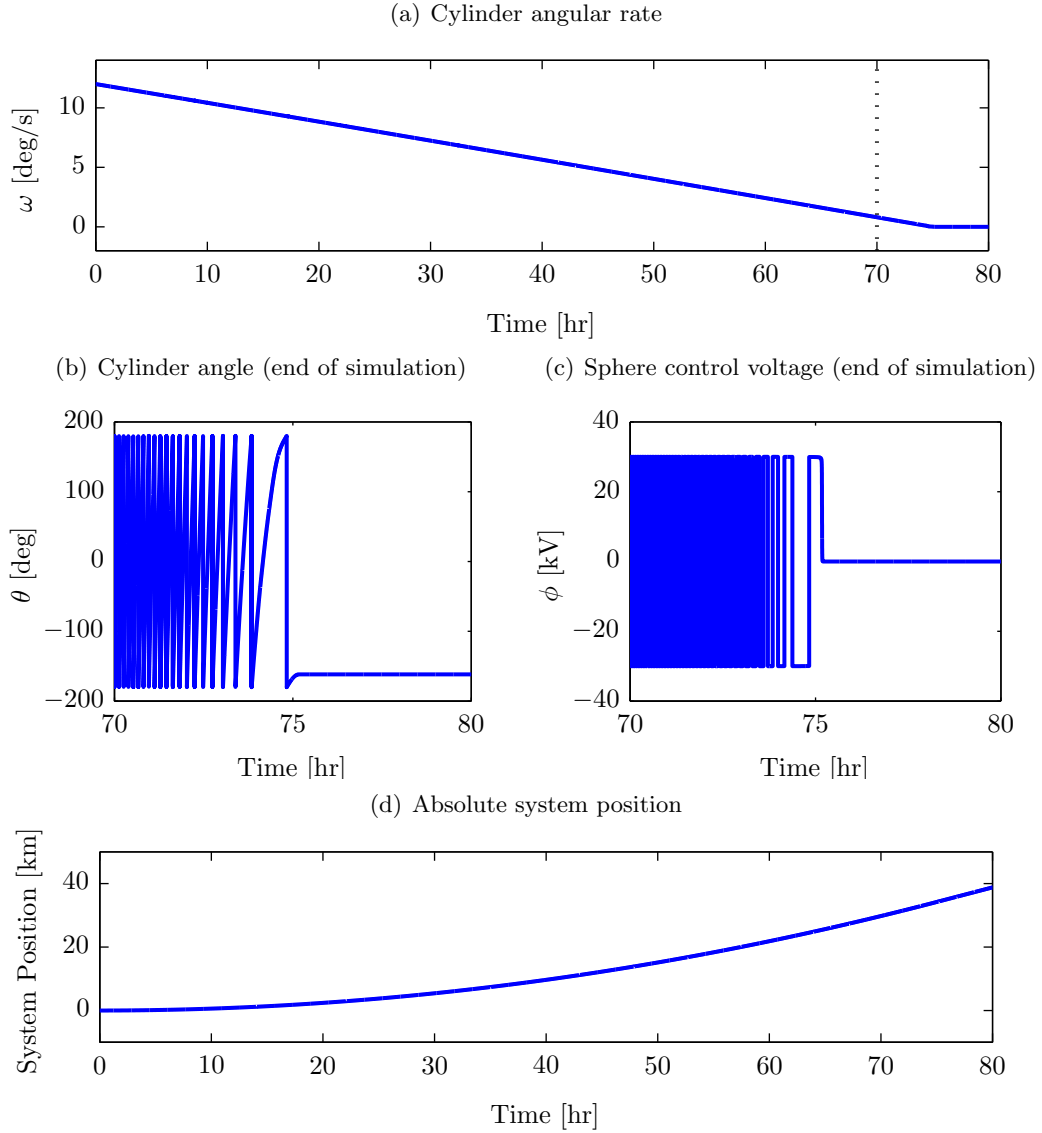


Figure 3.8: Cylinder tug and de-spin simulation using Coulomb charge control

### 3.4 System Parameter Optimization

#### 3.4.1 Single Rotation Simulation

The simulation in the previous section serves to prove the feasibility of the remote Coulomb de-spin concept and validate the voltage control algorithms developed for the servicing craft. So far the study has only considered a single system configuration. To optimize the design of future mission implementations, knowledge of the impact of various system parameters on the de-spin

performance is necessary. First, variations in separation distance as well as size and shape scaling of both spacecraft are studied to determine what effect they have on the system's de-spin time, displacement, and required stationkeeping maneuvers.

Instead of simulating the full mission de-spin operation with varying parameters, which would quickly become computationally prohibitive, a high fidelity simulation of a single cylinder rotation is conducted. Since only a single rotation is considered, the higher fidelity surface Multi-Sphere Model (SMSM) from Section 2.4 is used. Figure 3.9 shows the charge distribution existent in one orientation, with 50 evenly distributed conducting spheres along the surface of the debris cylinder and 13 spheres used to model the control craft. The charge control algorithm is simplified so that  $\phi_1 = -30$  kV and  $\phi_2 = +30$  kV when  $0^\circ < \theta < 90^\circ$ , while  $\phi_1 = \phi_2 = +30$  kV when  $90^\circ < \theta < 180^\circ$ , ensuring constantly arresting torques. This mimics the more complicated control law from Section 3.2.2 very well for large  $\alpha$  and considerable rotation rates.

As the cylinder completes its rotation, the electrostatic forces and torques are tracked. The

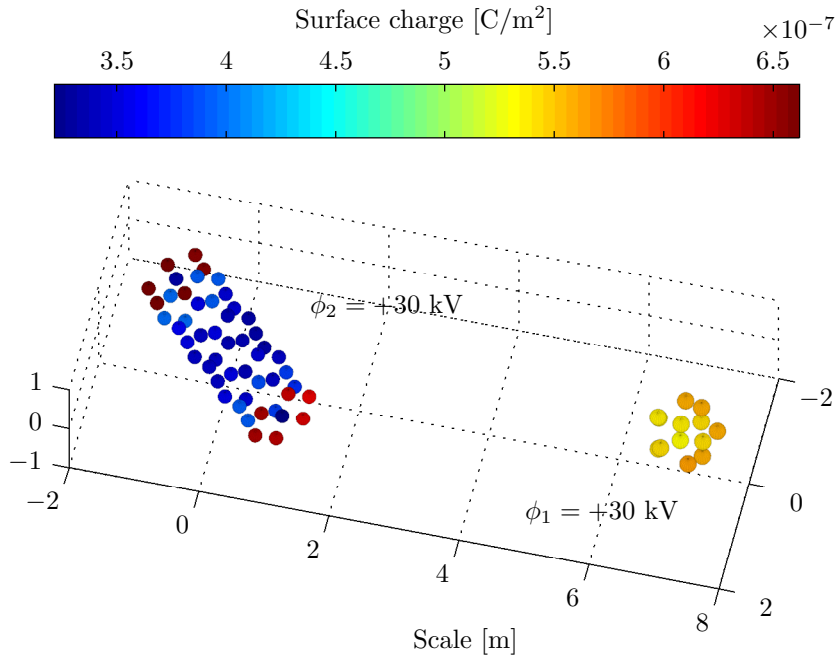


Figure 3.9: Surface populated MSM for cylinder-sphere system

average torque  $L_{2,\text{ave}}$ , which is independent of rotation rate, is used to calculate the de-spin time

$$\Delta t = \frac{I_2 \Delta \omega}{L_{2,\text{ave}}} \quad (3.39)$$

Assuming the thrust profile from Eq. 3.2 is implemented to maintain a constant separation distance between the objects in space, the entire system will accelerate by

$$\mathbf{a}_{\text{sys}} = \frac{\mathbf{F}_2}{m_2} \quad (3.40)$$

Given the de-spin time, the total system displacement in deep space can be calculated

$$\Delta \mathbf{X} = \frac{1}{2} \mathbf{a}_{\text{sys,ave}} \Delta t^2 = \frac{1}{2} \left( \frac{\mathbf{F}_{2,\text{ave}}}{m_2} \right) \Delta t^2 \quad (3.41)$$

The results for the single rotation simulation can be seen in the bottom line of Table 3.2, as compared to the full temporal and spatial simulation from the previous section. Clearly, the Coulomb torques and the total de-spin time agree to within a fraction of a percent with the time dependent simulation. The Coulomb force results agree to within 2.7% while system displacements deviate by about a kilometer, which likely results from the discrete position feedback control algorithm used above. An average thrust magnitude of 1.30 mN is required to maintain the relative position in the system. If an ion thruster with  $I_{SP} = 3000$  s is utilized, this results in only 11.9 g of propellant expelled over the duration of the de-spin operation.

Table 3.2: Baseline de-spin results

	$F_{2,\text{ave}}$ [mN]	$L_{2,\text{ave}}$ [mNm]	$\Delta t$ [hrs]	$\Delta X$ [km]
Time Dependent Simulation	0.225	0.150	75.17	34.37
Single Rotation Average	0.219	0.150	74.43	33.37

### 3.4.2 Separation Distance

It is important to understand the effect of separation distance on de-spin performance to determine what collision risks are warranted when conducting a remote electrostatic de-spin mission. Logically, the average force and torque experienced by the debris object decrease when the servicing

craft is situated farther away. When varying the separation distance in the single rotation simulation discussed above, it is possible to fit the following functions with high correlation to the averaged Coulomb force and torque acting on the debris cylinder:

$$F_{2,\text{ave}} \approx 0.2136 d^{-3.573}, \quad R^2 = 0.9974 \quad (3.42)$$

$$L_{2,\text{ave}} \approx 0.1076 d^{-3.407}, \quad R^2 = 0.9985 \quad (3.43)$$

Since the time to remove a given rotation rate varies inversely with the average Coulomb torque, and combining Eqs. (3.39) and (3.41) yields

$$\Delta X = \frac{1}{2} \left( \frac{I_2^2 \Delta \omega^2}{m_2} \right) \left( \frac{F_{2,\text{ave}}}{L_{2,\text{ave}}^2} \right) \quad (3.44)$$

both the de-spin time and system displacement increase by a high power with the separation distance. As such, as close as possible a formation is desirable for the de-spin operations, while successfully mitigating collision risks.

### 3.4.3 System Scale

Next, consider what happens when the entire system scales up or down in size, while the relative object sizes and separation distance stay constant. This exercise proves useful when considering the downsized terrestrial experiments conducted in Chapter 5, hereby relating the results to the full scale mission design. While the capacitance of each object increases with increasing size, resulting in higher charge levels for a given voltage, the increased separation distance reduces the electrostatic effects. Interestingly, the Coulomb force averaged over one cylinder rotation stays constant with a varying system size scale, while the average arresting torque increases linearly as the system size increases. Assuming that the craft maintain a constant density of 100 kg/m<sup>3</sup> as the sizes scale, the cylinder mass and inertia increase accordingly:

$$m_2 \sim \text{scale}_2^3 \quad (3.45)$$

$$I_2 \sim \text{scale}_2^5 \quad (3.46)$$

Previous work suggests a linear correlation between satellite launch mass and equivalent radius,<sup>70</sup> in which case the mass scales linearly while the inertia scales cubically. From Eq. (3.39) and (3.44), the de-spin time and system displacement increase drastically as the entire system size increases, making it harder to de-tumble large debris satellites even if the control craft increases equally in size.

#### **3.4.4 Servicing Craft Size**

A likely mission scenario is one where the goal is to de-spin a given satellite with specific dimensions. In this case, when designing the mission, the servicing spacecraft must be sized to optimize de-spin performance. The averaged single rotation simulation is run for various servicing craft diameters (where the baseline is a 1 m diameter), while the surface to surface separation distance is held constant at 5 m. Because the MSM spheres used to model the servicing craft spread further and further apart as the craft grows, a higher fidelity model is used with 138 spheres on the debris cylinder and 100 spheres on the control craft. As can be seen in Figure 3.10, the averaged Coulomb force and torque initially grow with increasing servicing craft diameter, because the capacitance and the charge increase for a given control voltage. At larger diameters, however, the Coulomb torque drops back off because the charge that is distributed along the nonadjacent surface of the control craft becomes further and further removed from the debris cylinder. As a result, the optimal de-spin performance considering this particular cylinder occurs with a control craft diameter of 7.9 m, with diminishing returns evident at larger sizes. The system displacement is minimized at a control craft diameter of 2.6 m. Besides this tradeoff, one must consider the added structural complexity, launch cost, and charging power requirements of flying a large servicing craft.

#### **3.4.5 Debris Aspect Ratio**

While not a mission design parameter, it is important to consider what effect the aspect ratio of the debris object has on performance, so that suitable targets for de-spin operations may be selected. Figure 3.11 shows how the simulation results depend on a varying cylinder length,

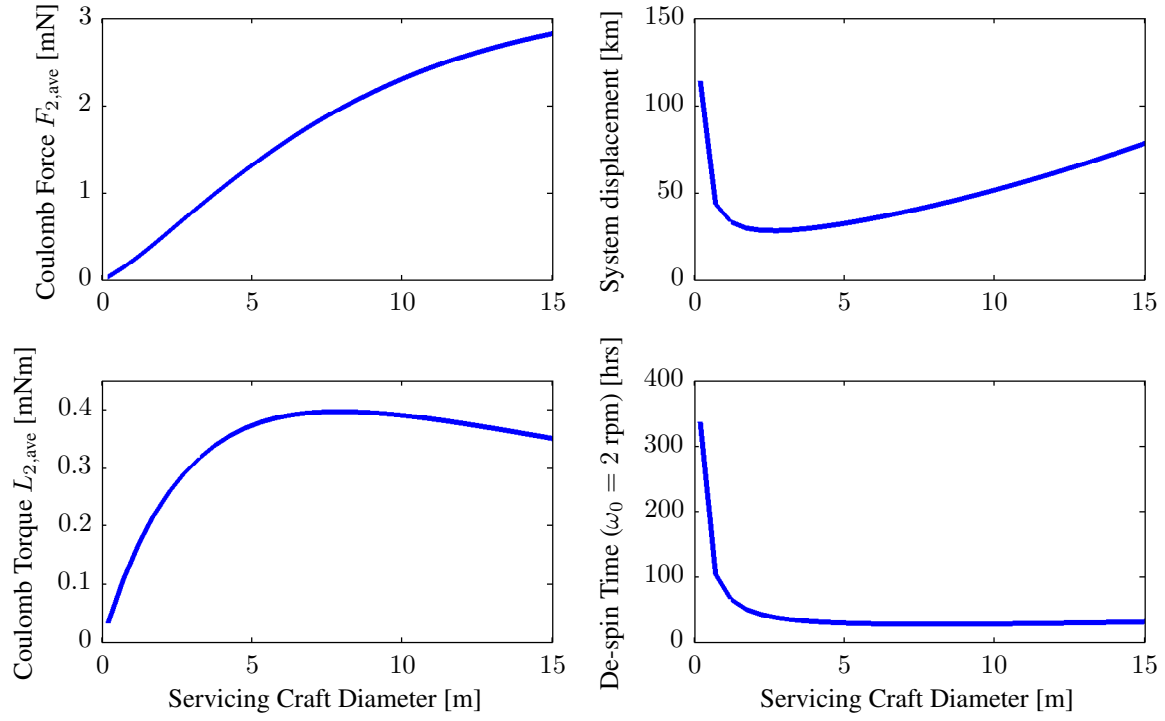


Figure 3.10: Performance dependency on servicing craft size

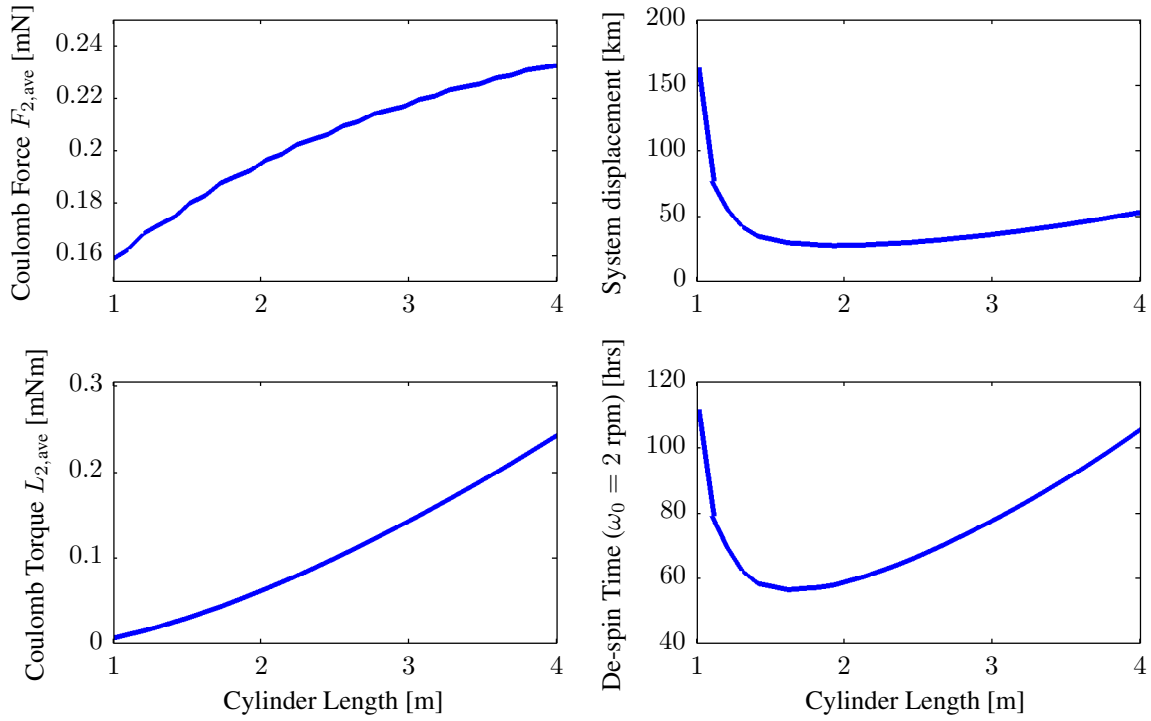


Figure 3.11: Performance dependency on debris aspect ratio

while the diameter is held constant at 1 m. It is assumed that the same minimum surface to surface separation distance is maintained to mitigate the collision risk. Again, the higher fidelity MSM is used, with the same sphere spacing as above (the number of spheres used on the cylinder now depends on cylinder length). Interestingly, the shortest de-spin time occurs with a cylinder of length 1.6 m, which represents a relatively small aspect ratio. While a longer aspect ratio results in higher Coulomb torques due to a larger moment arm, this trend is only roughly linear because the center to center separation distance also increases as the cylinder length grows. Mass increases linearly with cylinder length, while the moment of inertia increases to higher order. As a result the de-spin time and system displacement become larger for more slender cylinders.

### 3.5 Relative Position and Orientation Control Schemes

Besides designing the remote electrostatic de-spin mission with optimal sizing parameters as deduced from the previous section, the servicing spacecraft has the freedom to control its position and orientation in space with respect to the rotating debris object. The effects of several novel control schemes are herein analyzed. Generally, these approaches result in improvements in de-spin performance, which come at the cost of increased control forces and torques and therefore greater expenditures of fuel or power. Because this analysis deals with varying relative positions, the full temporal simulation with translational freedom from Section 3.3 is employed. The results, as discussed in the following sections, are compared to the baseline simulation and outlined in Table 3.3.

Table 3.3: De-spin control schemes results

	$\Delta t$ [hrs]	$\Delta X$ [km]	$F_{\text{thrust,ave}}$ [N]	$L_{\text{att,ave}}$ [Nm]
Baseline	74.32	34.37	0.001296	N.A.
Variable Separation Distance	65.27	31.29	2.073	N.A.
Circumnavigation	37.56	N.A.	5.402	N.A.
Non-spherical Control Craft	56.88	29.62	0.001185	0.09974



### 3.5.1 Variable Separation Distance

In the baseline control scheme, the center to center separation distance between the two craft is held constant. In order to mitigate the collision risk that poses a threat to mission success, it is actually the surface to surface separation distance that should be maintained at a minimum distance. Therefore, a position control scheme is envisioned where the control craft moves back and forth along the straight line of separation as the cylindrical debris rotates, maintaining a constant separation from the closest surface. Figure 3.12 shows the resulting desired center to center separation distance of the objects over one full rotation of the cylinder. As is evident, the control craft moves slightly further away than the baseline 7 m separation when the edge of the spinning cylinder is at closest approach.

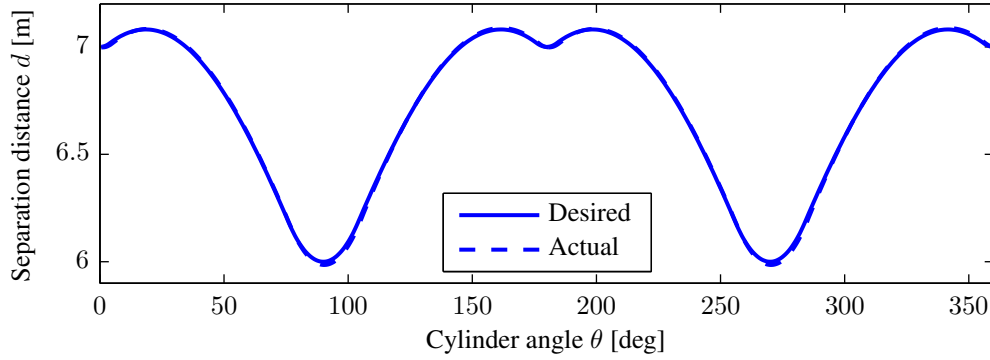


Figure 3.12: Object separation for constant surface to surface distance

A proportional-derivative position feedback control is implemented, utilizing the analytic derivative of the desired separation. This control maintains the relative position of the craft to within 0.021 m of the desired separation. Table 3.3 shows that the time to de-spin 12 deg/s of rotation decreases to 65.27 hours, which represents a 12.1% increase in performance. However, the average required thrusting force increases dramatically to 2.073 N, which falls outside the range of most existing fuel-efficient propulsion technology, and would require several hundred kilograms of expended fuel using conventional bi-propellant thrusters. One can conclude that the marginal gains in performance are not worth such a large cost in fuel requirements.

### 3.5.2 Circumnavigation Scheme

As the nonspherical debris object rotates, there are certain configurations for which the Coulomb control torque diminishes. Namely, when the cylinder is oriented parallel or perpendicular to the spherical servicer, no electrostatic moment is achievable. This presents the motivation for the following position control scheme, where the servicing craft circumnavigates the debris object as it rotates in order to maintain the optimal relative angle to the cylinder for maximum control torque. The same position control algorithm as before is used with larger gains to maintain a relative angle of  $\theta = 42.38^\circ$ , at which the cylinder experiences the maximum torque. As can be seen in Figure 3.13, this scheme results in a very minute system displacement because the net Coulomb forces cancel out as the servicing craft rotates around the debris object. Because the system constantly experiences the maximum achievable torque, de-spin time is reduced by 49.5% to a mere 37.56 hours. As in the previous simulation, the thrusting force necessary to maintain this relative orbit increases several orders of magnitude to 5.402 N. In this scenario, the fuel requirement

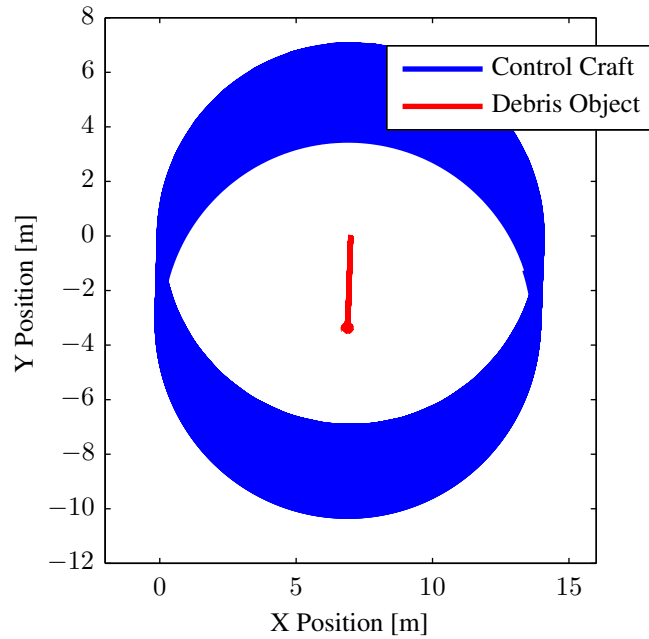


Figure 3.13: Position of craft in circumnavigation scheme

might be reduced if certain natural circumnavigation formation flying orbits are employed, as will be addressed during future investigations.

### 3.5.3 Non-spherical Control Craft

Next, a scenario is considered wherein the control craft is no longer modeled as a conducting sphere. If de-spin gains can be achieved by adjusting the attitude of the servicer, it may be possible to improve mission performance by use of rechargeable attitude control devices rather than expending thruster fuel reserves. While a cylindrical control craft was first considered, the desired attitude profile is much more efficient using the windmill configuration depicted in Figure 3.14. While the dimensions of the three sphere MSM are used, it is assumed that each of the external spheres can be charged independently. A constant relative position  $d = 8$  m is maintained between the spacecraft, which represents the same surface to surface separation as before. Now, however, the control craft can adjust its relative orientation to the rotating debris cylinder and specify a voltage  $\phi_{1,i} = \pm 30$  kV on any of the four external craft while the rest of the body is held at 0 kV. This will require a complex configuration of charge control devices and charge isolation surfaces.

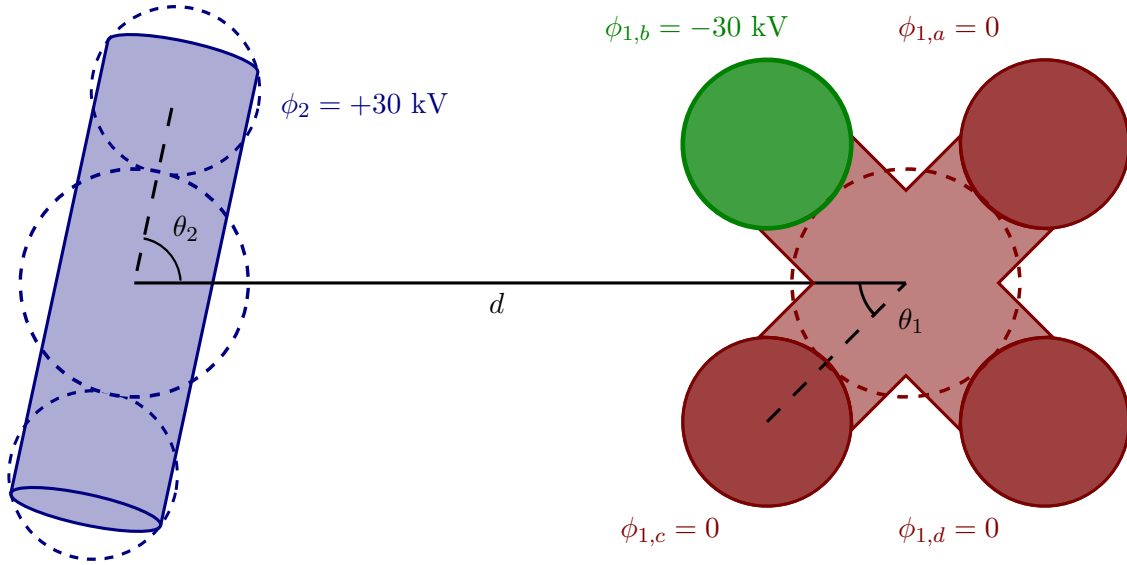


Figure 3.14: Configuration for windmill control craft

In order to determine an appropriate control strategy, Figure 3.15 shows the Coulomb torque experienced by the debris cylinder, dependent on the orientation of both objects. The control craft angle  $\theta_1$  varies between  $-90^\circ$  and  $+90^\circ$ , which corresponds to one of the two closest spheres in Figure 3.14 being charged. With the potential of the debris cylinder held at  $\phi_2 = +30$  kV, the left plot shows the attractive torques resulting from  $\phi_{1,i} = -30$  kV while the right plot shows the lesser torques that result from  $\phi_{1,i} = +30$  kV. The superimposed lines show the maximum achievable counter-clockwise (red) and clockwise (blue) torque that is possible for a given debris object orientation  $\theta_2$ . From this, one can deduce the desired servicing craft attitude  $\theta_1$  and which sphere should be charged. If the cylinder in Figure 3.14 with orientation  $\theta_2 \approx 80^\circ$  is spinning counter-clockwise, we wish to arrest it with a clockwise torque. Accordingly, an attractive torque should be applied with  $\theta_1 \approx -45^\circ$ ; thus an electric potential  $\phi_{1,b} = -30$  kV must be applied to sphere b.

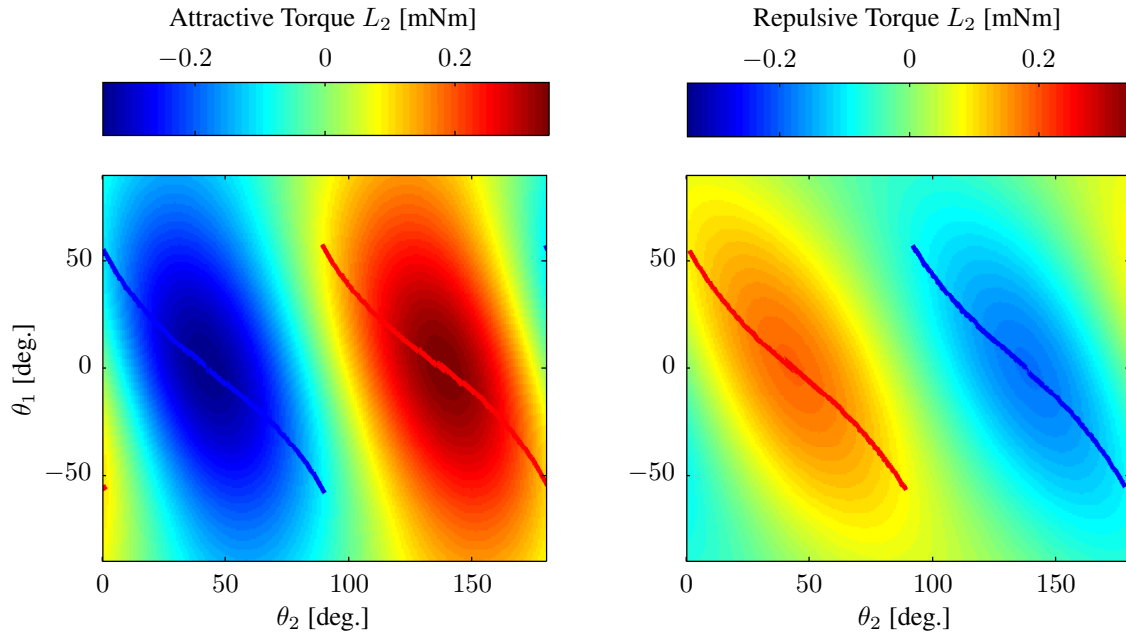


Figure 3.15: Coulomb torque dependency on debris and control craft angles

The results for the first minute of the scenario where the control craft can determine its relative orientation and which component is charged up are displayed in Figure 3.16. The top plot

shows what desired angle is determined from the data in Figure 3.15, what angle this corresponds to for the craft once the appropriate sphere to charge is chosen, and what angle is achieved by the attitude control algorithm during the simulation. A proportional-derivative control algorithm is implemented, where the desired rotation rate is assumed to be equivalent to the debris rotation (a linearization of the curves in Figure 3.15). The middle plot in Figure 3.16 shows which sphere is given what voltage, and the bottom plot shows the required control moments on the servicing craft.

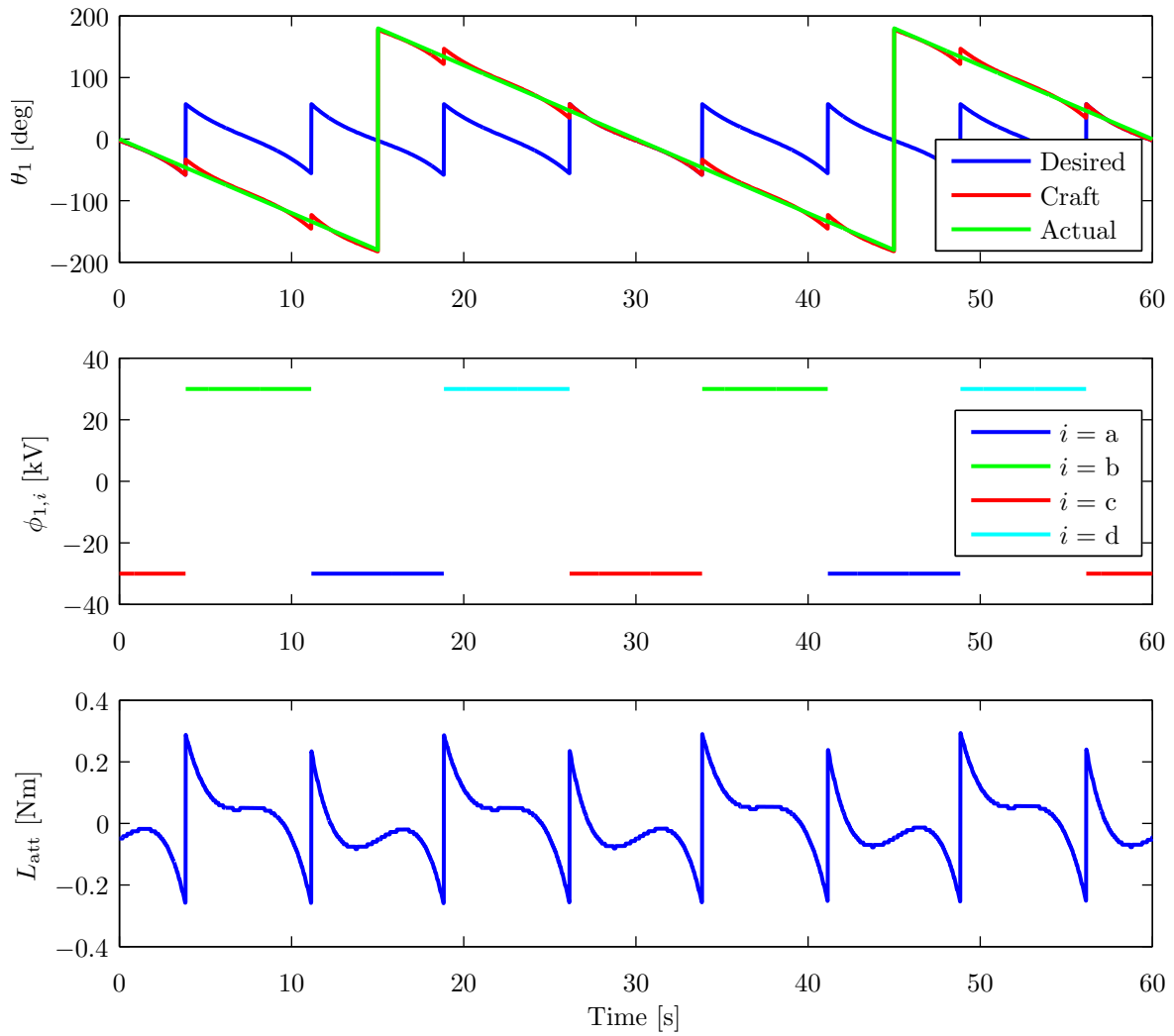


Figure 3.16: Results from windmill control craft scenario

In Table 3.3, it is clear that the time to remove a 12 deg/s rotation on the debris object takes only 56.88 hours, a 23.5% improvement in performance. System displacement and required thrusting are reduced, while only an average of less than one tenth of a Nm control moments are required, easily achievable using conventional reaction wheels. Moreover, since the required torques are symmetric, the control moment devices will not require frequent momentum dumping. Therefore, this scenario represents a considerable performance benefit without a significant fuel cost.

### 3.6 Asteroid De-spin

NASA has recently considered retrieving a small asteroid 10s of meters in size, and returning it to the near-Earth environment. In light of this Asteroid Retrieval Mission (ARM), the logical question is posed whether the technology to electrostatically detumble man made objects in Earth orbit may be extended to perform a de-spin maneuver on a near Earth asteroid (NEA). The goal is to robotically capture a suitable asteroid within the decade and transport it to a high lunar orbit so that a crewed mission may rendezvous with it to collect and retrieve samples. According to NASA’s Summer 2013 Asteroid Initiative Request for Information (RFI), “NASA is interested in concepts for systems to capture and de-spin an asteroid with the following characteristics:

- (a) Asteroid size:  $5\text{ m} < \text{mean diameter} < 13\text{ m}$ ; aspect ratio  $< 2/1$ .
- (b) Asteroid mass: up to 1,000 metric tons.
- (c) Asteroid rotation rate: up to 2 revolutions per minute about any axis or all axes.
- (d) Asteroid composition, internal structure, and physical integrity will likely be unknown until after rendezvous and capture.”

A significant challenge of such a mission is how to capture the tumbling asteroid. A feasibility study sponsored by the Keck Institute for Space Studies proposes to capture the asteroid using a high strength ‘bag’ held open by several arms and a ring to constrain the asteroid position and attitude.<sup>15</sup> The spacecraft guidance subsystem would use Radar-Altitude aided relative position

estimates to match the surface velocity and spin state of the target during capture. Considering that these pose algorithms are largely untested, and an asteroid of the dimensions and spin rate mentioned above exhibits up to 6 MJ of rotational kinetic energy, it would be beneficial to reduce the rotation of the asteroid as much as possible.

A simulation is created to estimate the time scales required to de-spin an asteroid with the specifications given in NASA's RFI regarding asteroid capture. Developing a realistic asteroid surface charging model is very challenging. The most optimistic case treats the surface as fully conducting. Naturally, the asteroid surface is not conducting, and only local charging of the regolith would be achieved. A balanced charging scheme where local surfaces obtain charge as described below is implemented. If this optimistic scenario leads to detumble times that are too long to be practical, it would illustrate that a more realistic charging model would only yield worse performance.

A surface populated MSM is used to determine the electrostatic interaction between a cylindrical asteroid and a nearby spherical control craft. The spacecraft uses a focused electron gun to induce an electric potential of  $-30$  kV on the adjacent half of the asteroid, while using a separate charge control device pointed to deep space to maintain a  $+30$  kV potential on its own body. It is assumed that the composition of the asteroid is such that the affected surface (within the field of view of the charge transfer device) will acquire the desired potential while there is sufficient insulation within the body that the rest of the asteroid maintains zero potential. The current balance for the asteroid assures that an asteroid MSM sphere not targeted by the electron gun balances to the nominal zero potential. The charge resides only on the spheres targeted by the electron gun emission. This scheme is maintained for a full rotation of the asteroid around its minor axis to determine the average achievable torque. One frame of this simulation is shown in Figure 3.17, with the electrostatic potential and charge distribution visible on both bodies each populated with 107 MSM spheres.

The cylindrical asteroid is chosen to have a 12 m length and 6 m diameter, giving it a mass of 678 metric tonnes, assuming an average density of  $2000 \text{ kg/m}^3$ . The representative asteroid

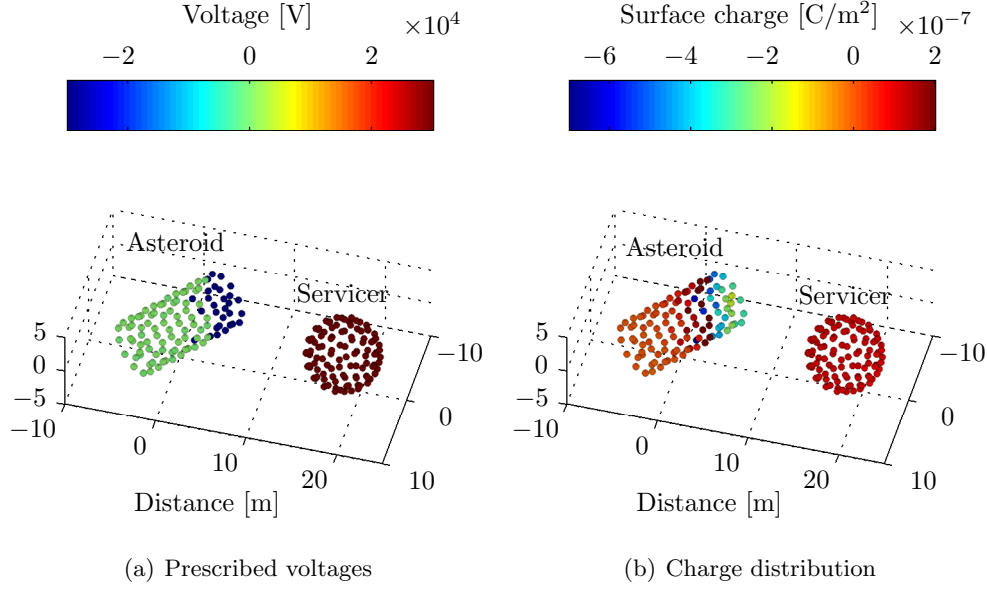


Figure 3.17: Voltage and charge distribution on the servicer craft and asteroid in de-spin simulation.

geometry and assumed simple density model resides in the middle of the size and weight range from the NASA RFI, with the most favorable torque aspect ratio of 2:1. The servicer craft is modeled as an 8 m diameter sphere, which is reasonable given that it is meant to capture the asteroid and transport it back to a lunar orbit. Using a surface to surface separation distance of one spacecraft diameter, an average torque of 19.5 mNm is achievable, which means that it would take 600 days, nearly 2 years, to remove one revolution per minute about the minor inertia axis of the asteroid. While adjusting certain simulation parameters might result in slight increases in performance, it is fairly unfeasible that the asteroid retrieval mission will allow for this much time for detumble operations. If long duration missions are implemented, such detumble durations can be simultaneous with a tugging effect allowing a low thrust trajectory to be simultaneously utilized. In general, the achievable torques are quite impressive and could be utilized for de-spin maneuvers on wayward GEO satellites in days or weeks. However, the inertias involved with a rotating asteroid are simply too large, yielding detumble times of a year or longer even with the highly optimistic assumption that the surface is conducting.



## Chapter 4

### Charge Transfer Analysis

In the previous chapter's control and sensitivity developments, it has been assumed that electrostatic potentials on both craft to  $\phi_i = \pm 30$  kV are achievable. In this section, analysis is performed to determine how to achieve those voltage levels using charge transfer devices on the servicing satellite. The voltage attained by a spacecraft is a complex function of the various currents to which it is exposed in the space plasma environment. These currents, which result from electron and ion plasma flux, the photoelectric effect, incoming and outgoing charged beam currents, and secondary electron emissions from incoming beams, must balance to create a steady state system, which in turn determines the achieved voltage levels.<sup>46</sup> The currents depend significantly on a multitude of parameters that describe the behavior of the space environment. Constants representative of a nominal environment at GEO altitudes are chosen for this development, but it is important to remember that these parameters may change during solar storm events, which would significantly affect the results. If the actual conditions are prohibitive to the intended de-spin operations, actuation may be suspended until more favorable weather returns.

Previous studies have analyzed the charge transfer capabilities when a single electron beam is directed from a servicer craft to a debris object, primarily to achieve an attractive Coulomb force for electrostatic tugs.<sup>32,33,74</sup> These efforts determine what voltage levels were achievable on both vehicles for a given electron beam energy and current, and highlight that the capabilities are largely dependent on the relative sizes of the craft. If a second charge transfer device is added to the control satellite, as in Figure 4.1, a greater range of potential levels is achievable. In this

analysis, the goal is to determine the transfer and external beam currents and energy necessary to achieve the desired voltage levels assumed previously. Moreover, consideration is given to the total power expelled by the charge transfer devices, as well as the momentum that the beams impart on the craft.

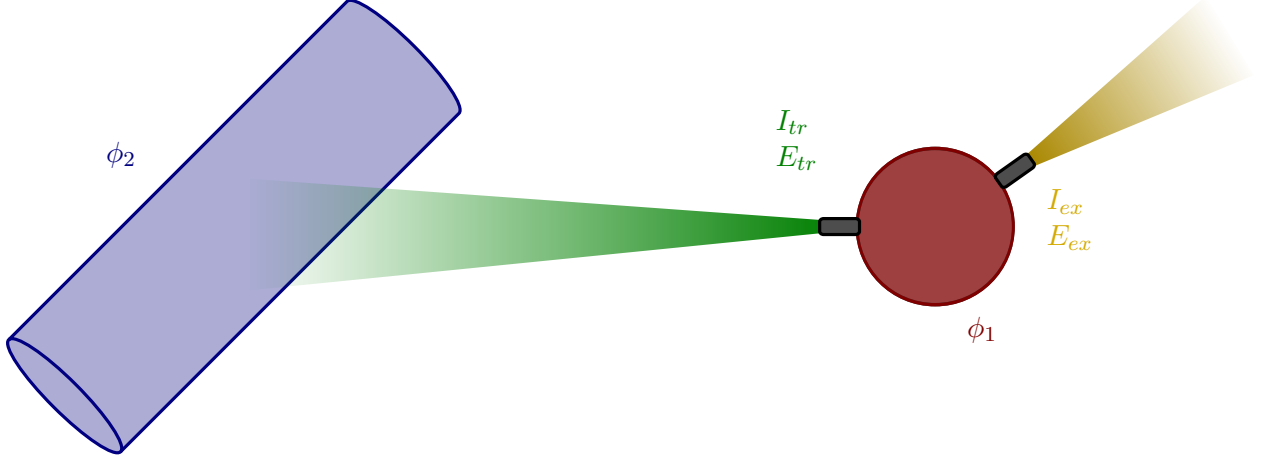


Figure 4.1: Depiction of charge transfer between craft

#### 4.1 Current Balance

The charging model developed in Reference 74 is used to compute the various currents experienced by the spacecraft. The nominal GEO plasma parameter values used are given in Table 4.1. A photoelectron current occurs whenever a craft is in sunlight, given by:

$$I_{ph}(\phi) = j_{ph,0} A_{\perp} e^{-\phi/T_{ph}} \quad \phi > 0 \quad (4.1a)$$

$$= j_{ph,0} A_{\perp} \quad \phi \leq 0 \quad (4.1b)$$

where  $T_{ph}$  is the temperature of the emitted photoelectrons,  $j_{ph,0}$  is the photoelectron flux, and  $A_{\perp}$  is the cross-sectional area exposed to sunlight. For the cylinder, an average between the transverse and longitudinal cross-sectional areas is used to capture both orientations it may have with respect to the sun. The exponential term in Eq. 4.1a decays so rapidly that in this study the photoelectron current is assumed to be negligible for positive voltages, i.e.  $I_{ph} = 0$  for  $\phi > 0$ .

The plasma electron current is modeled by

$$I_e(\phi) = -\frac{Aq_b n_e w_e}{4} e^{\phi/T_e} \quad \phi < 0 \quad (4.2a)$$

$$= -\frac{Aq_b n_e w_e}{4} \left(1 + \frac{\phi}{T_e}\right) \quad \phi \geq 0, \quad (4.2b)$$

where  $A$  is the total surface area exposed to the plasma environment,  $T_e$  is the plasma electron temperature,  $n_e$  is the plasma electron density,  $q_b$  is the elementary charge,  $m_e$  is the electron mass, and  $w_e = \sqrt{8T_e/\pi m_e}$  is the thermal velocity of the electrons. Similarly, the plasma ion current is computed using

$$I_i(\phi) = \frac{Aq_b n_i w_i}{4} e^{-\phi/T_i} \quad \phi > 0 \quad (4.3a)$$

$$= \frac{Aq_b n_i w_i}{4} \left(1 - \frac{\phi}{T_i}\right) \quad \phi \leq 0, \quad (4.3b)$$

where the subscript  $i$  denotes ions instead of electrons in each of the parameters mentioned above, and  $w_i = \sqrt{8T_i/\pi m_i}$ . As in previous studies, the ion population is assumed to consist solely of protons. For positively charged spacecraft, the current is negligible due to the exponential term in Eq. 4.3a, such that  $I_i = 0$  for  $\phi > 0$ .

The charge control exerted by the servicing spacecraft comes from either ion or electron beams. These charge control devices emit a current of particles  $I_B$  with an energy  $E_B$  relative to the craft potential.  $I_B > 0$  denotes that electrons are emitted from the control craft, while  $I_B < 0$  denotes expulsion of ions. In order to achieve emission, the energy of the beam must be sufficiently large for the particles to escape the electric influence of the charged craft. Assuming the beam energy is always positive ( $E_B > 0$ ) and  $q$  represents the charge of the particles (electrons are negative, ions are positive), the total energy of the particles must be positive for successful emission, i.e.  $E_B + q\phi_1 > 0$  or  $E_B > -q\phi_1$ . Using this relation, which holds for both the transfer and external beam, electrons are emitted from a negative craft with only minimal beam energy, as with ions from a positive craft.

In order to achieve charge control on the passive debris object, the transfer beam must be focused on the surface of the cylinder. They will be absorbed if there is enough energy left after

leaving the servicer to overcome the debris' electrostatic potential barrier. This is modeled by

$$I_{tr,2}(\phi_2) = -\alpha I_{tr} \quad E_{tr} > q(\phi_2 - \phi_1) \quad (4.4a)$$

$$= 0 \quad E_{tr} \leq q(\phi_2 - \phi_1) \quad (4.4b)$$

where  $\alpha$  represents the efficiency of the transfer, which is assumed to be 1, and the current on the debris is opposite that experienced by the servicer.

When the transfer beam consists of electrons and impacts a negatively charged debris object, the incoming electrons result in the emission of secondary electrons. Because of the negative potential of the debris object, these electrons will escape, resulting in a significant current source. This secondary electron emission is modeled by<sup>22</sup>

$$I_{SEE}(\phi_2) = -4Y_M I_{tr,2}(\phi_2)\kappa \quad \phi_2 < 0 \text{ and } I_{tr} > 0 \quad (4.5a)$$

$$= 0 \quad \phi_2 \geq 0 \text{ or } I_{tr} < 0, \quad (4.5b)$$

where

$$\kappa = \frac{E_{\text{eff}}/E_{\text{max}}}{(1 + E_{\text{eff}}/E_{\text{max}})^2}$$

and  $E_{\text{eff}} = E_{tr} - q(\phi_2 - \phi_1)$ .  $Y_M$  is the maximum yield of secondary electron production, and  $E_{\text{max}}$  is the impact energy at which this maximum occurs.

It is important to understand the simplifications inherent in the charge transfer model defined above. The electron and ion plasma flux are derived using the conservation of momentum of particles that come in the vicinity of the spacecraft. This approach is valid for low density plasmas with high Debye lengths, also known as the orbit limited regime, because the attracted plasma sheath exists relatively far away from the spacecraft.<sup>46</sup> When two oppositely charged spacecraft are located nearby within this sheath, as is the case for our study, the averaged dynamics of the incoming particles could be significantly different. Full particle-in-cell simulations would be required to model this system with higher fidelity. Also, the interaction of secondary electron emission particles between the two craft is not considered here, which may occur when the debris object is charged negatively and the servicer is positive. As such, this study serves more as an

Table 4.1: Plasma environment parameters for current balance

Parameter	Value	Units	Description
$T_{ph}$	2	eV	Temperature of emitted photoelectrons
$j_{ph,0}$	20	$\mu\text{A}/\text{m}^2$	Photoelectron flux
$q_b$	$1.60 \times 10^{-19}$	C	Elementary charge
$m_e$	$9.11 \times 10^{-31}$	kg	Electron mass
$T_e$	1250	eV	Plasma electron temperature
$n_e$	0.6	$\text{cm}^{-3}$	Plasma electron density
$m_i$	$1.67 \times 10^{-27}$	kg	Ion (proton) mass
$T_i$	50	eV	Plasma ion temperature
$n_i$	9.5	$\text{cm}^{-3}$	Plasma ion density
$Y_M$	2	—	Maximum yield of SEE
$E_{\max}$	300	eV	300

initial investigation into the approximate charge transfer requirements than a prediction of the actual electron and ion gun operation.

## 4.2 Power Requirements and Momentum Transfer

The power required to operate the charge transfer devices is a function of the adjustable beam energy and current, as follows:

$$P_B = \frac{E_B |I_B|}{q_b} \quad (4.6)$$

Besides the power used to accelerate the expelled ions or electrons, charge transfer guns also require a considerable amount of overhead power that is larger than the acceleration levels determined in this study. Moreover, ion guns are much more complex and require higher power levels to operate than electron guns.

Meanwhile, the expulsion or absorption of particles by a spacecraft results in a transfer of momentum to the craft. The force imparted can be computed using Newton's second law:

$$F_B = \frac{dp}{dt} = \frac{I_B}{q_b} m_p v_\infty \quad (4.7)$$

where the momentum of the particles once they've left the electric influence of the craft is used ( $m_p v_\infty$ ) and the beam current gives the rate at which particles leave the craft ( $I_B/q_b$ ). The velocity

is determined by an energy balance between the particles' initial potential energy and final kinetic energy:

$$v_{\infty} = \sqrt{\frac{2(E_B + q\phi_1)}{m_p}} \quad (4.8)$$

Argon is selected as the low mass species for the ion gun, with particle mass  $m_p(\text{Ar}^+) = 6.63 \times 10^{-26}$  kg. The momentum imparted on the debris object by the incoming transfer beam is equal to that felt by the servicing craft, because the particles impact the debris at the same rate and with the same far field momentum as they leave the servicer.

There are two possible ways to achieve attractive control (positive debris, negative servicer, or negative debris, positive servicer) and two ways to achieve repulsive control (both positive or both negative). The approaches are interchangeable with regard to the system dynamics and attitude control development, but distinctions do exist when considering the charge transfer requirements. For now, let's assume that the debris craft is held at a constant potential, while the polarity of the control craft is switched to alternate between attraction and repulsion. For simplicity, the desired magnitude is always assumed to be  $|\phi_i| = 30$  kV for both craft.

### 4.3 Positive Potential Debris Craft

First, analytic current balance methods are used to determine the equilibrium transfer and external beam currents and energies to achieve the desired potentials. If the debris potential is held positive, the only currents acting on the craft are the transfer beam current and the plasma electron flux. Other currents such as the photoelectric effect, plasma ion flux, and secondary electron effects are nonexistent or negligible. By enforcing a net zero current balance

$$I_{tr,2} + I_{e,2} = 0 \quad (4.9)$$

the required transfer beam current can be solved analytically.  $I_{tr} = -156.3 \mu\text{A}$ , which represents that the beam needs to consist of ions as is logical to achieve a positively charged debris object. For a negative control craft, the energy of the transfer beam must be 60 keV to achieve charge transfer according to Eq. 4.4a. As a result, the transfer beam draws 9.38 W of power, which is a

minimal amount in the scheme of most spacecraft power budgets. This ion beam does impart a  $24.63 \mu\text{N}$  force on both vehicles in the system, which is an order of magnitude smaller than the average Coulomb forces involved.

Equating the current balance on the control craft yields an analytic solution for the external beam current:

$$I_{ex} = -I_{tr} - I_{ph,1} - I_{e,1} - I_{i,1} \quad (4.10)$$

This results in a positive external current  $I_{ex} = 61.26 \mu\text{A}$ , meaning a beam of electrons is required to offset the transfer current and achieve the desired  $\phi_1 = -30 \text{ kV}$ . These electrons are naturally repelled by the negative craft, so they require minimal energy and the electron gun requires negligible power. These results are summarized in the top half of Table 4.2.

If repulsive control is desired with a positive debris object, the transfer beam current is identical via Eq. 4.9, but the transfer ions don't require any excess energy and the power is minimal. A much higher external electron current is necessary to bring the control craft to a positive potential, as determined using Eq. 4.10 where the ion plasma and photoelectron current can be neglected. The external electron beam requires an energy of  $E_{ex} = 30 \text{ kV}$  to escape the craft, which draws  $6.03 \text{ W}$  of power and imparts no force on the control craft because the electrons have no excess energy.

Table 4.2: Charge beam characteristics for positive debris craft

	Transfer	External	$P_{\text{tot}}$
$\phi_2 = +30 \text{ kV}$ $\phi_1 = -30 \text{ kV}$	$I_{tr} = -156.3 \mu\text{A}$ (ions) $E_{tr} = 60 \text{ keV}$ $P_{tr} = 9.38 \text{ W}$ $F_{tr} = 24.63 \mu\text{N}$	$I_{ex} = 61.26 \mu\text{A}$ ( $e^-$ ) $E_{ex} = 0 \text{ keV}$ $P_{ex} = 0 \text{ W}$ $F_{ex} = 0.036 \mu\text{N}$	<b>9.38 W</b>
$\phi_2 = +30 \text{ kV}$ $\phi_1 = +30 \text{ kV}$	$I_{tr} = -156.3 \mu\text{A}$ (ions) $E_{tr} = 0 \text{ keV}$ $P_{tr} = 0 \text{ W}$ $F_{tr} = 24.63 \mu\text{N}$	$I_{ex} = 200.9 \mu\text{A}$ ( $e^-$ ) $E_{ex} = 30 \text{ keV}$ $P_{ex} = 6.03 \text{ W}$ $F_{ex} = 0 \mu\text{N}$	<b>6.03 W</b>

To gain insight into the charge up process, a simulation of the time history of the charge and

voltage on both spacecraft is created. The state vector of this simulation is the charge on the debris and the servicer. At each time step, the MSM is used to determine the voltage on both craft. Since the total charge is distributed in some unknown way between the spheres in the cylinder MSM model, the floating charge approach outlined in Section 2.8.2 is used. The net current on each craft is calculated using the electric potentials, which yields the time derivative of the state vector. Transfer and external beam currents and energies given in Table 4.2 are used. The simulation starts from net zero charge levels, and switches between attractive and repulsive polarity every quarter of a second.

As is evident from the results in Figure 4.2, the desired voltage levels are achieved in roughly 0.1 seconds. This is a much faster than the polarity switching necessary to match the expected rotation rates of the debris. When the polarity control is switched, the debris potential first dips because the transfer beam energy has reduced to 0 eV. Once the control craft potential reaches the same potential, charge transfer is re-engaged and both craft quickly climb to the desired levels. This occurs during parallel or perpendicular orientations of the debris, at which point the control moments are minimal anyway.

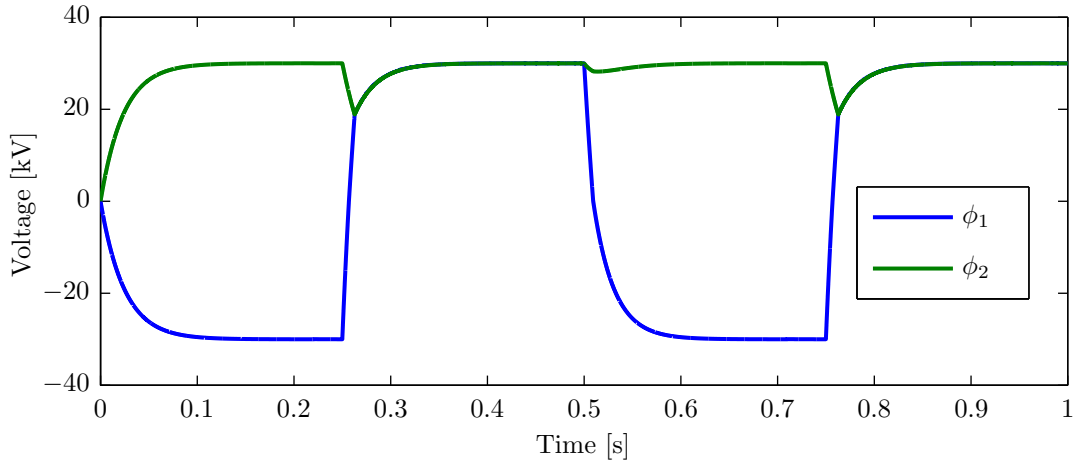


Figure 4.2: Time history of charge control with positive debris craft



#### 4.4 Negative Potential Debris Craft

If the debris spacecraft is kept at negative potential levels, its current balance relationship becomes more complicated:

$$I_{ph,2} + I_{e,2} + I_{i,2} + I_{tr,2} + I_{SEE,2}(I_{tr}, E_{tr}) = 0 \quad (4.11)$$

This equation is a function of both the transfer current  $I_{tr}$  and energy  $E_{tr}$ , so multiple combinations exist to achieve the desired debris voltage  $\phi_2 = -30$  kV. The required current can be solved analytically for a given transfer beam energy:

$$I_{tr} = \frac{I_{ph,2} + I_{e,2} + I_{i,2}}{1 - 4Y_M \kappa(E_{tr})} \quad (4.12)$$

Figure 4.3 shows the transfer beam current at various energies, for a positive control spacecraft ( $\phi_1 = +30$  kV) on the left and a negative control craft ( $\phi_1 = -30$  kV) on the right. The optimal combination is chosen so that the expended power by Eq. 4.6 is minimized, using a golden section search and parabolic interpolation.<sup>14,25</sup> The results for the attractive and repulsive scenario with a negative debris object are summarized in Table 4.3. The transfer beam current is sufficiently large in the attractive configuration that it would lead to excessive positive charging for the control craft. As a result, the external beam consists of ions for both cases.

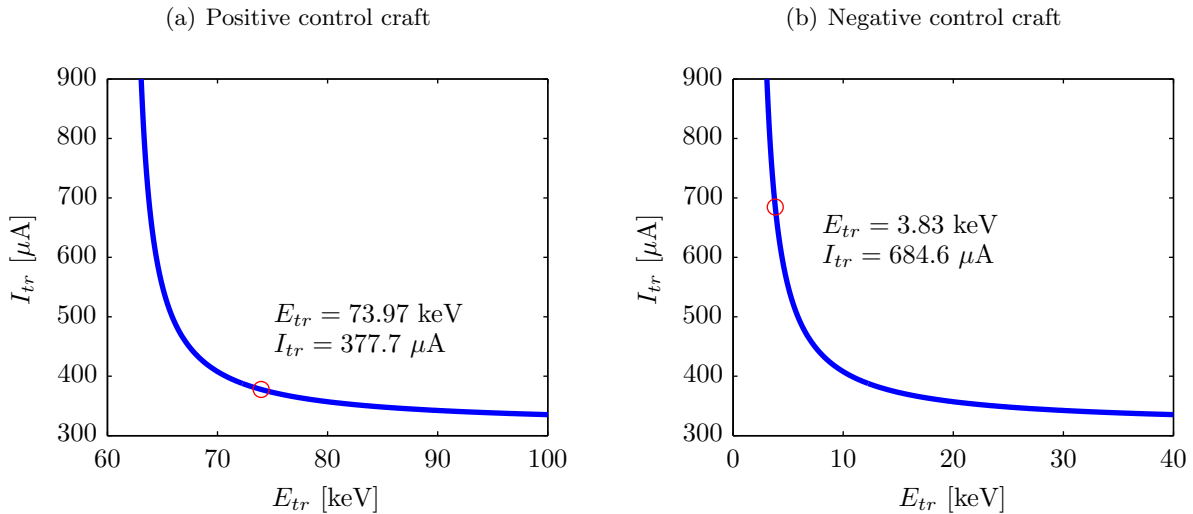


Figure 4.3: Power optimization for negative debris craft

Table 4.3: Charge beam characteristics for negative debris craft

	Transfer	External	$P_{\text{tot}}$
$\phi_2 = -30 \text{ kV}$ $\phi_1 = +30 \text{ kV}$	$I_{tr} = 377.7 \text{ } \mu\text{A} \text{ (e}^-\text{)}$ $E_{tr} = 73.97 \text{ keV}$ $P_{tr} = 27.94 \text{ W}$ $F_{tr} = 0.267 \text{ } \mu\text{N}$	$I_{ex} = -333.0 \text{ } \mu\text{A} \text{ (ions)}$ $E_{ex} = 0 \text{ keV}$ $P_{ex} = 0 \text{ W}$ $F_{ex} = 52.48 \text{ } \mu\text{N}$	<b>27.94 W</b>
$\phi_2 = -30 \text{ kV}$ $\phi_1 = -30 \text{ kV}$	$I_{tr} = 684.6 \text{ } \mu\text{A} \text{ (e}^-\text{)}$ $E_{tr} = 3.83 \text{ keV}$ $P_{tr} = 2.62 \text{ W}$ $F_{tr} = 0.424 \text{ } \mu\text{N}$	$I_{ex} = -779.6 \text{ } \mu\text{A} \text{ (ions)}$ $E_{ex} = 30 \text{ keV}$ $P_{ex} = 23.39 \text{ W}$ $F_{ex} = 0 \text{ } \mu\text{N}$	<b>26.01 W</b>

As before, the power optimal results above are implemented in a time dependent simulation of the charge and voltage accumulations, shown in Figure 4.4. The debris quickly reaches the desired negative potential because of the higher transfer beam energy and current necessary to overcome the secondary electron emission. The kink in the control craft voltage at around 0.5 seconds is a result of the external beam engaging due to sufficient particle energy once the craft potential has reached zero. Generally, the operation shows stable and efficient charge buildup when switching between polarities.

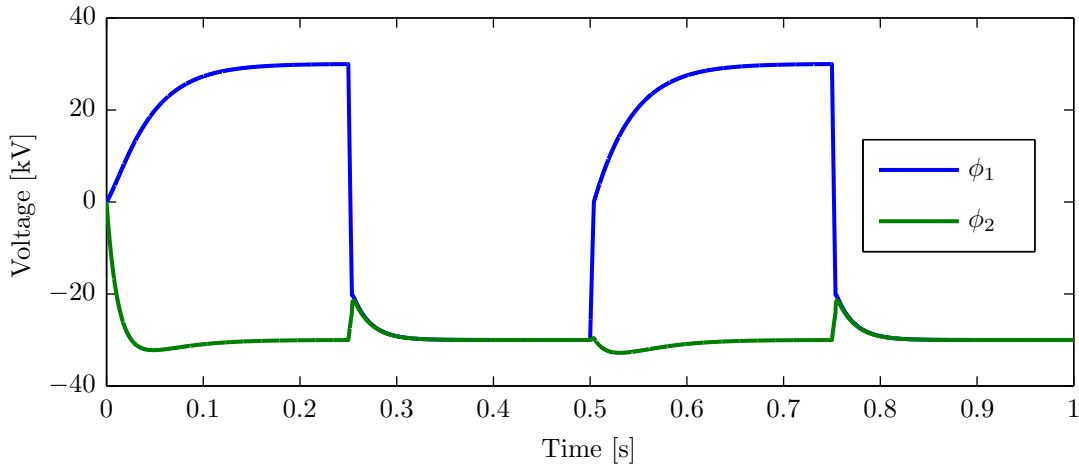


Figure 4.4: Time history of charge control with negative debris craft

The clear difference between the two charging options presented above is that maintaining a

positive debris craft potential requires about one third of the power consumption. This is primarily because of the secondary electron emission associated with exposing the debris object to an electron beam. Moreover, the interaction with the space plasma depends significantly on the polarity of the spacecraft potential. The maximum momentum transfer is roughly the same, considering the  $52.48 \mu\text{N}$  external force for the negative debris, positive servicer scenario acts only on the control craft, rather than the  $24.63 \mu\text{N}$  transfer beam force that acts on both vehicles with a negative debris object. For both cases, a single electron gun and a single ion gun are required on the servicing satellite. Only the energy and currents must be altered to switch the polarity of the control. Different charging combinations are possible if the control craft is held at a constant voltage while the polarity on the debris craft is switched, but this would require alternating which beams are directed where, a needless complication.

## Chapter 5

### Experimental Testbed

#### 5.1 Background

Validating spacecraft technology through economical terrestrial experiments is critical before costly on-orbit operations are performed. Simulating the low-friction microgravity space environment on Earth represents a ubiquitous challenge within this effort. Translational modes are generally required only when considering the relative motion of multiple spacecraft in formation flight, while rotational freedom is necessary to test the attitude control capabilities required by most satellites. The most common approach to generating frictionless motion is by use of air bearings, which have been incorporated into many spacecraft simulation testbeds since the beginning of the space age.<sup>76</sup> These testbeds range from low cost university efforts,<sup>62</sup> to complex government laboratory systems such as the Jet Propulsion Laboratory's Formation Control Testbed.<sup>61</sup> A high precision flat surface allows for horizontal translation and one degree of rotational motion. The air barrier can be supplied by pores in the stationary table or from within the mobile craft. Further rotational motion is possible via concentric spherical surfaces<sup>75</sup> or 1-D spindle air bearings.<sup>8</sup> When multiple modes are combined, systems with full translational and rotational freedom are possible.<sup>26</sup>

Actuation for air bearing testbeds is generally created by cold gas thrusters for translational motion and reaction wheels or control moment gyroscopes for attitude control. When validation of low thrust devices such as ion electrospray thrusters is required, other options such as magnetic levitation may be utilized.<sup>57</sup> Validating Coulomb actuation with a terrestrial testbed presents several additional challenges. In order to characterize the very low magnitude electrostatic forces

and torques, a high signal to noise ratio must be maintained by minimizing disturbances. Reducing the mass of any moving objects can help to increase their acceleration and discernible motion. Moreover, the system must be free of extraneous conducting parts in the presence of the high voltage components. The large electric fields can induce a non-uniform charge distribution within any metal parts, which in turn affects the performance of the system. Lastly, the charged objects require some connection with a high voltage power supply, which represents an extra disturbance for moving objects.

Recently, Seubert developed a dedicated terrestrial testbed for 1-D electrostatic relative motion in the Autonomous Vehicle Systems (AVS) lab at the University of Colorado Boulder.<sup>80,82</sup> This system, depicted in Figure 5.1, is designed to validate the fundamentals of the charged formation flight concept. The left side of the figure shows a stationary conducting sphere and one that slides freely on a custom air bearing track. Its position is tracked using a ranging laser system. Both spheres are connected to electrostatic power supplies that enable low current charging up to  $\pm 30$  kV. The entire system is operated from a desktop computer that interfaces with the electronics by means of a data acquisition card and a custom GUI developed with objective C code. Some limitations of the system are the noise in the laser measurement and a considerable time delay when

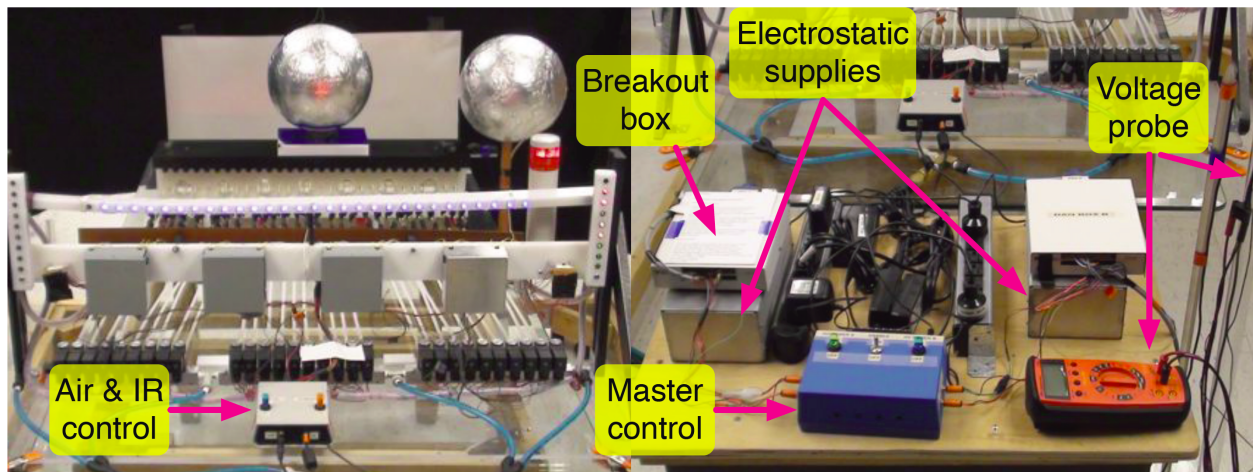


Figure 5.1: One-Dimensional Spacecraft Formation Flight Testbed for Terrestrial Charged Relative Motion Experiments

switching polarity with the power supplies. Seubert characterizes the disturbances caused by the air bearing track and charging cable on the mobile sphere, as well as electrostatic interference due to ionization of the air and polarization of the plastic testbed components.<sup>78</sup> Ultimately, the physical electrostatic interaction is modeled with a force model that exhibits plasma-like characteristics, and the sphere position is controlled with Coulomb forces using autonomous feedback algorithms.

In order to validate the remote electrostatic attitude control concept, a rotational Coulomb testbed is required. This system is developed in the AVS lab using the heritage of the translational testbed described above. The qualitative design requirements of this novel system are as follows:

- (1) Low friction rotational motion of nonspherical object.
- (2) Minimize moment of inertia of conducting geometry to increase accelerations.
- (3) Accurate sensing of angular position without disturbing motion.
- (4) Charge transfer from high voltage power supply without disturbing motion.
- (5) Quick polarity switching from power supplies.

The specifics of the testbed are described in the following section. Although they are outside of the scope of this research effort, several goals for expanding the capabilities of this system during future work have been identified. Operating the system within a vacuum chamber would allow for verification of the charge transfer model outlined in Chapter 4. Moreover, this would eliminate the atmospheric disturbances and create a more representative plasma environment. However, this would clearly prevent the use of any air bearing system for frictionless motion. Lastly, a testbed that allows for both translational and rotational motion would be necessary to verify the stationkeeping requirements for maintaining the desired relative motion between two craft.

## 5.2 Experimental Setup

A prototype testbed allowing rotational Coulomb charge control experiments was first introduced in Reference 87. While this testbed demonstrated that touchless de-spin control experiments

are feasible in a 1-G atmospheric environment, several hardware limitations were identified in this setup that restricted the performance to rotation rate control only. First, knowledge of the rotating object's angular positions was collected using a range-finding laser, which yielded noisy attitude data with insufficient accuracy. Second, active charge control was not implemented on the rotating cylinder. Rather, an initial voltage was applied to the cylinder whose gradual charge drain was characterized and modeled in the simulations. This resulted in a lack of repeatability and an inability to modulate the voltage on the cylinder during the experiment for precise control of the Coulomb torques. Lastly, the high voltage power supplies exhibited a time delay of up to one second when switching voltage polarity, thus considerably reducing the control authority in the case of large rotation rates.

Fig. 5.2 depicts the improved rotational testbed for Coulomb attitude control experiments, wherein all the above limitations are addressed. The conducting cylinder is attached with a threaded interface to a rotating shaft, which is secured by the two low friction ceramic bearings. A magnetic hub is mounted to the bottom of the shaft, whose orientation is measured to within  $0.35^\circ$  accuracy by the absolute 10-bit analog encoder. Analysis and testing show that the magnetic fields produced by the charged rotating cylinder are sufficiently small and do not interfere with the operation of the encoder. Charge is transferred to the rotating cylinder from a Spellman CZE 2000 high voltage power supply (HVPS) via a  $< 1$  mm gap between the charging cable and a copper bushing situated on the rotating shaft. This results in ionization of the surrounding air, effectively reducing its dielectric breakdown voltage. To prevent electrical damage to the magnetic encoder in the case of an electrostatic discharge, a grounding cable is mounted underneath the encoder. The cylinder has a 15 cm diameter and a 45 cm length. The mass of the rotating components is 156.8 g, with a transverse moment of inertia of  $2.867 \text{ g}\cdot\text{m}^2$ .

The 15 cm diameter stationary sphere is located at  $d = 45$  cm from the cylinder, which results in a 15 cm surface to surface separation at a parallel orientation with  $\theta = 0^\circ$ . The entire system is scaled down from the baseline mission configuration in Section 3.3, with the separation distance reduced even further. As such, this system is expected to have a much greater attitude control

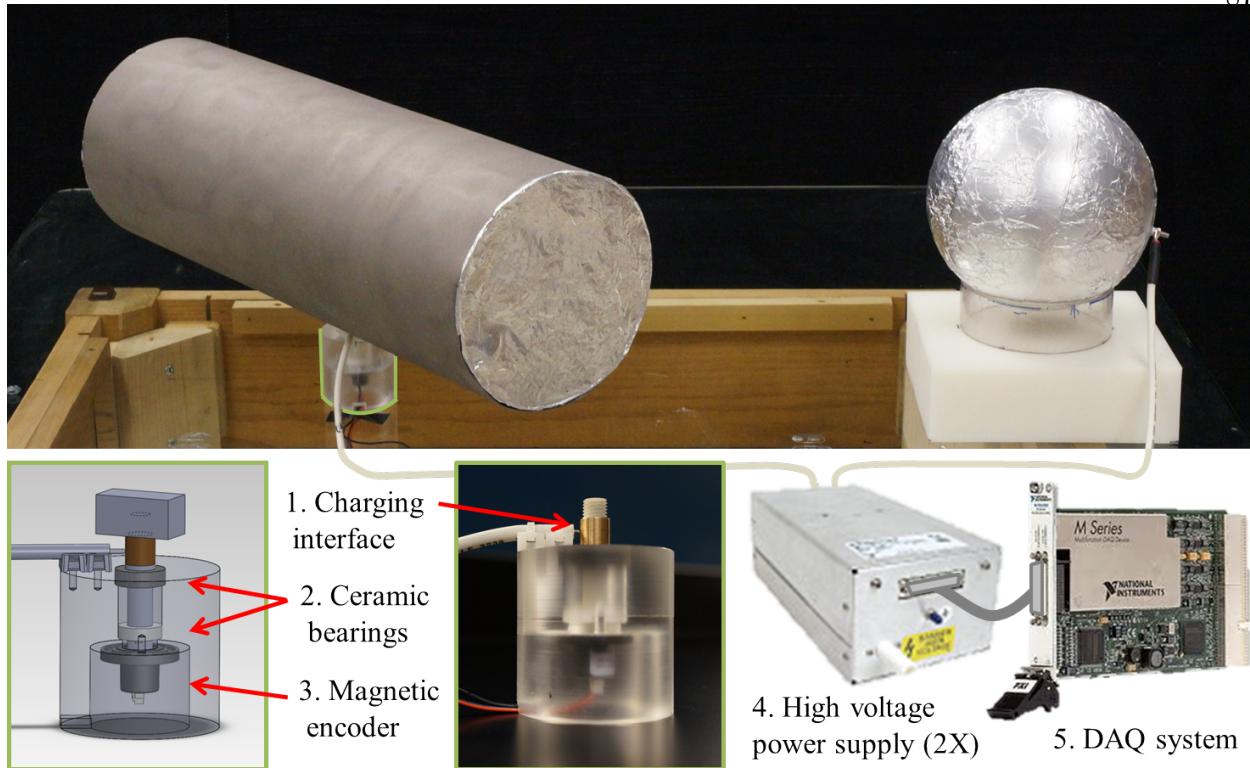


Figure 5.2: Depiction of the experimental setup for charged attitude control

authority than the baseline system. Since the stationary sphere experiences frequent polarity changes, it is charged using the Masusada CZ9-30R power supply, which is capable of an order of magnitude quicker polarity switching than the Spellman, with verified delays lower than 0.1 seconds. Both power supplies are capable of supplying  $\pm 30$  kV at up to  $300 \mu\text{A}$ , which results in power levels well within typical safety limits when proper precaution measures are practiced. To prevent any interaction between the operator and the charged objects, a large plastic cage surrounds the experimental setup.

Input and output control for the power supplies and angular encoder is achieved by a PCI express based 16-Bit multi-channel NI DAQ card. National Instruments LabVIEW software is utilized to monitor and interact with the hardware. Data sampling at 66.66 Hz is achieved, which far exceeds the time constants evident in the dynamics of the system. Differentiation of the cylinder's angular position is performed within LabVIEW using a discrete derivative with switching



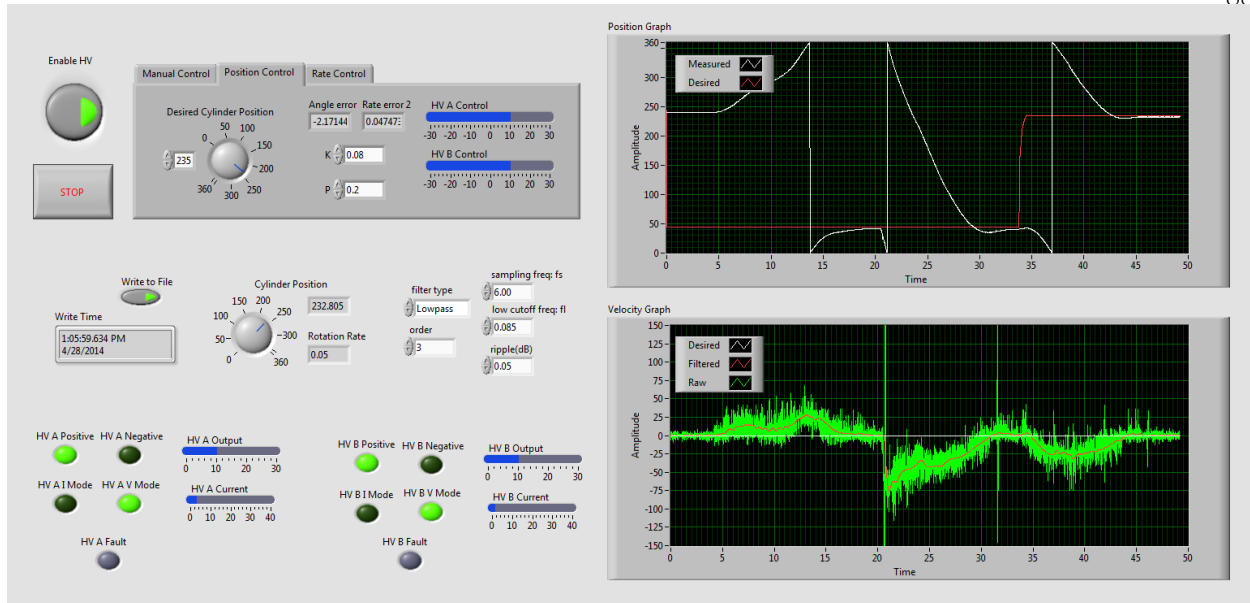


Figure 5.3: Screenshot of the LabVIEW graphical user interface

logic to handle the multiple revolution discontinuity, which is passed through a third order lowpass Chebyshev filter. The custom graphical user interface shown in Fig. 5.3 allows for various operation modes, including manual voltage control, angular position control, and rotation rate control. Table 5.1 identifies the manufacturer and model numbers for all the hardware mentioned above.

Table 5.1: Testbed component details

Contactless charge transfer	HVPS cable and copper bushing
Magnetic encoder	US Digital MAE3 Absolute Encoder
Ceramic bearing	VXB.com ZrO2 8x14x4 & 688 8x16x5 full ceramic sealed bearing
High voltage power supply	Matsusada Precision CZ9-30R
	Spellman Voltage Electronics CZE 2000
DAQ system	National Instruments PXI-6259 data acquisition card
	(2X) NI SCB-68 shielded breakout boxes

### 5.3 Disturbance Characterization

Besides the Coulomb interaction with the sphere, the clearly identifiable disturbances acting on the cylinder as it rotates about its axis are the friction torque from the bearing and the

atmospheric drag force acting on the cylinder surface.

The friction torque  $M_B$  in a rolling bearing is due to a combination of radial forces and axial forces  $F_i$ , the friction coefficient  $\mu_i$  and the average of the bore and outside diameter of the bearing  $\bar{d} = \frac{d_i + d_o}{2}$ , as follows:

$$M_B = \mu_r \frac{\bar{d}}{2} F_r + \mu_a \frac{\bar{d}}{2} F_a \quad (5.1)$$

Since the expected radial force due to the Coulomb interaction with the sphere never exceeds 13.90 mN, whereas the weight of the cylinder and laser disc is equal to a 1.786 N axial force, the radial component can be neglected. If the bearing diameter is incorporated into a new combined bearing friction coefficient  $C_b$ , the total bearing friction is written

$$M_B = C_b F_a \quad (5.2)$$

where  $C_b$  will be determined empirically, because there is no readily available way to isolate the bearing friction torque from other disturbance torques such as atmospheric drag.

For high Reynolds number flows, the drag force  $F_D$  on a body with surface area  $A$  and drag coefficient  $C_d$  moving at velocity  $V$  through a medium with density  $\rho$  is given by

$$F_D = \frac{1}{2} \rho V^2 C_d A \quad (5.3)$$

Consider a cylinder with length  $L$  and diameter  $D$  rotating at angular rate  $\omega = \dot{\theta}$ . A differential slice of width  $dr$  located at a distance  $r$  away from the cylinder axis of rotation experiences a drag force

$$dF_D = \frac{1}{2} \rho (\omega r)^2 C_d (D dr) \quad (5.4)$$

The differential torque from each slice is  $dM = r dF$  and the total torque from both halves of the cylinder due to atmospheric drag is

$$M_D = \rho \omega^2 C_d D \int_0^{L/2} r^3 dr \quad (5.5)$$

$$M_D = \frac{\rho \omega^2 C_d D L^4}{64} \quad (5.6)$$

A typical atmospheric air density  $\rho = 1.194 \text{ kg/m}^3$  is used and  $C_d$  is found to be 1 for an infinite cylinder at mid-range Reynold numbers.<sup>91</sup> The parasitic drag across the two ends of the cylinder must be considered. Since the ends move at  $V = \omega \frac{L}{2}$  relative to the ambient air, this effect can be incorporated into  $C_d$ , which is then determined empirically.

Five sets of data are collected by giving the cylinder an initial rotation and allowing it to de-spin naturally while the electric potential on both the cylinder and the adjacent sphere are held at zero. Fig. 5.4(a) shows the angular rates of the cylinder for each experimental run and a simulated de-spin using the modeled disturbance torques from Eq. (5.2) and (5.6). The corresponding coefficients are tuned until the resultant angular velocity curve optimally fit the experimental data, resulting in  $C_b = 0.000024$  and  $C_d = 0.92$ . Fig. 5.4(b) shows the resulting disturbance torques in the simulation, suggesting that the drag force is dominant at angular rates

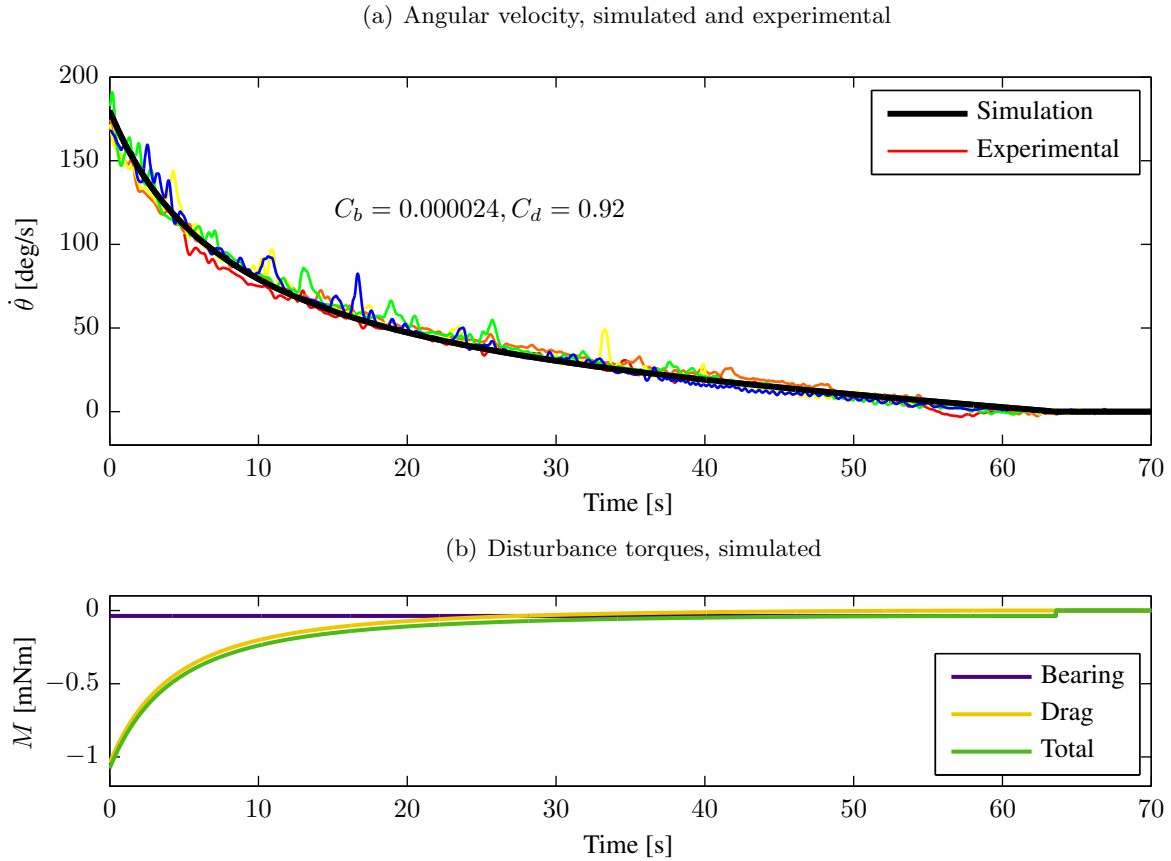


Figure 5.4: Characterization of disturbance torques

higher than 33 deg/s.

## 5.4 Rotation Rate Control

In this development, the goal is to maintain a constant angular rate of rotation on the cylinder  $\dot{\theta}_r$ . The error in rotation rate relative to the reference can be defined  $\delta\dot{\theta} = \dot{\theta} - \dot{\theta}_r$ . This is similar to the development in Section 3.2.2, but here the option of nonzero desired rotation rates is included.

### 5.4.1 Control Development

For the moment, the disturbance forces are omitted from the system dynamics, which take the form

$$I\ddot{\theta} = \gamma f(\phi)g(\theta) \quad (5.7)$$

The following energy based positive definite Lyapunov function is chosen:

$$V(\delta\dot{\theta}) = \frac{I}{2}\delta\dot{\theta}^2 \quad (5.8)$$

The time derivative of this function becomes

$$\dot{V}(\delta\dot{\theta}) = \delta\dot{\theta}(I\ddot{\theta}) \quad (5.9)$$

$$= \delta\dot{\theta}(\gamma f(\phi)g(\theta)) \quad (5.10)$$

where it is assumed  $\ddot{\theta}_r = 0$  and the system dynamics from Eq. 5.7 are used. At this point, a control function  $f(\phi)$  is chosen, which is implemented via the control voltages  $\phi_1 = \phi$  and  $\phi_2 = |\phi|$ . Similar to the developments in Section 3.2.2, the following control is chosen:

$$f(\phi) = -\frac{f_{\max}}{\pi/2} \text{sign}(g(\theta)) \tan^{-1}(P\delta\dot{\theta}) \quad (5.11)$$

The arctangent function is used so that the control voltages are smoothly limited at their saturation levels. The sign of  $g(\theta)$  is included so that the correct polarity voltage control is utilized in any given quadrant. The resulting Lyapunov rate is

$$\dot{V}(\delta\dot{\theta}) = -\frac{\gamma f_{\max}}{\pi/2} |g(\theta)| \delta\dot{\theta} \tan^{-1}(P\delta\dot{\theta}) \quad (5.12)$$

This function is negative semi-definite because  $\tan^{-1}(P\delta\dot{\theta})$  has the same sign as  $\delta\dot{\theta}$ , thus implying global stability to the desired rotation rate. While  $g(\theta)$  can be periodically zero, it is not possible for  $g(\theta)$  to remain zero unless  $\delta\dot{\theta} = 0$  as well. Thus, the largest invariant set where  $\dot{V} = 0$  is  $\delta\dot{\theta} = 0$ , and the system is globally asymptotically stable. Remember that both  $\gamma$  and  $g(\theta)$  take different forms depending on whether attractive or repulsive control is used, but their signs are unaffected.

When the experimental testbed disturbance torques are included in the equations of motion, closed-loop rate tracking errors will only be bounded or Lagrange stable. It is not possible to continually compensate for these arresting torques because the control authority via Coulomb charging vanishes at the four equilibrium points ( $\theta = n\frac{\pi}{4}$ ) during every rotation. When the cylinder reaches these orientations, the rotation speed will decrease until control authority is regained, at which point the control law in Eq. 5.11 will raise the rotation rate to match the desired rate. Freeflying spacecraft will not experience significant rotation torques, lending themselves more readily to these control algorithms.

#### 5.4.2 Experimental Results

The control algorithm in Eq. 5.11 is implemented on the experimental testbed described above, using the gain  $P = 2.0$ . As shown in Fig. 5.5(a), a reference rate  $\dot{\theta}_r = 30$  deg/s is prescribed for the first 54 seconds, at which point the reference is changed to  $\dot{\theta}_r = -60$  deg/s. The results are compared with a numeric simulation conducted in MATLAB which implements the three sphere MSM, including disturbance torques as described above. There is significantly more error in the rotation rate of the experimental system than in the simulation, which is due to the noise in the magnetic angular encoder and the filtering used to determine the resulting rotation rate. In both the physical system and the simulation, it takes about 8 seconds to attain the 30 deg/s rotation rate, and 18 seconds to reverse the rotation and achieve the 60 deg/s rotation rate in the other direction. Fig. 5.5(b) shows the Coulomb and disturbance torques (bearing friction and atmospheric drag) as calculated by the simulation. The Coulomb torques are periodic with angular rotation, and sporadic even in the simulation because of the inconsistent control authority as the cylinder

rotates through the parallel and perpendicular configurations.

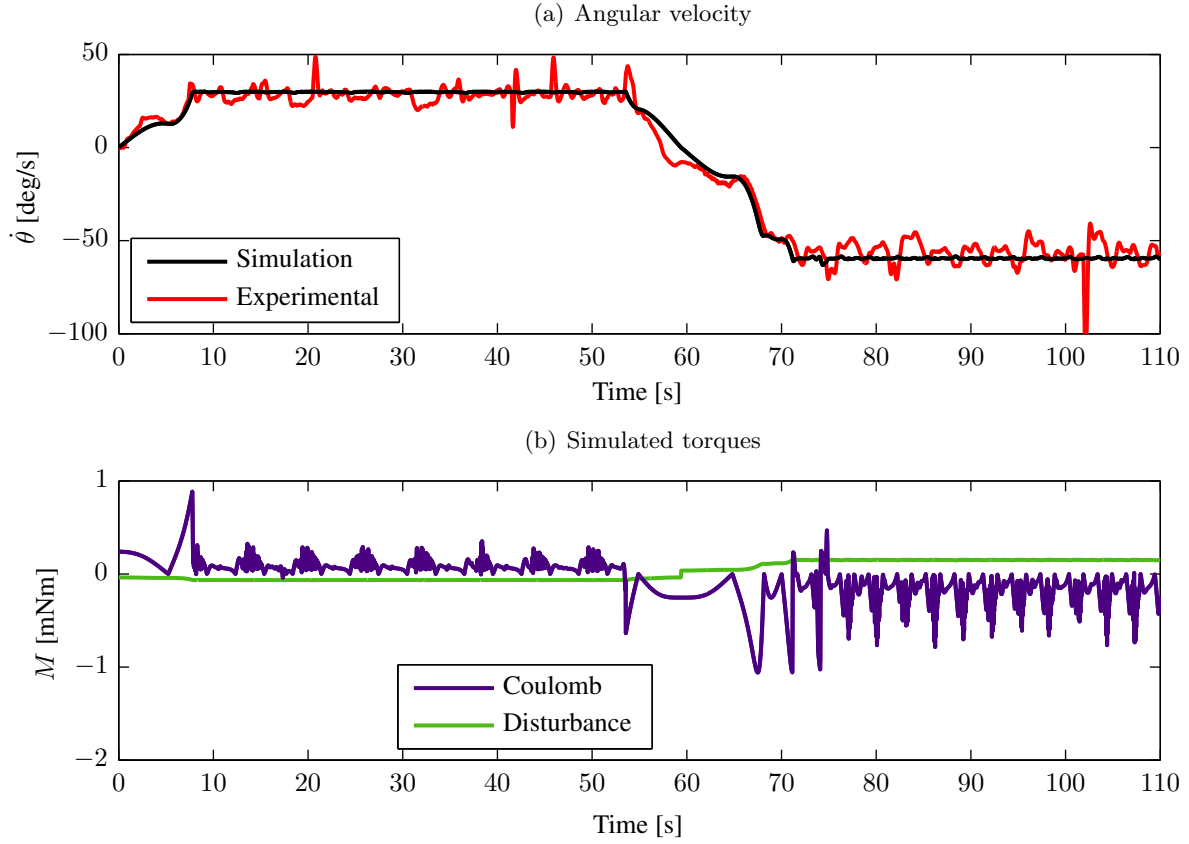


Figure 5.5: Cylinder rotation rate control, experimental and simulation

## 5.5 Attitude Control

Ultimately, the novelty of this testbed is its ability to control the exact attitude of the rotating cylinder. The goal is to track a reference orientation  $\theta_r$ , or minimize the error in angular position  $\delta\theta = \theta - \theta_r$ , which was not considered in Chapter 3. The reference angle is assumed to be constant, i.e.  $\dot{\theta}_r = 0$ .

### 5.5.1 Control Development

The involved nature of the system dynamics that result from the  $g(\theta)$  function complicates the stability control arguments. One possible control algorithm has been identified for which local

nonlinear stability arguments can be made. The proposed Lyapunov function is:

$$V(\dot{\theta}, \delta\theta) = \frac{1}{2}I\dot{\theta}^2 + \frac{K}{2}g^2(\theta)\delta\theta^2 \quad (5.13)$$

This function is positive definite only within a given quadrant, as  $g^2(\theta)$  vanishes at  $\theta = n\frac{\pi}{4}$ . If the electric potentials are chosen such that

$$f(\phi) = -\frac{1}{\gamma} \left( g(\theta)P\dot{\theta} + g(\theta)K\delta\theta + g'(\theta)K\delta\theta^2 \right) \quad (5.14)$$

where  $g'(\theta)$  denotes differentiation with respect to  $\theta$ , the resulting Lyapunov rate is

$$\dot{V}(\dot{\theta}, \delta\theta) = \dot{\theta} \left( I\ddot{\theta} + Kg(\theta)g'(\theta)\delta\theta^2 + Kg^2(\theta)\delta\theta \right) \quad (5.15)$$

$$= -g^2(\theta)P\dot{\theta}^2 \quad (5.16)$$

where several terms cancel when the system dynamics from Eq. 5.7 are included using the control in Eq. 5.14. This Lyapunov rate is negative semi-definite within any quadrant, implying local stability within that quadrant. The same approach can be taken as in Section 3.2.3 however, where the cylinder is allowed to coast without charge control until it reaches the appropriate quadrant, at which point the attitude control described above is implemented.

The control described above has been shown in simulations to converge to the desired reference attitude, but it is impractical for physical implementation because it requires exact knowledge of the higher order  $g$  function as well as its angle derivative. It is preferable to use a control based only on the sign of  $g$ , which is readily known for a given quadrant. Moreover, better time performance is provided using a control law of the following form, where  $K$  and  $P$  are chosen to be positive gains.

$$f(\phi) = -\frac{f_{\max}}{\pi/2} \text{sign}(g(\theta)) \tan^{-1} \left[ P\delta\dot{\theta} + K\delta\theta \right] \quad (5.17)$$

The arctangent function is again chosen so that control voltages are smoothly limited to their maximum levels without abrupt saturation. While it is difficult to make Lyapunov stability arguments regarding this nonlinear control, we can analyze the closed loop dynamics, which take the form

$$I\ddot{\theta} = -\frac{\gamma f_{\max}}{\pi/2} |g(\theta)| \tan^{-1} \left[ P\delta\dot{\theta} + K\delta\theta \right] \quad (5.18)$$

If we make the assumption that the reference trajectory is to maintain a constant orientation, i.e.  $\dot{\theta}_r = 0$ , the closed loop dynamics can be linearized about the reference angle  $\theta_r$  as follows:

$$\delta\ddot{\theta} + \beta P \delta\dot{\theta} + \beta K \delta\theta = 0 \quad (5.19)$$

where

$$\beta = \frac{\gamma f_{\max} |g(\theta_r)|}{(\pi/2)I} \quad (5.20)$$

Note that both  $\gamma$  and  $|g(\theta_r)|$  take different forms depending on whether the system is in an electrostatically attractive or repulsive state. Their signs remain unchanged however, and  $\beta$  is always a positive coefficient. Therefore, the roots of this second order differential equation always have negative real components, and the system is assumed to be locally stable in the linearized neighborhood of the reference angle. The natural frequency  $\omega_n$  and damping coefficient  $\zeta$  in this vicinity are

$$\omega_n = \sqrt{\beta K} \quad (5.21)$$

$$\zeta = \frac{P}{2} \sqrt{\frac{\beta}{K}} \quad (5.22)$$

Because  $\beta$  changes depending on the voltage polarities, the system will have different closed-loop response characteristics (stiffness, damping, etc.) depending on from which direction the cylinder approaches the reference orientation. Linear stability is guaranteed in either case.

### 5.5.2 Experimental Results

The results in Fig. 5.6 demonstrate the ability to prescribe a specific angular orientation on the rotating cylinder using Coulomb actuation. The cylinder is given an initial rotation rate of 100 deg/s, at which point the charge control algorithm in Eq. 5.17 is implemented via the high voltage power supplies. A reference angle of  $\theta_r = 45$  deg is prescribed while the gains are set to  $K = 0.08$  and  $P = 0.2$ . Within 10 seconds the cylinder is brought to rest, and after a slight overshoot, the desired reference angle is achieved to within 1.5 deg. From Fig. 5.4(a) it can be seen that it takes 60 seconds for the cylinder to come to rest from this rotation rate by disturbance torques alone. As is



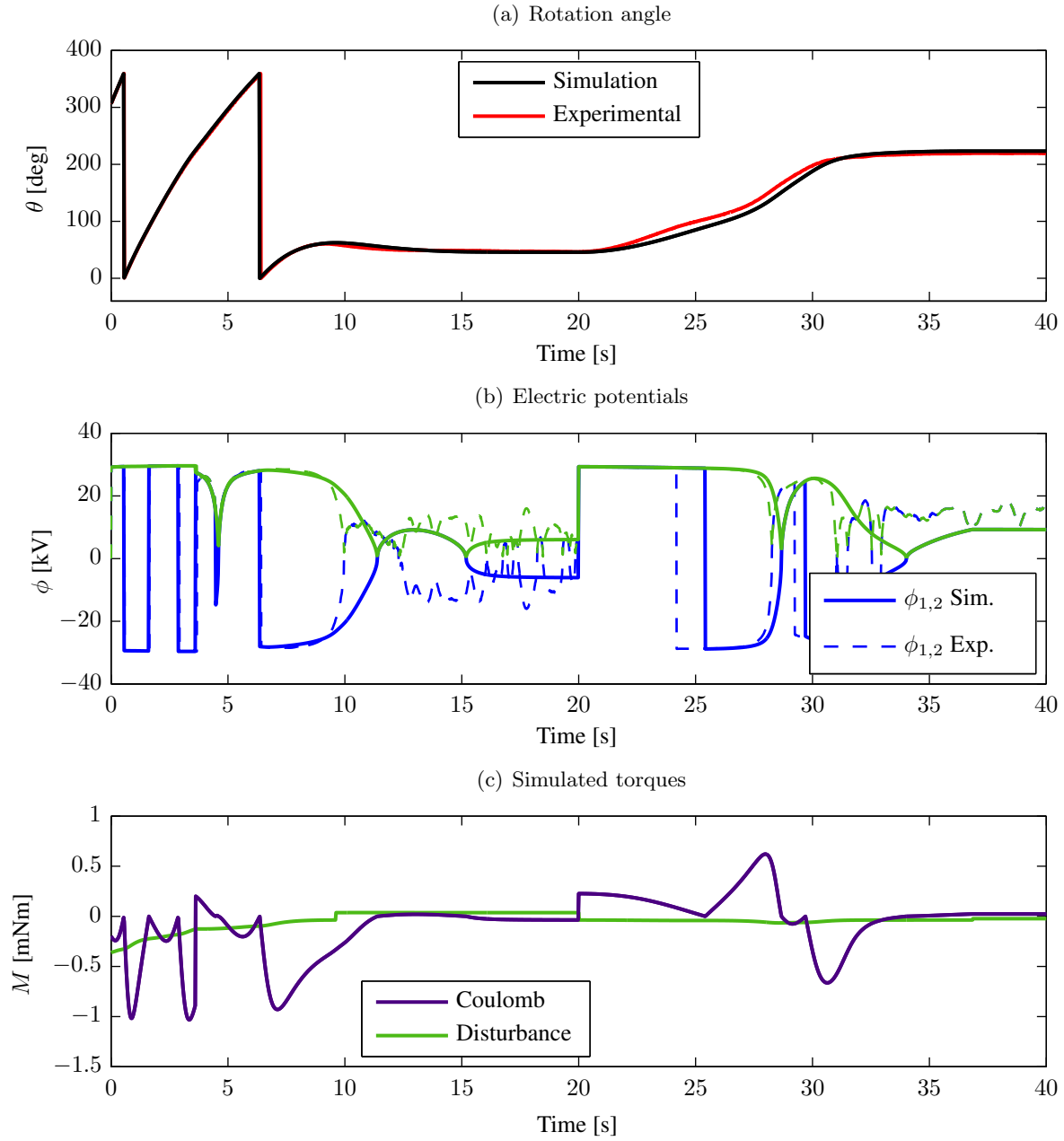


Figure 5.6: Cylinder attitude control: experimental and simulation

evident from Fig. 5.6(a), the simulation conducted using MATLAB matches the experimental results with formidable accuracy. This simulation implements the full system dynamics using the three sphere MSM, including disturbance torques from bearing and atmospheric drag. Fig. 5.6(b) depicts the prescribed electric potentials, where blue denotes the sphere voltage  $\phi_1$  and green denotes the cylinder voltage  $\phi_2$ . Here a slight deviation is evident between the simulation and experiment when

the cylinder comes to rest, which is likely the result of sensor noise at low velocities.

At 20 seconds into the simulation, the reference angle is changed to 225 deg, representing a 180 deg switch in the desired angle. Within 12 seconds the target orientation is achieved, this time with a 5.5 deg attitude error. This is because the reference angle is approached from the direction where repulsive control is required to remove the remaining error, which produces lower torques than the attractive configuration (as seen in Fig. 3.2) that are unable to overcome the bearing friction. The simulation demonstrates a lower error of 2 deg, suggesting there is some unmodeled stiction present in the ceramic bearings. Fig. 5.6(c) displays the friction and Coulomb torques calculated in the simulation, which suggests a maximum Coulomb torque of roughly 1 mNm, which matches well with the expected torques predicted by the MSM.

The terrestrial testbed described in this chapter is an extremely important tool in verifying the electrostatic de-spin concept. Using only Coulomb interaction, the system is able to swiftly bring the cylinder to rest from a large rotation rate, and position it in a desired angular orientation. Hereby, both the electrostatic models developed in Chapter 2, and the expected system dynamics including control algorithms derived in Chapter 3 are validated.

## Chapter 6

### Conclusion

#### 6.1 Dissertation Summary

This dissertation addresses various aspects of remote spacecraft attitude control by Coulomb charging. The goal is to remove rotational kinetic energy from an uncontrolled space object with a nearby servicing spacecraft, without making contact. This operation is to be carried out prior to conducting a physical rendezvous with the derelict satellite in order to reposition or service it. Such a mission involves a multitude of challenges. The servicing craft must establish large electrostatic potentials on both vehicles. The magnitude and polarity of the voltages depends on the orientation of the rotating debris craft, so that the resulting electrostatic torques serve to arrest the rotation of the object.

The first task is to model the electrostatic interaction between the charged three dimensional spacecraft. Conventional high fidelity models are too time intensive to use for 6DOF simulations, while sphere and point charge models are incapable of discerning Coulomb torques. A new approach named the Multi-Sphere Method (MSM) is herein developed to predict the electrostatic interaction in a computationally efficient way. Spheres are placed within the volume or along the surface of a conducting geometry, and the charge on each sphere is determined according to their position dependent capacitance, from which Coulomb forces and torques can be derived. This model is rigorously compared to higher order FEA software, thereby validating its use for predicting the electrostatics of the satellite de-spin concept. Even the simplified model predicts the electrostatic torque to within a percent at the separation distances expected in operation.

In order to validate various aspects of this technology, a simplified system is introduced whereby a spherical servicing craft attempts to remove the 1-D rotation about the minor axis of a spinning cylinder debris object. Analytic expressions for the torque exerted on the cylinder aid in creating nonlinear control algorithms to arrest the cylinder rotation. Lyapunov theory is utilized to determine the stability of various control laws, including those where Coulomb interaction is used to exert nominal tugging forces on the debris object. A baseline simulation indicates that a 12 deg/s rotation on the cylinder can be removed in roughly 3 days with reasonable system parameters. The sensitivity of the performance to various changes in size and separation distance is also investigated. Several approaches to optimizing the performance are identified, including relative position and attitude control schemes to be executed by the servicing craft. Lastly, the physical hardware necessary to achieve the desired potential levels is investigated. The servicing craft requires both an electron and an ion gun, but charge up and polarity switching procedures occur in roughly a tenth of a second, with no significant instabilities.

Besides theoretical analysis and computer simulations, the electrostatic detumble concept is verified experimentally. A scaled down version of the cylinder sphere system is created with physically conducting shapes in the laboratory. The cylinder is free to rotate with minimal disturbance torques, and the potential on both shapes is actively controlled using high voltage power supplies. Using control algorithms similar to those developed earlier, the testbed is capable of achieving rotation rate control and absolute attitude control on the cylinder. A 100 deg/s rotation is arrested in roughly 10 seconds, while the desired attitude is matched within 1.5 deg. This experimental validation along with the extensive system simulation performed represents a significant stride towards realization of the remote Coulomb attitude control concept.

## 6.2 Suggestions for Future Work

The electrostatic attitude control concept has progressed within this research effort from its inception to a 3-4 Technology Readiness Level (TRL).<sup>48</sup> All aspects of the system have been examined via first principles, and most key elements are analytically explored in further detail. Several

components of the technology have been integrated for experimental validation in a laboratory environment. While feasibility of the concept has matured significantly, the remaining path to successful implementation of a Coulomb de-spin mission is considerable.

The logical next step in the progression of this research is to expand the dynamics and control analysis to three dimensions. While the MSM and dynamics simulations presented in this dissertation are capable of full dimensionality, the control analysis so far has been limited to a single dimension. Reference 6 expands the motion of the cylinder-sphere system to three dimensions and proves that the 1-D tumble considered before can still be removed. Arresting any rotation in the plane perpendicular to the control craft position, however, would require relocation of the control craft. Meanwhile, the control authority to arrest a spin about the axis of symmetry of the debris object is questionable. This might be achieved by first inducing a nutating motion on the object, at which point some control authority is restored, but requires further investigation. Lastly, the complexity of the charge control requirements is dependent on the geometry of the spacecraft being considered for de-spin operations, so various shapes with features that differ from the simple cylinder should be considered.

The relative motion simulations performed in this dissertation have assumed deep space conditions. To improve the fidelity of this analysis in preparation for on-orbit mission implementation, the orbital relative motion dynamics must be considered. This will affect the station-keeping requirements for the servicing craft, but certain natural relative orbits may be utilized to aid with desired position control schemes. Furthermore, the experimental testbed may be expanded to additional dimensions to validate the relative motion dynamics and study the interaction of Coulomb forces and torques. This could be done by combining the current rotational setup with the linear air bearing testbed previously created in the AVS lab, or with a new design that allows planar motion on an air bearing slab. Integrating frictionless motion with high voltage capabilities presents a serious challenge for this approach, but might be achieved with self-contained vehicles.

Thus far, the analysis of the charge transfer devices required to achieve desired voltage levels on the satellites in the system contains inherent approximations. The assumptions and

simplifications must be verified using higher fidelity particle-in-cell plasma simulations. Moreover, the performance of charged beams and interaction with various material surfaces should be tested experimentally in vacuum chambers that replicate the space plasma environment. This approach could culminate in a test campaign that includes relative motion along with active charge control of the bodies within the vacuum environment. Incorporating all these aspects inside the vacuum chamber while mitigating electrostatic interference between the charged objects and the conducting chamber walls presents a considerable challenge.

Ultimately, on-orbit technology demonstration presents the best validation of the system concepts required for electrostatic de-spin operations. With the miniaturization of components and increasing use of Commercial Off The Shelf (COTS) hardware for space applications, it may be possible to test certain aspects of the technology in the GEO environment with low cost satellites such as CubeSats.<sup>24</sup> In order to apply the appropriate Coulomb charging and position control algorithms, the servicing spacecraft will require an expansive suite of sensing instruments. Besides accurate knowledge of the geometry and material composition of the uncontrolled spacecraft, the servicer must be able to sense its relative position and orientation. This would require robust visual algorithms, or more complex sensors such as radar, LIDAR, or structured light. Moreover, real time knowledge of the potential levels on both craft must be measured by Langmuir probes or electrostatic analyzers. The hardware requirements of these sensors has to be determined, and interference with the high voltage environment must be characterized.

Many of the tasks proposed above can be performed in a university laboratory setting, but eventually progress will be driven by financial support. When the severity of satellite conjunctions in GEO reaches critical levels, the funding for on-orbit validation missions may well be provided by government agencies. It is in the best interest of the entire aerospace engineering community to develop technologies such as remote Coulomb attitude control to combat the escalation of the GEO debris population.

## Bibliography

- [1] Paul V. Anderson and Hanspeter Schaub. Local orbital debris flux study in the geostationary ring. Advances in Space Research, 51(12):2195–2206, 2013.
- [2] Paul V. Anderson and Hanspeter Schaub. Local debris congestion in the geosynchronous environment with population augmentation. Acta Astronautica, 94(2):619–628, Feb. 2014.
- [3] L Anselmo and C Pardini. Space debris mitigation in geosynchronous orbit. Advances in Space Research, 41(7):1091–1099, 2008.
- [4] Brent W Barbee, Salvatore Alfano, Elfego Pinon, Kenn Gold, and David Gaylor. Design of spacecraft missions to remove multiple orbital debris objects. In Aerospace Conference, 2011 IEEE, pages 1–14. IEEE, 2011.
- [5] Robert Bauer. Distribution of points on a sphere with application to star catalogs. Journal of Guidance, Control, and Dynamics, 23(1):130–137, 2000.
- [6] Trevor Bennett and Hanspeter Schaub. Touchless electrostatic three-dimensional detumbling of large geo debris. In AAS/AIAA Spaceflight Mechanics Meeting, Santa Fe, New Mexico, Jan. 26–30 2014. Paper AAS 14-378.
- [7] Trevor Bennett, Daan Stevenson, Erik Hogan, Lauren McManus, and Hanspeter Schaub. Prospects and challenges of touchless debris despinning using electrostatics. In 3rd European Workshop on Space Debris Modeling and Remediation, CNES, Paris, June 16–18 2014. Paper #P8.
- [8] Dennis S Bernstein, N Harris McClamroch, and Anthony Bloch. Development of air spindle and triaxial air bearing testbeds for spacecraft dynamics and control experiments. In American Control Conference, 2001. Proceedings of the 2001, volume 5, pages 3967–3972. IEEE, 2001.
- [9] John Berryman and Hanspeter Schaub. Analytical charge analysis for 2- and 3-craft coulomb formations. AIAA Journal of Guidance, Control, and Dynamics, 30(6):1701–1710, Nov.–Dec. 2007.
- [10] Claudio Bombardelli and Jesus Pelaez. Ion beam shepherd for contactless space debris removal. AIAA Journal of Guidance, Control, and Dynamics, 34(3):916–920, May–June 2011.
- [11] Claudio Bombardelli, Hodei Urrutxua, Mario Merino, Eduardo Ahedo, Jesús Peláez, and Joris Olympio. Dynamics of ion-beam-propelled space debris. In 22nd Symposium (International) on Space Flight Dynamics. Available online at [web.fmetisia.upm.es/ep2](http://web.fmetisia.upm.es/ep2), 2011.

- [12] Christophe Bonnal, Jean-Marc Ruault, and Marie-Christine Desjean. Active debris removal: Recent progress and current trends. Acta Astronautica, 85:51–60, 2013.
- [13] C.A. Brebbia. The boundary element method for engineers. Pentech Press, 1978.
- [14] Richard. P. Brent. Algorithms for Minimization without Derivatives. Prentice-Hall, Englewood Cliffs, New Jersey, 1973.
- [15] J.R. Brophy, L. Friedman, and F. Culick. Asteroid retrieval feasibility. In Aerospace Conference, 2012 IEEE, pages 1–16, March 2012.
- [16] Mengu Cho, Raju Ramasamy, Toshiaki Matsumoto, Kazuhiro Toyoda, Yukishige Nozaki, and Masato Takahashi. Laboratory tests on 110-volt solar arrays in simulated geosynchronous orbit environment. Journal of spacecraft and rockets, 40(2):211–220, 2003.
- [17] Philip Chrystal, Darren McKnight, P Meredith, Jan Schmidt, Marcel Fok, and Charles Wetton. Space debris: on collision course for insurers. Swiss Reinsurance Co. Publ., Zurich, Switzerland, March, 2011.
- [18] Patrice Couzin, Frank Teti, and Richard Rembala. Active removal of large debris : Rendez-vous and robotic capture issues. In 2nd European Workshop on Active Debris Removal, Paris, France, 2012. Paper #7.5.
- [19] V.A. Davis and M.J. Mandell. Plasma interactions with spacecraft, vol. ii. Technical report, AFRL, April 2011. NASCAP-2K Scientific Documentation for Version 4.1.
- [20] LT DeLuca, F Bernelli, F Maggi, P Tadini, C Pardini, L Anselmo, M Grassi, D Pavarin, A Francesconi, F Branz, et al. Active space debris removal by a hybrid propulsion module. Acta Astronautica, 91:20–33, 2013.
- [21] M. H. Denton, M. F. Thomsen, H. Korth, S. Lynch, J. C. Zhang, and M. W. Liemohn. Bulk plasma properties at geosynchronous orbit. Journal of Geophysical Research, 110(A7), 07 2005.
- [22] BT Draine and EE Salpeter. On the physics of dust grains in hot gas. The Astrophysical Journal, 231:77–94, 1979.
- [23] W. H. DuMouchel and F. L. O’Brien. Integrating a robust option into a multiple regression computing environment. In Computer Science and Statistics: Proceedings of the 21st Symposium on the Interface, Alexandria, VA, 1989. American Statistical Association. Manuscript.
- [24] Matthew T Erdner. Smaller satellite operations near geostationary orbit. PhD thesis, Monterey, California. Naval Postgraduate School, 2007.
- [25] M. A. Malcolm Forsythe, G. E. and C. B. Moler. Computer Methods for Mathematical Computations. Prentice-Hall, 1976.
- [26] Daniele Gallardo, Riccardo Bevilacqua, and Richard E Rasmussen. Advances on a 6 degrees of freedom testbed for autonomous satellites operations. In AIAA Guidance, Dynamics and Control Conference, 2011.



- [27] Walton C. Gibson. The Method of Moments in Electromagnetics. Chapman and Hall/CRC, 1st edition, 2007.
- [28] Roger F. Harrington. Matrix methods for field problems. Proc. IEEE, 55(2):136–149, 1967.
- [29] Erik Hogan and Hanspeter Schaub. Relative motion control for two-spacecraft electrostatic orbit corrections. In AAS/AIAA Spaceflight Mechanics Meeting, Girdwood, Alaska, July 31 – August 4 2011. Paper AAS 11–466.
- [30] Erik Hogan and Hanspeter Schaub. Collinear invariant shapes for three-craft coulomb formations. Acta Astronautica, 12:78–89, March–April 2012.
- [31] Erik Hogan and Hanspeter Schaub. Space debris reorbiting using electrostatic actuation. In AAS Guidance and Control Conference, Breckenridge, CO, Feb. 3–8 2012. Paper AAS 12–016.
- [32] Erik A. Hogan and Hanspeter Schaub. Impacts of solar storm events and ion beam emission on electrostatic tractor performance. In 13th Spacecraft Charging Technology Conference, Pasadena, CA, June 23–27 2014.
- [33] Erik A. Hogan and Hanspeter Schaub. Impacts of tug and debris sizes on electrostatic tractor charging performance. In International High Power Laser Ablation and Beamed Energy Propulsion, Santa Fe, New Mexico, April 21–25 2014.
- [34] P.W. Holland and R.E. Welsch. Robust regression using iteratively reweighted least-squares. Communications in Statistics: Theory and Methods, (A6):813–827, 1977.
- [35] Lee E. Z. Jasper and Hanspeter Schaub. Effective sphere modeling for electrostatic forces on a three-dimensional spacecraft shape. In AAS/AIAA Spaceflight Mechanics Meeting, Girdwood, Alaska, July 31 – August 4 2011. Paper AAS 11–465.
- [36] J.L. Junkins. Optimal Estimation of Dynamical Systems. Sijthoff-Noordhoff, 1st edition, 1978.
- [37] Yu S. Karavaev, R. M Kopyatkevich, M. N. Mishina, G. S. Mishin, P. G. Papushev, and P. N. Shaburov. The dynamic properties of rotation and optical characteristics of space debris at geostationary orbit. In Advances in the Astronautical Sciences, volume 119, pages 1457–1466, 2004. Paper No. AAS-04-192.
- [38] TS Kelso. Analysis of the 2007 chinese asat test and the impact of its debris on the space environment. In 8th Advanced Maui Optical and Space Surveillance Technologies Conference, Maui, HI, 2007.
- [39] Donald J Kessler and Burton G Cour-Palais. Collision frequency of artificial satellites: The creation of a debris belt. Journal of Geophysical Research: Space Physics (1978–2012), 83(A6):2637–2646, 1978.
- [40] Hassan K. Khalil. Nonlinear Systems. Prentice-Hall, Inc., Upper Saddle River, NJ, 3rd edition, 2002.
- [41] Lyon B. King, Gordon G. Parker, Satwik Deshmukh, and Jer-Hong Chong. Spacecraft formation-flying using inter-vehicle coulomb forces. Technical report, NASA/NIAC, January 2002.

- [42] Lyon B. King, Gordon G. Parker, Satwik Deshmukh, and Jer-Hong Chong. Study of inter-spacecraft coulomb forces and implications for formation flying. AIAA Journal of Propulsion and Power, 19(3):497–505, May–June 2003.
- [43] Shoji Kitamura, Yukio Hayakawa, Kumi Nitta, Satomi Kawamoto, and Yasushi Ohkawa. A reorbiter for large geo debris objects using ion beam irradiation. In 63rd International Astronautical Congress, Naples, Italy, 2012. Paper No. IAC-12-A6.7.10.
- [44] Heiner Klinkrad. Space debris. Wiley Online Library, 2010.
- [45] Shu T Lai. An improved langmuir probe formula for modeling satellite interactions with near-geostationary environment. Journal of Geophysical Research: Space Physics (1978–2012), 99(A1):459–467, 1994.
- [46] Shu T Lai. Fundamentals of Spacecraft Charging: Spacecraft Interactions with Space Plasmas. Princeton University Press, 2011.
- [47] J-C Liou and Nicholas L Johnson. A sensitivity study of the effectiveness of active debris removal in leo. Acta Astronautica, 64(2):236–243, 2009.
- [48] John C Mankins. Technology readiness levels. White Paper, April, 6, 1995.
- [49] E. G. Mullen, M. S. Gussenhoven, D. A. Hardy, T. A. Aggson, B. G. Ledley, and E. Whipple. Scatha survey of high-level spacecraft charging in sunlight. Journal of Geophysical Research: Space Physics, 91(A2):1474–1490, 1986.
- [50] Arun Natarajan and Hanspeter Schaub. Linear dynamics and stability analysis of a coulomb tether formation. Journal of Guidance, Control, and Dynamics, 29(4):831–839, July–Aug. 2006.
- [51] Andrew Ogilvie, Justin Allport, Michael Hannah, and John Lymer. Autonomous satellite servicing using the orbital express demonstration manipulator system. In Proc. of the 9th International Symposium on Artificial Intelligence, Robotics and Automation in Space (i-SAIRAS’08), pages 25–29, 2008.
- [52] RC Olsen. Experiments in charge control at geosynchronous orbit- ats-5 and ats-6. Journal of Spacecraft and Rockets, 22(3):254–264, 1985.
- [53] N. Ortiz Gómez and S. J. I. Walker. Eddy Currents applied to de-tumbling of space debris: feasibility analysis, design and optimization aspects. In 40th COSPAR Scientific Assembly. Held 2-10 August 2014, in Moscow, Russia, Abstract PEDAS.1-30-14., volume 40 of COSPAR Meeting, 2014.
- [54] P. Papishev, Yu. Karavaev, and M. Mishina. Investigations of the evolution of optical characteristics and dynamics of proper rotation of uncontrolled geostationary artificial satellites. Advances in Space Research, 43(9):1416 – 1422, 2009.
- [55] Gordon G. Parker, Chris E. Passerello, and Hanspeter Schaub. Static formation control using interspacecraft coulomb forces. In 2nd International Symposium on Formation Flying Missions and Technologies, Washington D.C., Sept. 14–16, 2004 2004.

- [56] Jerome Pearson, J Carroll, E Levin, and J Oldson. Active debris removal: Edde, the electrodynamic debris eliminator. In Proceedings of 61st International Astronautical Congress. Prague: IAC, 2010.
- [57] Louis E Perna, Fernando Mier Hicks, Chase S Coffman, Hanqing Li, and Paulo Lozano. Progress toward demonstration of remote, autonomous attitude control of a cubesat using ion electrospray propulsion systems. In Joint Propulsion Conference, Atlanta, 2012.
- [58] Vincent L Pisacane. The space environment and its effects on space systems. American Institute of aeronautics and Astronautics, 2008.
- [59] Carolyn K Purvis, Henry B Garrett, AC Whittlesey, and N John Stevens. Design guidelines for assessing and controlling spacecraft charging effects. 1984.
- [60] J Reed, J Busquets, and C White. Grappling system for capturing heavy space debris. In 2nd European Workshop on Active Debris Removal, 2012.
- [61] Martin W Regehr, Ahmet B Acikmese, Asif Ahmed, MiMi Aung, KC Clark, P MacNeal, J Shields, G Singh, R Bailey, C Bushnell, et al. The formation control testbed. In Aerospace Conference, 2004. Proceedings. 2004 IEEE, volume 1. IEEE, 2004.
- [62] Benjamin Z Reinhardt, Mason Peck, and Brandon Hency. Development of an eddy-current actuator test bed.
- [63] Richard Rembala, Frank Teti, and Patrice Couzin. Operations concept for the robotic capture of large orbital debris. In 35th Annual AAS Guidance & Control Conference, Breckenridge, Colorado, February 3–8 2012. AAS. Paper No. AAS 12-018.
- [64] I Retat, B Bischof, et al. Net capture system: a potential orbital space debris removal system. In 2nd European Workshop on Active Debris Removal, CNES Headquarters, Paris, France, 2012.
- [65] PA Robinson Jr and P Coakley. Spacecraft charging-progress in the study of dielectrics and plasmas. Electrical Insulation, IEEE Transactions on, 27(5):944–960, 1992.
- [66] Michael C Roggemann, Kris Hamada, Kim Luu, Venkata S Rao-Gudimetla, Randy F Cortez, L William Bradford, David C Thompson, and Robert Shirey. Three-dimensional imaging and satellite attitude estimation using pulse laser illumination and a remote ultra-low light imaging (rulli) sensor for space situational awareness (ssa). Technical report, DTIC Document, 2008.
- [67] Hanspeter Schaub. Stabilization of satellite motion relative to a coulomb spacecraft formation. Journal of Guidance, Control and Dynamics, 28(6):1231–1239, Nov.–Dec. 2005.
- [68] Hanspeter Schaub, Christopher Hall, and John Berryman. Necessary conditions for circularly-restricted static coulomb formations. Journal of the Astronautical Sciences, 54(3–4):525–541, July-Dec. 2006.
- [69] Hanspeter Schaub and Lee E. Z. Jasper. Circular orbit radius control using electrostatic actuation for 2-craft configurations. In AAS/AIAA Astrodynamics Specialist Conference, Girdwood, Alaska, July 31 – August 4 2011. Paper AAS 11-498.

- [70] Hanspeter Schaub and Lee E. Z. Jasper. Orbit boosting maneuvers for two-craft coulomb formations. AIAA Journal of Guidance, Control, and Dynamics, 36(1):74–82, Jan. – Feb. 2013.
- [71] Hanspeter Schaub and John L. Junkins. Analytical Mechanics of Space Systems. AIAA Education Series, Reston, VA, 3rd edition, 2014.
- [72] Hanspeter Schaub and Daniel F. Moorer. Geosynchronous large debris reorbiter: Challenges and prospects. In AAS Kyle T. Alfriend Astrodynamics Symposium, Monterey, CA, May 17–19 2010. Paper No. AAS 10-311.
- [73] Hanspeter Schaub, Gordon G. Parker, and Lyon B. King. Challenges and prospect of coulomb formations. Journal of the Astronautical Sciences, 52(1–2):169–193, Jan.–June 2004.
- [74] Hanspeter Schaub and Zolt'an Sternovsky. Active space debris charging for contactless electrostatic disposal maneuvers. Advances in Space Research, 43(1):110–118, 2014.
- [75] Jana L Schwartz and Christopher D Hall. The distributed spacecraft attitude control system simulator: development, progress, plans. In NASA Space Flight Mechanics Symposium, Greenbelt, MD. Citeseer, 2003.
- [76] Jana L Schwartz, Mason A Peck, and Christopher D Hall. Historical review of air-bearing spacecraft simulators. Journal of Guidance, Control, and Dynamics, 26(4):513–522, 2003.
- [77] Raymond Serway and John Jewett. Principles of physics: a calculus-based text, volume 2. Cengage Learning, 2012.
- [78] Carl Seubert. One-dimensional spacecraft formation flight testbed for terrestrial charged relative motion experiments. 2011.
- [79] Carl R. Seubert, Stephan Panosian, and Hanspeter Schaub. Analysis of a tethered coulomb structure applied to close proximity situational awareness. AIAA Journal of Spacecraft and Rockets, 49(6):1183–1193, Nov. – Dec. 2012.
- [80] Carl R. Seubert and Hanspeter Schaub. Closed-loop one-dimensional charged relative motion experiments simulating constrained orbital motion. In AAS/AIAA Astrodynamics Specialist Conference, Pittsburgh, PA, Aug. 9–13 2009. Manuscript.
- [81] Carl R. Seubert and Hanspeter Schaub. Electrostatic force model for terrestrial experiments on the coulomb testbed. In 61st International Astronautical Congress, Prague, CZ, Sept. 2010. International Astronautical Federation. Paper IAC-10.C1.1.9.
- [82] CR Seubert and H Schaub. One-dimensional testbed for coulomb controlled spacecraft. In AAS/AIAA Spaceflight Mechanics Meeting, Savannah, GA, pages 09–015, 2009.
- [83] Lt Col Glen Shepherd and Air Force Space Command. Space surveillance network. In Shared Space Situational Awareness Conference, Colorado Sprincs, CO, 2006.
- [84] Josip Sliško and Raúl A. Brito-Orta. On approximate formulas for the electrostatic force between two conducting spheres. American Journal of Physics, 66(4):352–355, 1998.
- [85] W. R. Smythe. Static and Dynamic Electricity. McGraw–Hill, 3rd edition, 1968.

- [86] Jack A. Soules. Precise calculation of the electrostatic force between charged spheres including induction effects. American Journal of Physics, 58(12):1195–1199, 1990.
- [87] Daan Stevenson and Hanspeter Schaub. Terrestrial testbed for remote coulomb spacecraft rotation control. International Journal of Space Science and Engineering, 2(1):96–112, 2014.
- [88] Laura A. Stiles, Hanspeter Schaub, Kurt K. Maute, and Daniel F. Moorer. Electrostatically inflated gossamer space structure voltage requirements due to orbital perturbations. Acta Astronautica, 84:109–121, Mar.–Apr. 2013.
- [89] Fumihito Sugai, Satoko Abiko, Teppei Tsujita, Xin Jiang, and Masaru Uchiyama. Detumbling an uncontrolled satellite with contactless force by using an eddy current brake. In IROS’13, pages 783–788, 2013.
- [90] Alan C. Tribble. The Space Environment - Implications for Spacecraft Design. Princeton University Press, revised and expanded edition, 2003.
- [91] D.J. Tritton. Physical Fluid Dynamics. Oxford Science Publications. Clarendon Press, 1988.
- [92] Harsh Vasavada and Hanspeter Schaub. Analytic solutions for equal mass four-craft static coulomb formation. Journal of the Astronautical Sciences, 56(1):17–40, Jan. – March 2008.
- [93] Ting Wang. Analysis of debris from the collision of the cosmos 2251 and the iridium 33 satellites. Science & Global Security, 18(2):87–118, 2010.
- [94] CL Waters, JC Samson, and EF Donovan. Variation of plasmatrough density derived from magnetospheric field line resonances. Journal of Geophysical Research: Space Physics (1978–2012), 101(A11):24737–24745, 1996.
- [95] Elden C Whipple. Potentials of surfaces in space. Reports on Progress in Physics, 44(11):1197, 1981.
- [96] Wenfu Xu, Bin Liang, Bing Li, and Yangsheng Xu. A universal on-orbit servicing system used in the geostationary orbit. Advances in Space Research, 48(1):95–119, 2011.

## Appendix A

### Coulomb Force Determination by Sensing

Because there exists an inherent relation between surface charge density and the local external electric field, discretized knowledge of either quantity is sufficient to discern the electrostatic forces acting on a body. If either of these quantities can be measure along the surface of a spacecraft, the complete Coulomb mechanics can be constructed without knowledge of neighboring objects and surrounding electrostatic fields.

Consider the Gaussian surface on a conductor in Figure A.1. The electric field adjacent to the surface is known to be perpendicular, because any orthogonal component would rearrange the charge distribution until the field is perpendicular. Moreover, the electric field inside the conductor is zero by similar arguments. If Gauss' law in Eq. A.1 is applied to the cylindrical surface in Figure A.1 with infinitesimal height and small radius  $R$ , Eq. A.3 results.

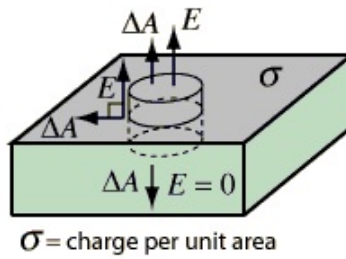


Figure A.1: Gaussian surface on conductor.

$$\oint \mathbf{E} \cdot d\mathbf{A} = \frac{Q}{\epsilon_0} \quad (\text{A.1})$$

$$E_n \pi R^2 = \frac{\sigma \pi R^2}{\epsilon_0} \quad (\text{A.2})$$

$$\mathbf{E}_n = \frac{\sigma}{\epsilon_0} \hat{\mathbf{n}} \quad (\text{A.3})$$

Consider the conducting body in Figure A.2 with varying charge distribution  $\sigma(\mathbf{r})$ . The force on a differential section of surface area  $dA$  is the product of the adjacent electric field  $E_n$  and the differential charge  $dq$ . Using the relation in Eq. A.3, summed over the entire body's surface, the total electrostatic force on the body in Eq. A.7 results. Similarly, one can determine the total moment on the body, given in Eq. A.8.

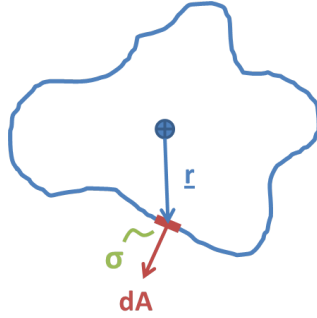


Figure A.2: Charged Conductor.

$$d\mathbf{F} = \mathbf{E}_n dq \quad (\text{A.4})$$

$$= E_n \sigma dA \quad (\text{A.5})$$

$$= \frac{\sigma^2}{\epsilon_0} dA = \epsilon_0 E_n^2 dA \quad (\text{A.6})$$

$$\mathbf{F} = \oint \frac{\sigma(\mathbf{r})^2}{\epsilon_0} dA = \oint \epsilon_0 E_n(\mathbf{r})^2 dA \quad (\text{A.7})$$

$$\mathbf{L} = \oint \frac{\sigma(\mathbf{r})^2}{\epsilon_0} \mathbf{r} \times d\mathbf{A} = \oint \epsilon_0 E_n(\mathbf{r})^2 \mathbf{r} \times d\mathbf{A} \quad (\text{A.8})$$

If the local charge distribution  $\sigma_i$  or the local electric field  $E_{n,i}$  can be measured at discrete points along the surface of a body, it is possible to approximate the force and moment due to the associated fraction of surface area.

$$\mathbf{F} = \sum \frac{\sigma_i(\mathbf{r})^2}{\epsilon_0} \mathbf{A} = \sum \epsilon_0 E_{n,i}(\mathbf{r})^2 \mathbf{A} \quad (\text{A.9})$$

$$\mathbf{L} = \sum \frac{\sigma_i(\mathbf{r})^2}{\epsilon_0} \mathbf{r} \times \mathbf{A} = \sum \epsilon_0 E_{n,i}(\mathbf{r})^2 \mathbf{r} \times \mathbf{A} \quad (\text{A.10})$$

The benefit of this method is that no knowledge of the electrodynamic surroundings of the sensing body is required to determine the Coulomb mechanics. Debye shielding due to plasma effects is inherently included in the calculated forces and moments, as well as any bias forces solely due to space weather. The forces imparted on a foreign object are equal and opposite to those determined from the charge distribution on the sensing spacecraft, because of Newton's third law.



## Appendix B

### MSM Code

```
function [bodyout, posout] = multisphere2(body, pos)
% MULTISPHERE function to compute the electrostatic interactions between n
% conductors & insulators each approximated by a finite number of spheres.
%%%%%%%%%%%%%%%%%%%%%%%%%%%%%%%%%%%%%%%%%%%%%%%%%%%%%%%%%%%%%%%%%%%%%%%%
%
% INPUTS
% For each body i, input the structure "body" with the following fields:
%
% body(i).sphs = [x_1 ... x_n
%                 y_1 ... y_n
%                 z_1 ... y_n
%                 R_1 ... R_n]
% * coordinates from body origin & radius of the n spheres in the MSM of body i
%
% body(i).Vq = [V_j ... NaN ... NaN    NaN
%              NaN ... q_j ... NaN    NaN
%              NaN ... NaN ... q_tot1 q_tot1]
% * number of columns needs to be same as sphs field
% * each column above represents a different option for the spheres
% * 1.   conductor: voltage is specified in 1st row
% * 2.   insulator: charge is specified in 2nd row
% * 3/4. set of spheres that share a total fixed charge (and part of the same conductor)
%
% body(i).r = [r_x; r_y; r_z]
% * position in space of body origin
%
% body(i).C = DCM of body rotation in space (optional)
%
% pos = [pos1_x ... posn_x
%        pos1_y ... posn_y
%        pos1_z ... posn_z]
% * optional positions in space at which the function will return Voltage & E-field
```

```

% information
%
%
% OUTPUTS
% bodyout(i).F = [Fx; Fy; Fz] *force on body i
%
% bodyout(i).L = [Lx; Ly; Lz] *torque on body i
%
% bodyout(i).Vq = [V_1 ... V_n
%                  q_1 ... q_n]
% * voltage and charge on each sphere in body i
%
% bodyout(i).sphs_abs = [r1_x ... rn_x
%                        r1_y ... rn_y
%                        r1_z ... rn_z]
% * absolute positions in space of each sphere in body i
%
% posout.V = [V1 ... Vn]
% * Voltage in space at the points defined by pos
%
% posout.E = [E1_x ... En_x
%             E1_y ... En_y
%             E1_z ... En_z]
% * Electric field in space at the points defined by pos

b=length(body);
bodyout(b).Vq=[];
% Coulomb's constant [Nm^2/C^2]
kc=8.987551e9;

%initiate C & r field if doesn't exist
if ~isfield(body,'C')
    body(1).C=[];
end
if ~isfield(body,'r')
    body(1).r=[];
end

Vq=[];
%loop through bodies to initialize
for h=1:b
    %populate C if not specified
    if isempty(body(h).C)
        body(h).C=eye(3);
    end
    if isempty(body(h).r)
        body(h).r=zeros(3,1);
    end
end

```

```

end
%check if columns of sphs = columns of Vq
if size(body(h).sphs,2)~=size(body(h).Vq,2)
    error('ERROR: number of spheres and voltage/charge information do not...
    match')
end
%check if either q or V is given for all spheres
if sum(sum(isnan(body(h).Vq))==size(body(h).Vq,1))
    error('ERROR: invalid voltage or charge specified')
end
%rotate & translate spheres
body(h).sphs(1:3,:)=body(h).C'*body(h).sphs(1:3,:); %rotation - adjust...
% input for torque calc later
bodyout(h).sphs_abs=[body(h).sphs(1:3,:)+repmat(body(h).r,1,size...
(body(h).sphs,2));body(h).sphs(4,:)]; %translation, write to output
%build Vq (expand rows to furthest)
if size(body(h).Vq,1)>size(Vq,1)
    Vq=[padarray(Vq,size(body(h).Vq,1)-size(Vq,1),NaN,'post'),body(h).Vq];
elseif size(Vq,1)>size(body(h).Vq,1)
    Vq=[Vq,padarray(body(h).Vq,size(Vq,1)-size(body(h).Vq,1),NaN,'post')];
else
    Vq=[Vq,body(h).Vq];
end
end

sphs=[bodyout.sphs_abs]; %for position dependent capacitance matrices

%find conducting & insulated spheres
sphs_c=sphs(:,isnan(Vq(2,:)));
sphs_i=sphs(:,isfinite(Vq(2,:)));

%initialize
q_i=Vq(2,isnan(Vq(1,:)))';
V_c=Vq(1,isnan(Vq(2,:)))'/kc; %scale by kc to avoid poor conditioning
V_c(isnan(V_c))=0; %for constant charge conductors

%add conductors with total charge
if size(Vq,1)>2
    qtots=zeros(size(Vq,1)-2,1);
    for i=3:size(Vq,1)
        qtots(i-2)=Vq(i,find(isfinite(Vq(i,:)),1));
    end
    V_c=[V_c;qtots];
else
    qtots=[];
end
end

```

```

a=size(sphs,2);
m=size(sphs_c,2);
n=size(sphs_i,2);
q=length(qtots);

Cc_inv=zeros(m+q,m+q);
Ci_inv=zeros(m+q,n);
Ca_inv=zeros(a,a);

m_ind=1;
n_ind=1;

%loop through all spheres
for i=1:a
    %populate full cap matrix
    Ca_inv(i,i)=kc/sphs(4,i);
    for j=1:i-1
        Ca_inv(i,j)=kc/norm(sphs(1:3,j)-sphs(1:3,i));
        Ca_inv(j,i)=Ca_inv(i,j);
    end
    if isnan(Vq(2,i)) %conducting sphere, build cap matrix
        Cc_inv(m_ind,m_ind)=1/sphs(4,i); %kc omitted for conditioning
        for s=1:m_ind-1
            Cc_inv(m_ind,s)=1/(norm(sphs_c(1:3,m_ind)-sphs_c(1:3,s)));
            %kc omitted for conditioning
            Cc_inv(s,m_ind)=Cc_inv(m_ind,s);
        end
        m_ind=m_ind+1;
    elseif isnan(Vq(1,i)) %insulated sphere, build cap matrix
        for t=1:m
            Ci_inv(t,n_ind)=1/(norm(sphs_i(1:3,n_ind)-sphs_c(1:3,t)));
            %kc omitted for conditioning
        end
        n_ind=n_ind+1;
    end
end

%expand matrices for qtot spheres
for r=1:length(qtots)
    Cc_inv(m+r,isfinite(Vq(r+2,:)))=1;
    Cc_inv(isfinite(Vq(r+2,:)),m+r)=-1;
end

%calculate qs
if n==0 %no insulated spheres
    q_c=Cc_inv\V_c;
elseif m==0 %no conducting spheres

```

```

        q_c=[];
    else %combined
        q_c=Cc_inv\ (V_c-Ci_inv*q_i);
    end

    q_a=Vq(2,:)' ;
    q_a(isnan(q_a))=q_c(1:m);
    V_a=Ca_inv*q_a;
    Vq_out=[V_a,q_a]';

    %populate pos E & V

    if exist('pos','var')
        posout.V=zeros(1,size(pos,2));
        posout.E=zeros(size(pos));
        for g=1:size(pos,2)
            for f=1:a
                rho=pos(:,g)-sphs(1:3,f);
                posout.V(g)=posout.V(g)+kc*q_a(f)/norm(rho);
                posout.E(:,g)=posout.E(:,g)+kc*q_a(f)*rho/norm(rho)^3;
            end
        end
    end

    %populate forces & torques
    a_ind=1;
    for h=1:b
        p=size(body(h).sphs,2);
        bodyout(h).Vq=Vq_out(:,a_ind:a_ind+p-1);
        F=zeros(3,1);
        L=zeros(3,1);
        lp=1:a;
        lp(a_ind:a_ind+p-1)=[]; %index all but spheres in this body
        %calculate forces & torques
        for e=a_ind:a_ind+p-1
            for f=lp
                rij=sphs(1:3,e)-sphs(1:3,f);
                F=F+kc*q_a(e)*q_a(f)*rij/norm(rij)^3;
                L=L+tilde(body(h).sphs(1:3,e-a_ind+1))*kc*q_a(e)*q_a(f)*rij/norm(rij)^3;
            end
        end
        bodyout(h).F=F;
        bodyout(h).L=L;
        a_ind=a_ind+p;
    end

end
end

```

## Appendix C

### VMSM Parameter Variation

While the visual approach to quantifying the Multi-Sphere Method in Section 2.5.2 is useful for analyzing the quality of a single parameter fit, when multiple scenarios are compared to each other, it is desirable to have a single value for the quality of the fit for each scenario. The following scalar residual sums  $RES_F$  and  $RES_L$  for the model forces and torques are therefore defined. Here  $n$  is the number of external sphere locations  $\mathbf{d}_i$  where data points are considered, and  $F$  and  $L$  refer to the forces and torques from the MSM and the Maxwell truth data.

$$RES_F = \frac{\sum_{i=1}^n |F_{\text{MSM}}(\mathbf{d}_i) - F_{\text{truth}}(\mathbf{d}_i)|}{\sum_{i=1}^n F_{\text{truth}}(\mathbf{d}_i)} \quad (\text{C.1})$$

$$RES_L = \frac{\sum_{i=1}^n |L_{\text{MSM}}(\mathbf{d}_i) - L_{\text{truth}}(\mathbf{d}_i)|}{\sum_{i=1}^n L_{\text{truth}}(\mathbf{d}_i)} \quad (\text{C.2})$$

Dividing by the denominator ensures that this scalar residual sum is independent of the resolution of the data set. Table C.1 compares the residuals of the three-sphere MSM fit shown above and a single sphere model (equivalent to the Effective Sphere Method in<sup>35</sup>). The single sphere size is determined using the same non-linear fit, resulting in  $R = 0.9974$  m. It is clear that the single sphere results in much higher residuals than the three-sphere model, and  $RES_L$  for a single sphere is unity because it lacks the ability to predict any non-zero torques.

Table C.1: Scalar residual comparison between three-sphere MSM and single sphere model

	3 sphere MSM	Single sphere model
$RES_F$	0.0155	0.0972
$RES_L$	0.0485	1.0000

An important step to validating the Multi-Sphere Method is to verify whether a model with specific parameters scales with some of the arbitrary constants that were chosen when using Maxwell to develop a truth model data set. While the geometry of the modeled shape is specified in the problem statement, the size of the external sphere  $R_B$  and the model and external sphere voltage  $\phi_A$  and  $\phi_B$ , were chosen arbitrarily, though they represent typical spacecraft charge control parameters. When the MSM is utilized in simulations, these conditions are liable to change. Moreover, the external sphere could take on a generic 3D shape of its own, which can in turn be modeled with the MSM. To verify that the specific model holds when these parameters are changed, the outputs of the MSM with the optimized sphere parameters are compared to numerical simulations while individually varying the parameters  $R_B$ ,  $\phi_A$  and  $\phi_B$  and replacing the external sphere with a duplicate of the 3D body at two orientations. Remember that the nominal values are an external sphere with  $R_B = 0.5$  m,  $\phi_A = \phi_B = 30$  kV, and the same three-sphere model outlined in Table 2.1. The results are concisely summarized using scalar residual values in Table C.2.

Table C.2: Scalar residual comparison of scaled parameter variation from numerical simulation

$R_B$ variation	0.25 m	1m	
$RES_F$	0.0150	0.0578	
$RES_L$	0.0639	0.0749	
$\phi_A$ variation	-30 kV	10 kV	50 kV
$RES_F$	0.0281	0.0225	0.0242
$RES_L$	0.0370	0.1021	0.0745
$\phi_B$ variation	-30 kV	10 kV	50 kV
$RES_F$	0.0275	0.0733	0.0241
$RES_L$	0.0424	0.2454	0.0481
External cylinder	Parallel	Perpendicular	
$RES_F$	0.0355	0.0305	
$RES_L$	0.0350	0.0744	

The residual values for all the scaled scenarios are an improvement over the single sphere

residuals in Table C.1. The only scenario that yields less than desirable results are the combination of  $V = +30$  kV and  $V = +10$  kV. The induced charge effects are largest for this combination of charges, which are not captured by a three-sphere MSM. Future models with multiple spheres may capture these effects better. For now, it is still clear that the three-sphere model provides an improvement over other models because of its ability to resolve torques and forces more accurately than a single sphere approximation.



## Appendix D

### SMSM Packing Parameter

In order to analyze the optimal sphere size across various geometries, comparing the total surface area  $4\pi R^2 n$  of every sphere in the MSM to the total surface area  $S$  of the modeled geometry provides geometric insight. This relation is represented by the packing parameter  $\gamma$ :

$$\gamma = \frac{4\pi R^2 n}{S} \quad (\text{D.1})$$

For the spherical spacecraft being modeled with the SMSM, the optimal packing parameter is plotted against the number of spheres in the model in Figure D.1. Interestingly, even though the number of spheres in the model and therefore the spacing between them changes, the parameter  $\gamma$  appears to converge to a constant value.

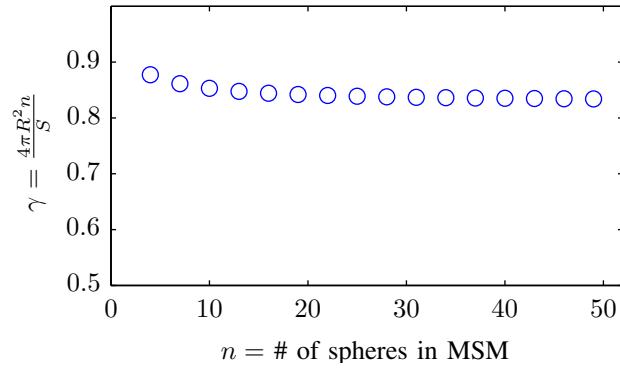


Figure D.1: Optimal packing parameter for Surface MSM on sphere

The same plot is given for the cylinder geometry in Figure D.2. Clearly, the optimal  $\gamma$  values do not match those for the sphere in Figure D.1. For this reason,  $R$  must be fit for a specific sphere

distribution to match the capacitance of a given model shape.

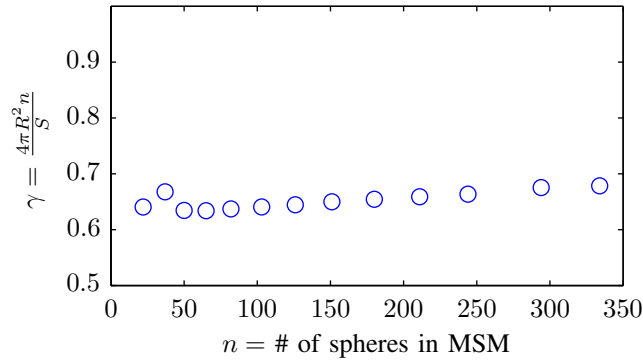
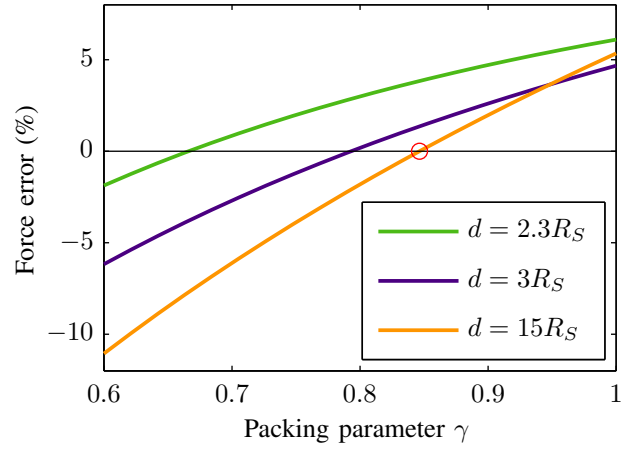


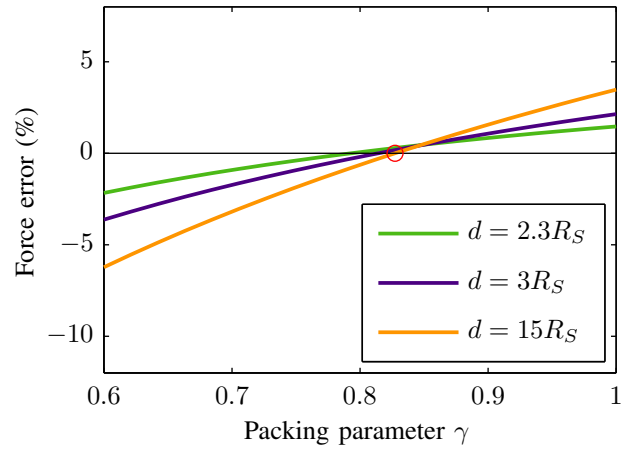
Figure D.2: Optimal packing parameter for Surface MSM on cylinder

In Section 2.5.1, the calculation error in the force between two spheres is analyzed for various models. These results beg the question, how does the uniform sphere radius  $R$ , and thus the packing parameter  $\gamma = \frac{4\pi R^2 n}{S}$ , affect the resulting force computations? In Figure 2.9, this parameter is optimized such that the capacitance of the MSM matches the capacitance of the sphere that it is intended to model. If a different  $R$  is chosen, might the model match the true forces better at close separation distances? Figure D.3 shows the error in force at three separation distances, for a range of  $\gamma$  values, comparing both the 10 and 30 sphere model. The repulsion configuration is chosen with  $V_1 = V_2 = +30$  kV.

At the larger separation distance ( $d = 15R_S$ ), the force error is minimized when  $\gamma = 0.8464$  for  $n = 10$  and when  $\gamma = 0.8273$  for  $n = 30$ , as shown by the red circle. This corresponds within a fraction of a percent to the optimal values in Figure D.1, suggesting that fitting the model-sphere radii to the body capacitance results in the optimal force prediction at larger separation distances. To match the induced charge effects and forces at closer distances, the optimal packing parameter  $\gamma$  (and therefore  $R$ ) is smaller. Choosing  $R$  on this basis, however, would result in significant errors at larger separation distances. In the end, spacecraft proximity missions would rarely operate at fewer than 10 craft radii separation unless docking is considered, so the best approach is to choose the sphere radii by matching to the spacecraft body's self-capacitance in deep space as outlined in



(a) MSM with 10 spheres



(b) MSM with 30 spheres

Figure D.3: Error in force for various packing parameters

Section 2.4. Notice that the sensitivity in force error to  $\gamma$  is appreciably decreased for the model with more spheres, which is a promising feature of the new method.